

Quantum Phase Transitions in Constrained Bose Systems

**Von der Fakultät Mathematik und Physik der Universität
Stuttgart zur Erlangung der Würde eines Doktors der
Naturwissenschaften (Dr. rer. nat.) genehmigte Abhandlung**

Vorgelegt von
Dipl. Phys. (ETH) Lars Bonnes
aus Dinslaken

Hauptberichter: Prof. Dr. Stefan Wessel, Ph.D.

Mitberichter: Prof. Dr. rer. nat. Günter Wunner

Tag der mündlichen Prüfung: 20.07.2011

Institut für Theoretische Physik III
Universität Stuttgart

2011

Contents

I. Zusammenfassung	7
II. Abstract	9
III. Table of Acronyms	11
IV. Curriculum Vitae	13
1. Tailoring Interactions in Cold Quantum Gases	15
1.1. Introduction	15
1.2. Bosons in Optical Lattices	17
1.3. Dissipation Induced Three-body Constraint	19
1.4. Supersolid Nucleation Transition on the Triangular Lattice	21
1.5. Engineering Three-Body Potentials with Polar Molecules	26
1.6. Experimental Probes in Cold Gases	32
2. Methods	37
2.1. Quantum Monte Carlo	37
2.1.1. Generalized Directed Loop Algorithm in the Stochastic Series Expansion	38

2.1.2.	Measuring Physical Observables	46
2.1.3.	Quantum Parallel Tempering	50
2.2.	Tensor Network Renormalization Group	52
2.2.1.	Coarse Graining the Tensor Network	53
2.2.2.	Convergence and Performance	57
2.3.	Accessing Phase Transitions	59
2.3.1.	First and Second Order Phase Transitions	59
2.3.2.	Berezinskii-Kosterlitz-Thouless Transition	62
3.	Pairsuperfluidity in Dynamically Constrained Bose Systems	65
3.1.	Effective Feshbach Model	67
3.2.	ASF-Insulator Transition	69
3.3.	Accessing the Superfluid Phases	71
3.3.1.	ASF-PSF Transition	71
3.3.2.	On an Efficient Monte Carlo Update for the Pair Phase	75
3.4.	The Thermal Half-Vortex Unbinding Transition	78
3.5.	Perspectives towards a Parallel Multi-Worm Algorithm	81
4.	The Supersolid Nucleation Transition	85
4.1.	Generic Case	86
4.2.	Critical Properties of the Particle-Hole Symmetric Point	92
4.3.	SS-C at Finite Temperatures	96
5.	Triangular Supersolid beyond Two-Body Interactions	99
5.1.	Nearest-Neighbor Interactions	101
5.2.	Extended Model	102
5.3.	Supersolid-Supersolid Transition	105

6. Frustrating Three-body Interactions on the Honeycomb Lattice	111
6.1. Three-Body Interactions	114
6.1.1. Quantum Monte Carlo	116
6.1.2. Incompressible Phases	118
6.1.3. VBS-VBS Quantum Phase Transitions	130
6.1.4. Classical Limit	135
6.2. Two-body Interactions	139
6.2.1. Cascaded Transition	140
6.2.2. Numerical Results	142
7. Outlook and Conclusion	145
7.1. Open Questions	145
7.2. Disordered Supersolid: Towards a Glassy Solid	146
7.3. The N-Flavor Hubbard Model with Alkali Earth Atoms	147
A. Locally Optimal Scattering Probabilities	151
B. Helicity Modulus for the Pairsuperfluid	153
C. Implementation of LoadLeveller	155

I. Zusammenfassung

Die vorliegende Doktorarbeit befasst sich mit aktuellen Fragen niedrigdimensionaler Quantensysteme, wie sie in heutigen Experimenten mit ultrakalten Quantengasen realisiert werden können. Ein Hauptaugenmerk, vom Standpunkt der quanten-statistischen Mechanik aus gesehen, liegt dabei auf der Charakterisierung von Quanten- und thermischen Phasen sowie ihrer Übergänge mit Hilfe von numerischen Methoden wie Quanten-Monte-Carlo oder der Tensornetzwerk-Renormierungsgruppe.

Der erste Teil befasst sich mit Gitterbosonen unter dem Einfluss starker Dreikörperverluste. Die Dynamik wird, ähnlich dem Quantenzenoeffekt, auf den Unterraum eingeschränkt, in dem Dreifachbesetzungen vermieden und somit dissipative Prozesse unterdrückt werden. Die Niederenergiephysik kann durch ein effektives Feshbach-Modell beschrieben werden, in dem die Paarphysik interessantes quantenkritisches Verhalten zeigt, das durch den Coleman-Weinberg-Mechanismus beschrieben wird. Eine ausführliche numerische Untersuchung wird in Kapitel 3 präsentiert, die, zum einen, die Eigenschaften der Paarsuperfluid-Phase untersucht. Desweiteren wird das Auftreten eines unkonventionellen Sprungs der Helizität gefunden, der sich auf das Proliferieren von Halbvortexanregungen zurückführen lässt. Die besondere Natur der Paarphase führt zum Auftreten einer endlastigen Verteilung im Monte-Carlo-Verfahren and erschwert effektive Simulationen in diesem Regime. Eine generische Erweiterung des Monte-Carlo-Updates, das diese Samplingprobleme behebt, wird vorgestellt.

Der anschließende Teil befasst sich mit polaren Molekülen in optischen Gittern. Durch die spezielle Form ihrer Wechselwirkung und starke Beeinflussbarkeit durch externe elektrische Felder stellen sie ideale Kandidaten für die Realisierung neuer Zustände von Materie dar. Von besonderem Interesse ist hier ein Regime, das von starken Dreikörperwechselwirkungen dominiert ist.

I. Zusammenfassung

Zuerst wird die Quanten-Nukleation des Dreiecksgittersupersolids besprochen und Kapitel 4 gibt eine detaillierte Symmetrieanalyse in Verbindung mit Monte-Carlo-Simulationen. Die Stabilität der besonderen Eigenschaften dieses Modells werden in Kapitel 5 im Hinblick auf realistische Potentiale mit Zwei- und Dreikörperwechselwirkungen untersucht.

Die Physik, die sich mit Hilfe von Dreikörperwechselwirkungen realisieren lässt, wird in Kapitel 6 an Hand von einem Bosegas auf dem Bienenwabengitter weiter untersucht. Frustration und das Auftreten von Valencebondsolids im Quantenregime charakterisieren das Phasendiagramm dieses Modells. Die Wechselwirkung zwischen Zwei- und Dreikörpertermen führt zu einer Kaskade von Zwischenphasen mit sehr großen Superstrukturen. In diesem Zusammenhang wird die Anwendung der Tensornetzwerk-Renormierungsgruppe auf Systeme mit Vielkörperwechselwirkungen demonstriert und es werden generische Limitationen in der Implementierung dieses Algorithmus aufgezeigt.

Kapitel 7 widmet sich noch offenen Fragen und stellt Ergebnisse aus aktuellen Projekten vor. Es geht dabei um den Einfluss von Unordnung auf einen Supersolid, der eine neue Glasphase zu stabilisieren scheint, die als Koexistenz eines Bose-Glas und eines Solids verstanden werden kann. Ein weiterer Fokus liegt auf der Berechnung der Entropie von eindimensionalen $SU(N)$ Hubbard-Modellen im Hinblick auf aktuelle Experimente mit Erdalkalimetallen.

Eine Liste mit Veröffentlichungen, die im Rahmen dieser Doktorarbeit entstanden sind, findet sich in Kapitel II.

II. Abstract

This doctoral thesis studies low dimensional quantum systems that can be realized in recent cold atom experiments. From the viewpoint of quantum statistical mechanics, the main emphasis is on the detailed study of the different quantum and thermal phases and their transitions using numerical methods, such as quantum Monte Carlo and the Tensor Network Renormalization Group.

The first part of this work deals with a lattice Boson model subject to strong three-body losses. In a quantum-Zeno like manner, a dynamical three-body constraint arises that restricts the evolution of the quantum system to the subspace with at most two particles per site i.e., three-body losses will be suppressed. Its low-energy description by a Feshbach model leads to the appearance of a pair condensate phase with intriguing quantum critical properties controlled by the Coleman-Weinberg mechanism. A comprehensive numerical study, presented in Chapter 3, identifies the pair phase and provides evidence for an unconventional Berezinskii-Kosterlitz-Thouless transition due to the unbinding of half-vortices. The study of the pair phase with worm-like algorithms turns out to be challenging and an extension of the directed loop algorithm is presented that overcomes the sampling limitations posed by the appearance of fat-tail distributions.

In the following chapters, attention is drawn to lattice systems of polar molecules in optical lattices. Their intriguing dipolar interaction and sensitivity towards external fields make them ideal candidates to realize new states of matter. Particularly, it has been shown that one can drive these systems into a regime where the interaction is dominated by competing two- and three-body potentials. First, the triangular lattice supersolid is considered in Chapter 4. An extensive numerical study combined with a detailed symmetry analysis answers the question of the nature of the supersolid quantum nucleation transition. Following this discussion, Chapter 5 investigates whether the characteristic features of this model

persist in the presence of interactions for a realistic system with polar molecules.

The three-body interaction regime in a honeycomb Bose-Hubbard model turns out to give rise to a set of highly complex phases in terms of valence bond solids and leads to frustration. Chapter 6 studies the phase diagram and shows how the competition between two- and three-body interactions exhibiting a cascade of phases in the regime of intermediate couplings. In addition, it is demonstrated how the Tensor Network Renormalization Group can be applied to systems with multibody interactions and generic algorithmic limitations are described.

Finally, preliminary results concerning the effect of quantum disorder on the triangular supersolid and recent calculations for the entropy of one-dimensional trapped $SU(N)$ Hubbard models are discussed in Chapter 7.

The main results of Chapters 3, 5 and 6 of this thesis have been published in peer reviewed journals.

- L. Bonnes and S. Wessel, *Pair Superfluidity of Three-Body Constrained Bosons in Two Dimensions*, Phys. Rev. Lett. 106, 185301 (2011)
- L. Bonnes and S. Wessel, *Supersolid Polar Molecules beyond Pairwise Interactions*, Phys. Rev. B 83, 134511 (2011)
- L. Bonnes, H.P. Büchler and S. Wessel, *Polar molecules with three-body interactions on the honeycomb lattice*, New J. Phys. 12, 053027 (2010)
- L. Bonnes and S. Wessel, *Three-Body Strongly Correlated Polar Molecules in Optical Lattices*, John von Neumann Institute for Computing: Proceedings of the NIC Symposium 2010

The results of Chapter 4 can be found in the preprint

- L. Bonnes and S. Wessel, *Generic First-Order vs. Continuous Quantum Nucleation of Supersolidity*, arXiv:1105.1682 (submitted to Phys. Rev. Lett.).

III. Table of Acronyms

b_i, b_i^\dagger	Bosonic creation and annihilation operators action on site i
n_i	Boson counting operator action on site i , $n_i = b_i^\dagger b_i$
\mathbb{Z}_q	Cyclic group with q elements
$U(1)$	Unitary group of degree 1
$SU(N)$	Special unitary group of degree N
χ^2/DOF	Chisquare per degree of freedom
BEC	Bose-Einstein condensate
(O) DLRO	(Off) Diagonal long range order
DMRG	Density Matrix Renormalization Group
ED	Exact diagonalization
HB	Heat-Bath
(Q)MC	(Quantum) Monte Carlo
locopt	Locally optimal scattering probabilities
minbounce	Bounce minimization scattering probabilities
NF	Normal fluid
RG	Renormalization group
SF	Superfluid
SS	Supersolid
SSE	Stochastic series expansion
STIRAP	Stimulated Raman adiabatic passage
TDL	Thermodynamic limit
TG	Tonks-Girardeau
TNRG	Tensor Network Renormalization Group
TOF	Time-Of-Flight

IV. Curriculum Vitae

- Name: Lars Bonnes
- E-Mail: lars@itp3.uni-stuttgart.de
- Date of Birth: 19 April 1984 in Dinslaken, Germany
- Education: 2003: German Abitur at the Theodor-Heuss Gymnasium Dinslaken, Germany
- Studies: 2003 - 2005: RWTH Aachen University
Vordiplom in 10/2005
- 2005-2008: Federal Institute of Technology ETH Zürich
Diplom in 04/2008
Thesis: Emergent Gauge Theories in Frustrated Magnetic Systems
Supervisor: Prof. M. Troyer
Scholarship holder of the Studienstiftung des Deutschen Volkes
- Since 09/2008: Doctoral Student at the University of Stuttgart
Institute for Theoretical Physics III
Supervisor: Prof. S. Wessel
Thesis: Quantum Phase Transitions in Constrained Bose Systems
Scholarship holder of the Studienstiftung des Deutschen Volkes
- Publications:
- L. Bonnes and S. Wessel, *Pair Superfluidity of Three-Body Constrained Bosons in Two Dimensions*, Phys. Rev. Lett. 106, 185301 (2011)

- L. Bonnes and S. Wessel, *Supersolid Polar Molecules beyond Pairwise Interactions*, Phys. Rev. B 83, 134511 (2011)
- L. Bonnes, H.P. Büchler and S. Wessel, *Polar molecules with three-body interactions on the honeycomb lattice*, New J. Phys. 12, 053027 (2010)
- L. Bonnes and S. Wessel, *Three-Body Strongly Correlated Polar Molecules in Optical Lattices*, John von Neumann Institute for Computing: Proceedings of the NIC Symposium 2010

Preprints:

- L. Bonnes and S. Wessel, *Generic First-Order vs. Continuous Quantum Nucleation of Supersolidity*, arXiv:1105.1682 (submitted to Phys. Rev. Lett.).

1. Tailoring Interactions in Cold Quantum Gases

1.1. Introduction

Almost twenty years after the demonstration of laser cooling [1], the first Bose-Einstein condensate (BEC) was reported in 1995 [2–4]. This remarkable achievement, which was awarded with the Nobel Prize in physics in 2001 [5], triggered a new era of atomic and molecular optics. Important hallmarks are the demonstration of the wave nature of matter by the production of an “atom laser“ [6] or the observation of the superfluid-Mott insulator transition by Greiner *et al.* [7]. The high degree of control over the interactions and the pureness of the systems allow high precision measurements, used e.g. in for atomic clocks [8–10] and gravimetric experiments [11].

In the past decade, tailoring quantum matter has gained a lot of interest in the atomic and molecular optics community. In particular, interactions of an ultra-cold quantum gas can be tuned by applying external electric and magnetic fields such that it can be used to resemble a particular behavior. This approach is complementary to condensed matter physics where the properties of a system are fixed by its lattice geometry, doping or chemical composition. One goal is to obtain further insight into well established models emanating from condensed matter physics, such as the Hubbard model [12, 13] or frustrated magnets [14], by engineering the interactions in ultra-cold gases accordingly [15, 16]. In addition, questions of statistical physics, such as concerning quantum criticality, can be accessed directly [17–19]. There also are proposals to go beyond current solid-state systems and explore exotic quantum matter, simulate (lattice) gauge theories [20, 21] or even realize a quantum computer [22–25].

Compared to solid state physics, ultra-cold quantum gases are very peculiar systems. Solid state systems have a lattice constants of a few Ångströms and the temperature scales for the onset of superconductivity, for instance, range from a few Kelvin in mercury up to about 100 K for the cuprates [26] and can be reached by liquid gas cooling. The usual solid state description is based on electrons interacting with the electric potential of the ions forming the crystal lattice. Lattice systems in cold gases experiments, on the other hand, are usually implemented through optical lattices [16, 27]. Superimposing laser beams generate a spatially varying potential landscape for the quantum gas in one, two or three dimensions [16, 28] with lattice constants of a few hundred nanometers. Typical energy scales are about meV and below. Thus, the temperature regime at which quantum mechanics dominates the characteristics of the ultracold gas are of the order of 10^{-8} K . Accessing this temperature regime proves to be challenging and relies on cooling techniques such as evaporative [29, 30] or laser cooling [1]. Furthermore, the constituents used in ultra-cold quantum gases have a rich inner structure that make them sensible to external fields. The internal degrees can either be of electronic origin, such as the hyper-fine levels of alkaline-earth atoms [16] or rotational degrees of freedom in polar molecules [31].

In the remainder of this chapter, attention is drawn to specific aspects of the field of ultra-cold quantum gases that are important for the realization and understanding of the statistical physics problems addressed in this thesis. First, the creation of effective interactions due to strong dissipation will be discussed in Section 1.3. Hence, open quantum systems offer the opportunity to tune interactions into a new regime and give rise to intriguing quantum phases like the dynamically paired bosonic phase, detailed in Chapter 3. On the other hand, polar molecules are highlighted in Section 1.5 as ideal candidates for the realization of low-dimensional lattice system featuring supersolids (Chapter 4 and 5) or exotic frustration-induced states (see Chapter 6). Finally, recent experimental measurement and detection techniques are introduced in Section 1.6 and the connection between theoretical calculations and experimentally accessible observables is made.

It should be noted that the Boltzmann and Planck constant k_B and h will be set to unity throughout this work.

1.2. Bosons in Optical Lattices

Optical lattices form a spatially varying potential landscape for neutral atoms due to light-matter interaction. The external electric field, $\mathbf{E}(\mathbf{r})$, induces a dipole moment that has the form $\sim \chi_a(\omega)\mathbf{E}(\mathbf{r})$ in the linear response regime, where $\chi_a(\omega)$ denotes the polarizability of the atom [16, 27]. Thus, the interaction potential is given by

$$V^{\text{dipole}}(\mathbf{r}) = -\frac{1}{2}\chi_a(\omega)\mathbf{E}(\mathbf{r})^2. \quad (1.1)$$

In the vicinity of an internal resonance of the bare ground state of the atom, $|0\rangle$, to an excited state, $|1\rangle$, the dipole potential can be expressed as

$$V^{\text{dipole}}(\mathbf{r}) \approx \frac{3\pi c^2 \Gamma}{2\omega_0^3 \Delta} \mathbf{E}(\mathbf{r})^2, \quad (1.2)$$

where ω_0 is the frequency of the transition $|0\rangle \rightarrow |1\rangle$, Γ is the lifetime of $|1\rangle$ and $\Delta = \omega - \omega_0$ is the detuning of the laser from the atomic resonance [16, 27]. The form of the potential in Equation (1.2) has intriguing physical consequences. Namely, the atoms feel a force $\mathbf{F} \propto \Delta^{-1}\nabla\mathbf{E}^2$ and the particles are attracted to the maxima or minima of the intensity distribution, where the sign of the force can be controlled by either red or blue detuning of the electric (laser) field. The concept of optical lattices is to create an intensity pattern resembling a periodic structure of intensity extrema. In one dimension, for instance, this can be achieved by superimposing two counterpropagating laser beams forming a standing wave, $V^{\text{dipole}} = V_0 \sin^2(kz)V(x, y)$. The periodicity is controlled by the wave length $\lambda = 2\pi/k$ and V_0 is proportional to the intensity of the laser beam. $V(x, y)$ is the radial shape of the laser beam that will not be discussed further but can be thought of as a Gaussian beam profile $\sim \exp(-r^2/w^2(z))$ [16]. Higher dimensional lattices with various geometries such as simple square or cubic lattices or even triangular and kagome structures [32] can be formed with an appropriate number of laser beams. Another method for the generation of optical lattices is holographic projection as has been shown in the context of the single site microscopy [33].

In the next step, the Bose-Hubbard model is derived as an effective description

1. Tailoring Interactions in Cold Quantum Gases

for cold gases in an optical lattice. The starting point is the Hamilton operator for the bosonic fields ψ and ψ^\dagger ,

$$H = \int d^d r \psi^\dagger(\mathbf{r}) \left[-\frac{\nabla^2}{2m} + V^{\text{ext}}(\mathbf{r}) \right] \psi(\mathbf{r}) + \int \int d^d r d^d r' \psi^\dagger(\mathbf{r}) \psi^\dagger(\mathbf{r}') V(\mathbf{r}', \mathbf{r}) \psi(\mathbf{r}') \psi(\mathbf{r}), \quad (1.3)$$

in the presence of an external field $V^{\text{ext}}(\mathbf{r})$ and interparticle interaction $V(\mathbf{r}', \mathbf{r})$ in d dimensions. The external potential is an optical lattice periodic in all $d \leq 3$ dimensions and the non-interacting Hamiltonian can be solved using Bloch's theorem [34]. A trapping potential will be neglected throughout this work. In the case of a separable external potential, the Wannier functions $w_n(\mathbf{r})$ for each band n can be chosen such that they are real and decay like an exponential $\sim \exp(-x/c_n)$ for large distances thus describing a state localized at $x = 0$ [35]. The fields ψ and ψ^\dagger can be expanded in terms of bosonic operators $b_{i,n}$ ($b_{i,n}^\dagger$) annihilating (creating) a boson in the Wannier state $w_n(\mathbf{r} - \mathbf{r}_i)$, namely

$$\psi(\mathbf{r}) = \sum_{i,n} w_n(\mathbf{r} - \mathbf{r}_i) b_{i,n} \quad (1.4)$$

$$\psi^\dagger(\mathbf{r}) = \sum_{i,n} w_n(\mathbf{r} - \mathbf{r}_i) b_{i,n}^\dagger. \quad (1.5)$$

If the lattice is sufficiently deep¹ and the mean thermal and exchange energies are much smaller than the band-gap, one can drop contributions from higher bands. Furthermore, it is assumed, that the Wannier functions $w(\mathbf{r})$, where the band index will be omitted from now, decay within a single lattice site i.e., $\int d^d r w(\mathbf{r} - \mathbf{r}_i) w(\mathbf{r} - \mathbf{r}_j)$ is small for $i \neq j$ and $w(\mathbf{r} - \mathbf{r}_i)$ describes a well localized state at lattice site i . Substituting Equation (1.4) and Equation (1.5) into Equation (1.3) yields

$$H = - \sum_{i \neq j} t_{ij} b_i^\dagger b_j - \sum_i \mu_i n_i + \sum_i U_i n_i (n_i - 1) + \sum_{i \neq j} V_{ij} n_i n_j. \quad (1.6)$$

¹Sufficiently deep means that the recoil energy, that is the kinetic energy $k^2/2m$ of an atom absorbing an optical lattice photon with momentum k , is much smaller than the depth of the optical lattice V_0 .

The tunneling amplitudes t_{ij} , the on-site interactions μ_i and U_i and the extended density interactions V_{ij} are given by integrals over Wannier functions and depend on the external fields, such as the depth of the optical lattice or particle-particle interactions. The particle number operator is given as $n_i = b_i^\dagger b_i$. In the ultra-cold regime, the dominant interaction will be s-wave scattering. Hence, the van-der-Waals interaction between two neutral atoms can be approximated by a point-like pseudopotential and the density interaction reduces to $U_i = U$, $V_{ij} = 0$ and $t_{ij} = 0$ if i and j are not nearest-neighbors, $t_{ij} = t$ otherwise. μ_i constitutes an on-site energy and can be motivated as a chemical potential or an external confinement.

1.3. Dissipation Induced Three-body Constraint

Customarily, interactions in ultra-cold quantum gases are controlled by external fields tuning the elastic interactions. For instance, the s-wave scattering amplitude is controlled via a Feshbach resonance [36] and the hopping parameter depends on the depth of the external potential. However, trapped quantum gases do not constitute a closed quantum system but are subject to loss from inelastic collisions. These processes are, in general, unwanted since they lead to heating and dilution. It turns out, that strong losses can also drive the system into a strongly-correlated regime. Recently, Syassen *et al.* [37, 38] report that they produce a BEC of bosonic $^{87}\text{Rb}_2$ molecules in the hardcore regime induced by inelastic two-body recombinations. The avoidance of doubly occupied sites can be interpreted as leading to a suppression of inelastic scattering in a quantum Zeno like manner [39, 40] leading to an effective hardcore constraint [38]. The bosonic gas in the Tonks-Girardeau (TG) regime resembles the behavior of a one-dimensional Fermi gas [41–43]. This approach is in contrast to the work by Paredes *et al.* [44] firstly reaching the TG regime in a dilute ^{87}Rb BEC by explicitly tuning the ratio of kinetic energy $\gamma \approx U/t$ by an additional lattice potential increasing the effective mass of the rubidium atoms.

Extending the idea of dissipation induced interactions, Daley *et al.* [45] propose a setup where an effective three-body constraint arises giving rise to interesting phenomena beyond the well understood TG gas. In particular, the

motivation is to mimic the three-body contact interactions in quantum Hall systems [46] that can give rise to exotic ground-states with non-abelian excitations [47, 48]. The interest of this work is a different regime, though. An attractive Bose gas subject to strong three-body losses, controlled by driving the system through a three-body resonance [49], will be stabilized from collapse since triply occupied sites will be avoided, in analogy to the TG case mentioned before. Delay *et al.* [45] derive the dynamical suppression from a microscopic Bose-Hubbard model subject to three-body losses by solving the master equation and employing time-dependent DMRG (tDMRG) [50, 51] in combination with quantum trajectories [52]. The attractive interaction gives rise to the formation of atom pairs that will condense without the formation of an atomic condensate. Intriguing quantum critical behavior is expected from the formation of this new phase due to the interaction of the Goldstone mode of the atomic condensate with an Ising field emerging from the formation of bosonic pairs, discussed in the framework of Feshbach models [53, 54].

Chapter 3 presents a comprehensive numerical study of the attractive Bose-Hubbard model with three-body constraint on the square lattice and provides details beyond the results published recently in Physical Review Letters [55]. First, the existence of the pair superfluid (PSF) phase and its transition to the atomic superfluid (ASF) is studied. Using an extended update for the directed loop algorithm (see Chapter 2.1.1), the atomic and pair Green's function $G_n(ij) = \langle (b_i^\dagger)^n (b_j)^n \rangle$ ($n = 1, 2$) can be accessed directly and the ASF and PSF phase can be distinguished quantitatively. It turns out, that sampling the pair Green's function using a double worm update suffers from a fat-tailed distribution [56] such that the Monte Carlo error is not well defined anymore. Using a linear coupling scheme, that introduces hopping between all lattice sites, it is shown how to circumvent this (generic) sampling problem. The ASF-PSF transition is found to be dominated by an Ising critical point but the large correlation length prohibits a clear identification of the nature of the phase transition near unit filling. In addition to that, the insulator-superfluid transition, that is expected to be in the dilute Bose gas universality class [57], is found to be driven first-order for certain values of $\mu/|U|$, in overall agreement with a recent effective potential approach [12]. The effective pairing mechanism is also reflected in the

high-temperature physics and the universal jump of the helicity modulus has to be modified to take into account the unbinding of half-vortices in the paired phase [58]. After presenting the finite-temperature phase diagram, attention is drawn to the discrimination of the ASF and PSF phase at finite temperature since breaking of the $U(1)$ symmetry is prohibited by the Mermin-Wagner theorem [59]. Ng and Yang argue, that the ASF and PSF can be distinguished by an even-odd effect in the winding numbers [60] due to the formation of pairs. Whereas this is true for the model presented in Equation (3.1), this classification fails in the generic case. By including pair hopping terms driving the ASF-PSF transition explicitly, it is shown that the parity of the winding numbers does not suffice to quantitatively differentiate the two superfluids and one has to resort to the Green's function to detect quasi-long range order in the atomic and pair channel. Concludingly, the differences between the multi-worm update presented by Ng and Yang [60] and the pairworm presented in this work will be delineated.

1.4. Supersolid Nucleation Transition on the Triangular Lattice

The term “supersolid” describes a peculiar phase in which solid diagonal long-range order (DLRO) and off-diagonal long-range order (ODLRO) coexist and are stable towards phase separation. The question “Can a Solid Be ‘Superfluid’” was asked by Legget [61] and others [62–64] more than forty years ago. Legget considers a cylindric oscillator filled with solid ^4He . If DLRO and ODLRO coexist, the superfluid part will decouple from the oscillation and the moment of inertia is decreased by $\sim \rho_s/\rho$, where ρ_s/ρ is the superfluid fraction [61]. The appearance of the non-classical rotational inertia fraction (NCRIF) was firstly observed in 2004 by Kim and Chan [65, 66]. However, the interpretation of the NCRIF in solid helium turns out to be more subtle since the observability of NCRIF and other related effects highly depends on the pureness of the helium crystals [65–67]. Thus, bulk supersolidity does not seem to be an inherent property of solid helium but an effect of disorder like grain boundaries or interstitials [67–69].

In low-dimensional lattice systems, however, the situation is more clear and the existence of supersolid phases has been established for a variety of Bose-

Hubbard like models [70–79]. The stability of domain walls between the solid and the superfluid determine the stability of the supersolid towards phase separation. The latter occurs for most hardcore Bose-Hubbard models with purely nearest neighbor interactions, such as the formation of the $n = 1/2$ checkerboard solid on the square [71] or honeycomb lattice [80]. Additional interactions like the inclusion of higher bands [81], softening the hardcore constraint [71], considering layered systems [76] or adding nearest-neighbor [82] or long-range (dipolar) interactions [77, 83], however, are known to destabilize the formation of domain walls. In this situation, vacancies or interstitials can hop through the system along “superflow paths” thus condensing and leading to ODLRO².

Notably, the group around Tilman Esslinger reports the realization of a supersolid phase, in terms of the coexistence of DLRO and OLDRO, by coupling a BEC to the modes of an optical cavity [85]. Self organization leads to the formation of a checkerboard structure in the condensate and superimposes a solid like structure onto the BEC [85, 86]. Even though the term supersolid is correct, it should be distinguished from the lattice supersolid described earlier. In these systems, supersolidity comes from vacancies or interstitials (density fluctuations) that move coherently through a solid structure; the supersolid can be seen as a two-component system. The solid structure in the “checkerboard BEC” is a spatial variation of the density of the BEC and resembles a one component system where all particles are coherent.

The situation for hardcore bosons on the triangular lattice with nearest-neighbor interactions is peculiar since the interplay of geometrical frustration on the triangular bonds and delocalization stabilizes a supersolid phase. In face of the recent experimental realization of the superfluid-Mott transition in a triangular optical lattice using ⁸⁷Rb atoms [32] and proposals to study frustrated bosonic systems in this geometry [87], the triangular Bose-Hubbard model is a promising candidate for the first experimental realization of a lattice supersolid. The triangular lattice attracted a lot of interest in the past year [70, 72–75, 78, 88–93]. In particular, the Hamiltonian for hardcore bosons with nearest-neighbor tunneling

²This does not need to be the case but the superflow can also emerge from higher order hopping processes as exemplified by the checkerboard supersolid [84]. However, the energy scales for the superflow are not of the order of the hopping t but t^2/V reducing the stability of the supersolid towards thermal excitations.

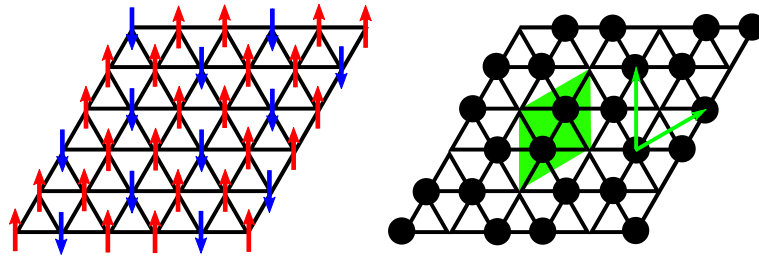


Figure 1.1.: Classical spin configuration (left) and corresponding density pattern showing the $n = 2/3$ solid. The green lozenge denotes the unit cell of the solid ordering and the green vectors the basis vectors.

amplitude t and repulsion, $V > 0$, reads

$$H = -t \sum_{\langle ij \rangle} \left(b_i^\dagger b_j + b_j^\dagger b_i \right) + V \sum_{\langle ij \rangle} n_i n_j - \mu \sum_i n_i. \quad (1.7)$$

Firstly, consider the classical ($t = 0$) Hamiltonian and reformulate it in terms of an antiferromagnetic Ising model substituting $n_i \rightarrow S_i^z + 1/2$ reading

$$H^\Delta = -J \sum_{\langle ij \rangle} S_i^z S_j^z + h \sum_i S_i^z \quad (1.8)$$

with $J = -V < 0$ and $h = V - 3\mu$.

The antiferromagnetic coupling leads to frustration [94] as the interaction term can not be minimized on all bonds of a plaquette simultaneously. This model has been studied extensively in the past decades [95–100]. At $h = 0$, the ground-state consists of all spin configurations where two spins on each plaquette point in the same direction and has an extensive degeneracy [101–107]. Alexander and Picus find, that the system exhibits a six-fold symmetry [108] and the thermal disordering transition to a paramagnetic phase is governed by the \mathbb{Z}_6 vector model. The \mathbb{Z}_q vector model, or also called vector Potts or clock model, is a XY model with discretized values of the phase, $\theta_i = 2\pi/qn_i$ with $n_i = 0, 1, \dots, (q-1)$, reading $H^q = -\sum_{\langle ij \rangle} \cos(2\pi/q[n_i - n_j])$. For $q \geq 5$ the disorder transition is not direct but an intermediate phase appears separated by a BKT transition [109–113]. This phase resembles the XY phase ($q \rightarrow \infty$) with quasi long-range order and undergoes a second BKT transition to a paramagnet [114–118]. This is in agree-

ment with Monte Carlo results for the \mathbb{Z}_q model [118], the Ising model [99] and the classical Heisenberg model [119] on the triangular lattice. If spin symmetry is broken explicitly by an external magnetic field, $h \neq 0$, the symmetry is reduced to the sublattice rotational symmetry \mathbb{Z}_3 and the high temperature transition is within the $q = 3$ Potts universality class [112]. The spins order in a pattern that is depicted for $h > 0$ in Figure 1.1 giving a $\sqrt{3} \times \sqrt{3}$ ordering at wave vector $\mathbf{Q} = (2\pi/3, 0)$.

For the quantum regime ($t > 0$), the phase diagram of Equation (1.7) is sketched in Figure 1.2. In bosonic language, the magnetic ordering pattern correspond to two solids with filling $n = 1/3$ and $2/3$, related by particle hole symmetry around $\mu/V = 3$ ($h = 0$) and the corresponding structure factor [72–75] reads

$$S(\mathbf{Q}) = 1/N \sum_{ij} e^{i\mathbf{Q}\mathbf{r}_{ij}} \langle n_i n_j \rangle. \quad (1.9)$$

Both $n = 1/3$ and $2/3$ solid can be identified by $S((2\pi/3, 0))/N = 1/9$ for the ideal solid. Quantum fluctuations will eventually destroy DLRO and the solid undergoes a first-order quantum melting transition into a uniform superfluid phase with off-diagonal long range order (ODLRO) i.e., the bosons will condense, $\langle b \rangle \neq 0$, and the system will show a superfluid response ρ_s . It turns out, that the solid phase is stable up to $t/V \approx 0.2$ [72]. For intermediate values of μ , however, two supersolid phases appear which feature both DLRO and ODLRO and the supersolid with $1/3 < n \leq 1/2$ ($1/2 \leq n < 2/3$) will be denoted SS-A (SS-B). The supersolid phase additionally breaks the $U(1)$ symmetry of the phase of the bosonic wavefunction and, thus, is in the 3D XY universality class. At $\mu/V = 3$, the system exhibits a discontinuous supersolid-supersolid transition [75] where the superfluid density ρ_s , the filling n and the structure factor S/N are continuous but the internal structure of the sublattice density fluctuations changes. To understand this, one considers a single triangular plaquette in the classical limit. The density pattern $(\epsilon_1, \epsilon_2, \epsilon_3)$, where $\epsilon_i = \langle n_i - \langle n_i \rangle \rangle$, around the plaquette is given by $(2/3, -1/3, -1/3)$ and $(-2/3, 1/3, 1/3)$ for the $n = 1/3$ and $2/3$ solid. SS-A and SS-B resemble this density pattern even though the fluctuations are not pinned one finds $(\pm\epsilon, \mp\epsilon', \mp\epsilon')$ [72, 75] with, in general, $\epsilon \neq \epsilon'$. In order to

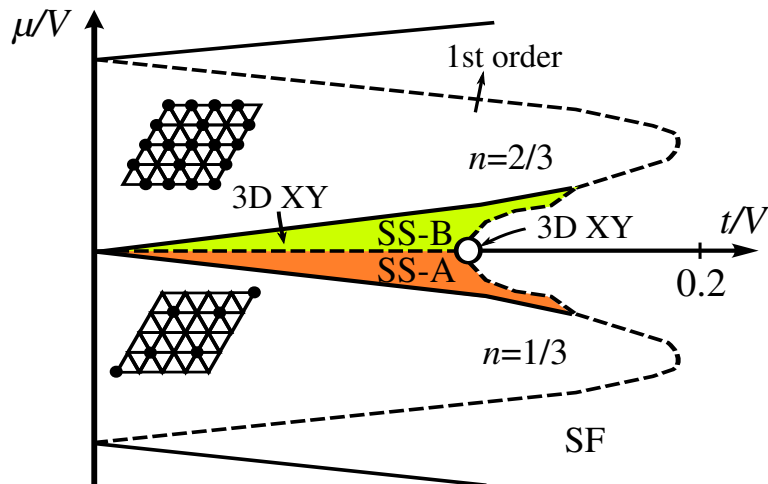


Figure 1.2.: Schematic phase diagram for hardcore bosons with nearest-neighbor hopping t and repulsion V on the triangular lattice (adapted from [72]). The dashed lines denote first-order transitions whereas the solid lines and the white circle denote 3D XY transitions.

distinguish SS-A and SS-B and formally see the aforementioned \mathbb{Z}_q symmetries of the classical model, one defines a phase variable θ on each plaquette where θ is defined the sublattice summation

$$\epsilon e^{i\theta} = \epsilon_1 + \epsilon_2 e^{-\frac{2\pi}{3}i} + \epsilon_3 e^{\frac{2\pi}{3}i}. \quad (1.10)$$

In the generic point away from particle-hole symmetry, a generalized magnetization, in analogy to \mathbb{Z}_3 vector models, takes values

$$\langle \cos(3\theta) \rangle \begin{cases} < 0, & \text{SS-A} \\ > 0, & \text{SS-B} \end{cases} \quad (1.11)$$

and the (super)solid breaks the three-fold sublattice rotational symmetry, as depicted in Figure 1.3. At $\mu/V = 3$, however, SS-A and SS-B coexist and $\langle \cos(3\theta) \rangle = 0$ but $\langle \cos(6\theta) \rangle > 0$. This illustrates the aforementioned symmetry enhancement to a six-fold, \mathbb{Z}_6 symmetry.

Employing large-scale quantum Monte Carlo simulations, the $T = 0$ nucleation transition is investigated. The results presented in Chapter 4, that are also accessible in a recent preprint [92], provide evidence for an extended regime of first-order transitions away from $\mu/V = 3$. An estimate for the “strength” of

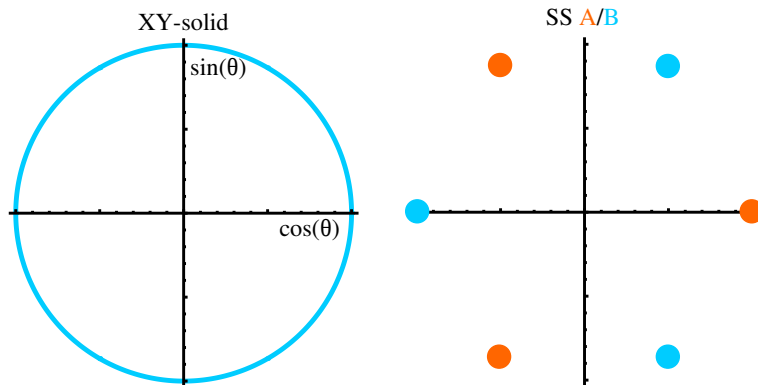


Figure 1.3.: Distribution of the complex magnetization defined in Equation (1.10) in the complex plane for the SS-A/B and the XY quasi-solid.

the first-order nature is given by explicitly extrapolating the order parameter peak positions at the point of phase coexistence. At the particle hole symmetric point, $\mu/V = 3$, the system is found to exhibit a continuous 3D XY transition, in accordance with the proposed scenario of symmetry enhancement. Within the numerical accuracy, no sign for a first-order transition at $\mu/V = 3$ is found.

1.5. Engineering Three-Body Potentials with Polar Molecules

A route towards new and exciting physics in the ultra-cold regime is provided by dipolar quantum gases [31, 120]. The interactions of dilute, neutral atomic gases is governed by the interatomic potential (van-der-Waals interactions) that can be modeled effectively by a contact interaction $U = g\delta(\mathbf{r})$. The coupling parameter g is fully determined by the particle mass and the s-wave scattering length. Dipolar gases, however, also feel a dipolar force generated by the potential

$$U_{\text{dipole}}(\mathbf{r}) = \frac{C_{\text{dipole}}}{4\pi} \frac{(\mathbf{e}_1 \mathbf{e}_2) \mathbf{r}^2 - 3(\mathbf{e}_1 \mathbf{r})(\mathbf{e}_2 \mathbf{r})}{r^5}. \quad (1.12)$$

Here, \mathbf{r} is the dipole separation and \mathbf{e}_i denotes the direction of the dipole moment [31]. Common folklore entitles dipolar interactions as anisotropic and the $1/r^3$ dipole interaction long-range. Whereas the former is true, the latter requires a more detailed discussion. Following the considerations by Astrakharchi

and Lozovik [121], the dipolar potential is truly long-range only for $d \geq 3$ and can be regarded as short range otherwise. Their argument is based on the intensity of the chemical potential and the possibility to perform a partial wave analysis of the scattering problem and define a s-wave scattering length in $d < 3$.

Comparing the strength of s-wave scattering versus dipole interaction, $\epsilon = C_{\text{dipole}}/3g$, the system will be dominated by U_{dipole} for $\epsilon \gtrsim 1$. The route towards the experimental preparation of dipolar quantum gases is pursued using different approaches. For instance, one can use the magnetic dipoles, that are about $1 \mu_{\text{B}}$ for ^{87}Rb and $6 \mu_{\text{B}}$ for ^{52}Cr . The first BEC of chromium was realized in Stuttgart by the group of Tilmann Pfau [122] and since then, BEC of atoms with magnetic dipole moments have proven to give interesting phenomena such as the stabilization of an attractive Bose gas [123, 124] and self-organization effects in stacked systems [125]. The magnetic dipole interaction, however, is comparably weak with $\epsilon \approx 1/6$ for chromium and even less for other alkali metals.

Polar molecules [31, 126], that are heteronuclear molecules, provide very large electric dipole moments of the order of a few Debye and an ϵ much larger than unity (e.g, $\epsilon \approx 20$ for KRb). Thus, they prove to be ideal candidates for the realization of dipolar quantum gases. In addition to the electronic degrees of freedom, molecules also possess rotational and vibrational modes. The cooling of the rovibrational degrees of freedom is crucial since the dipole moment decreases rapidly with increasing interparticle separation in higher excited states [127]. The production of ultra-cold alkali dimers has stimulated enormous experimental efforts [128–135]. In particular, the preparation of KRb [133, 134] and LiCs [130, 136, 137] in their rovibrational ground-state was reported recently. The creation of ground state alkali earth dimers usually starts from two clouds of ultra-cold atoms of species A and B. In the first step, a molecule AB^* is formed, where atom B is in a highly excited state. The ground-state transfer can be achieved by magneto-association via a Feshbach resonance followed by an adiabatic passage to the $X^1\Sigma^+$ rovibrational ground state, as used by Ni *et al.* [133] (cf. Figure 1.4) or by creating a highly excited alkali earth molecule via photo association that can decay into to ground-state via spontaneous or stimulated emission [137].

The sensitivity of polar molecules to electric fields and the anisotropic nature of their interactions make them ideal candidates for the engineering of quantum

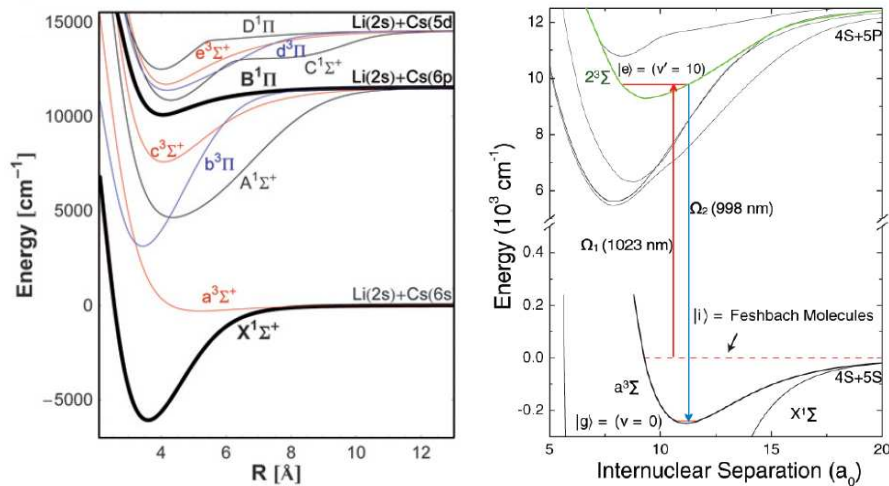


Figure 1.4.: **Left:** Interparticle potential for LiCs. The ground-state alkali metals are transferred via photoassociation of a bound state of Li(2s) and an excited Cesium atom. The highly excited ground-state decays to the rovibrational ground state of LiCs via spontaneous emission. Picture taken from Reference [137] **Right:** A weakly bound Feshbach molecule of potassium and rubidium is transferred into its rovibrational ground state by using a two-step STIRAP procedure via the bound state of an excited molecule, as presented in Reference [133].

states. The goal is to mimic condensed matter systems that elude themselves from an efficient numerical or analytical approach. Two prominent representatives are the two dimensional Hubbard model that suffers from a fermionic sign problem. Its has stimulated a lot of interest in the context of high temperature superconductors [12, 13] and graphene [138]. Furthermore, the realization of exotic quantum matter with non-trivial topological properties, as in quantum Hall states, or the realization of non-abelian quasi-particles that can be utilized for quantum computation, is proposed in cold molecular systems [21, 23, 139–142]. Of particular interest in this thesis is a recent proposal by Büchler *et al.* [142] to drive a system of polar molecules into a regime that is dominated by three-body interactions i.e., a potential term involving the position of three molecules. This type of interaction is unusual since all elementary excitation are inherently pairwise and multi-body terms usually come as small perturbations in an effective theory.

Polar molecules in an electric field, $\mathbf{E}(t)$, can effectively described by a rigid-

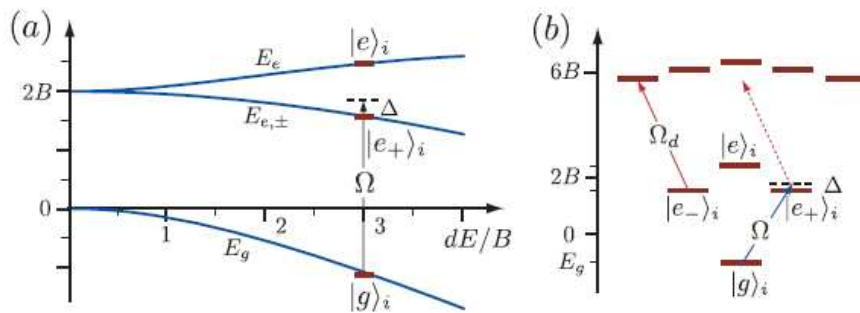


Figure 1.5.: **(a)** Ground-state, $|g\rangle$, and first excited, $|e\rangle$ and $|e_{\pm}\rangle$, energy levels of a rigid rotor with inertia B in an external field $\mathbf{E}(t) = E\mathbf{e}_z$. The external field lift the ground-state degeneracy of the $m = \pm 1$ and $m = 0$ states. **(b)** The ground and $|e_{\pm}\rangle$ levels are coupled by a microwave field with Rabi frequency Ω and detuning Δ . Coupling the $|e_{-}\rangle$ state to a $J = 2$ level by a second photon field with frequency Ω_d lifts the remaining degeneracy in the $m = \pm 1$ sector. Original picture found in Reference [142].

rotor [142]

$$H_{\text{rot}} = B\mathbf{J}^2 - \mathbf{d}\mathbf{E}(t). \quad (1.13)$$

Here, \mathbf{J} is the angular momentum operator, B is the moment of inertia and $\mathbf{d} = q\mathbf{r}$ is the dipole operator. The ground-state $|g\rangle$ for zero external field has s-wave symmetry, hence, its dipole moment vanishes. In order to derive an effective spin model, the degeneracy of the first excited level has to be lifted. Applying a static electric field along the z-axis, $\mathbf{E}(t) = E\mathbf{e}_z$, partially lifts the degeneracy of the $J = 1$ states, denoted by $|e_{\pm}\rangle$ for $m = \pm 1$ and $|e\rangle$ for $m = 0$. The residual degeneracy can be lifted by driving the transition from the $|e_{-}\rangle$ state to a $J = 2$ niveau with frequency Ω_d (cf. Figure 1.5). Thus, the $J = 0$ and $J = 1$, $m = 1$ rotational levels are coupled via a microwave field with frequency Ω and detuning Δ inducing Rabi oscillations between $|g\rangle$ and $|e_{+}\rangle$. The new dressed states are superpositions of $|g\rangle$ and $|e_{+}\rangle$ and the interaction Hamiltonian can be rewritten in terms of pseudo-spin 1/2 operators, \mathbf{S} , acting on the S_z eigenstates $|+\rangle = \alpha|g\rangle + \beta|e_{+}\rangle$ and $|-\rangle = \alpha|e_{+}\rangle - \beta|g\rangle$. Turning towards a many particle physics descriptions, consider an ensemble of polar molecules

at positions \mathbf{r}_i interacting via the dipole-dipole interaction. For strong dipole moments of the dressed states, $D = |\langle g|\mathbf{d}|e_+\rangle|^2$, the s-wave scattering potential will be neglected. Namely, the dipole interaction Hamiltonian within the rotating wave approximation takes the form of an anisotropic Heisenberg model in an external field [142],

$$H_d = -1/2 \sum_{i \neq j} D\nu(\mathbf{r}_{ij}) \left[S_i^x S_j^x + S_i^y S_j^y - \eta_-^2 S_i^z S_j^z - \frac{\eta_- \eta_+}{2} S_i^z - \frac{\eta_+^2}{4} \right]. \quad (1.14)$$

The function $\nu(\mathbf{r}_{ij}) = (1 - 3 \cos \theta)/r_{ij}^3$ is the anisotropic part of the dipole-dipole interaction for parallel aligned dipoles i.e., $\mathbf{e}_i = \mathbf{e}_z$ in Equation (1.12). The angle θ is measured between the vector connecting the dipole, \mathbf{r}_{ij} , and the direction of the dipoles, \mathbf{e}_i . In particular, this approximation is accurate for large separations $r \gg (D/B)^{1/3}$. In this regime, an effective description can be obtained in perturbation theory around the initially prepared state of parallel aligned dipoles $|K\rangle = \bigotimes_i |+\rangle_i$. From the energy shift obtained in second order in the small parameter $(R_0/a)^3$, where a is the typical interparticle separation and $R_0 = (D/\sqrt{\Delta^2 + \Omega^2})^{1/3}$ is a length scale constructed out of the dipole moment and the eigenenergies of the S_z eigenstates, an effective potential is inferred [142]. It consists of two parts, namely a two-body potential

$$V(\mathbf{r}) = \lambda_1 D\nu(\mathbf{r}) + \lambda_2 D R_0^3 \nu^2(\mathbf{r}) \quad (1.15)$$

and a three-body interactions

$$W(\mathbf{r}_1, \mathbf{r}_2, \mathbf{r}_3) = \gamma_2 R_0^3 D [\nu(\mathbf{r}_1 - \mathbf{r}_2)\nu(\mathbf{r}_1 - \mathbf{r}_3) + \nu(\mathbf{r}_1 - \mathbf{r}_2)\nu(\mathbf{r}_2 - \mathbf{r}_3) + \nu(\mathbf{r}_1 - \mathbf{r}_3)\nu(\mathbf{r}_2 - \mathbf{r}_3)]. \quad (1.16)$$

The couplings λ_1 , λ_2 and γ_2 are functions of the external field E and the relative detuning Δ/Ω . The striking observation of Büchler *et al.* is that there exists a parameter regime where $\lambda_1 = 0$ and $\lambda_2 \gtrsim 0.7\gamma_2$ [142]. This has the consequence that the two- and three-body interactions are equally relevant for the behavior of the quantum system and the asymptotic behavior of the potential is van-der-Waals like, $1/r^6$.

In the presence of a two-dimensional optical lattice, a Bose-Hubbard description can be derived. Owing to the perturbative nature of the effective potential approach, the validity is only guaranteed, if the lattice constant is sufficiently large and, in particular, tunneling to a already occupied site is strongly suppressed [142]. Thus, the particles can be modeled as hardcore and the following model, neglecting an inhomogeneous confining potential, is obtained

$$H = -t \sum_{\langle ij \rangle} \left(b_i^\dagger b_j + \text{h.c.} \right) + \sum_{ij} \frac{V_{ij}}{2} n_i n_j + \sum_{ijk} \frac{W_{ijk}}{6} n_i n_j n_k - \mu \sum_i n_i. \quad (1.17)$$

Here, b_i (b_i^\dagger) are standard bosonic annihilation (creation) operators, $n_i = b_i^\dagger b_i$ count the boson numbers on site i and $V_{ij} = V(\mathbf{r}_{ij})$ and $W_{ijk} = W(\mathbf{r}_i, \mathbf{r}_j, \mathbf{r}_k)$ denote the two- and three-body couplings. The hopping term in Equation (1.17) is restricted to nearest-neighbors $\langle ij \rangle$ only.

The Hamiltonian, given in Equation (1.17), will be subject to detailed numerical studies. In Chapter 5, the triangular lattice supersolid, that has been introduced in Section 1.4, is revisited. The internal structure of the supersolid phases is determined by the underlying \mathbb{Z}_q symmetries and particle-hole symmetry around $\mu/V = 3$. Short-range and extended two- and three-body interactions break this symmetry explicitly and the question is raised whether the features of the two-body nearest neighbor model can still be observed in a regime with more complex potentials.

After discussing the triangular supersolid, Chapter 6 will focus on the hardcore Bose-Hubbard model on the honeycomb lattice. Nearest-neighbor three-body interactions, that can be expressed as plaquette interactions in the triangular lattice, now give rise to frustration and a rich classical and quantum phase diagram. The quantum regime is dominated by a variety of valence bond solids (VBS) that arise from an order-by-disorder effect [143] out of the highly degenerate classical manifold. The competition of W - and V -terms in Equation (1.17) leads to a cascaded transition into a checkerboard solid and classical and quantum algorithms as well as a novel tensor real space renormalization scheme, that will be discussed in detail in Section 2.2, will be applied to this problem. The results of this discussion can also be found in a publication in *New Journal of Physics* [144].

1.6. Experimental Probes in Cold Gases

Although the phase diagrams of the discussed models are interesting by themselves from a statistical physics point of view, the perspective towards the experimental realization of the given model systems is an important issue. By shortly listing some experimental possibilities towards accessing the nature of superfluid, solid, supersolid and valence bond solid phases, it will become clear that the phenomenology of the discussed models can actually be accessed in recent experiments.

Besides tailoring the interactions and preparing the system, accessing the phase diagram is one of the main challenges that have to be overcome by experimental physicists. The phases discussed so far in the previous sections can be divided into two classes. First, the superfluid is gapless and features frictionless mass flow and (quasi) long range phase correlations. In addition to that, insulators or solids are incompressible ($\partial n / \partial \mu = 0$) and have a gap. For the soft-core model presented in Equation (1.17), the excitation gap is given by $|U|$ whereas in the triangular solid, see Section 1.4 and 1.5, it is of order $V + W$. On top of that, the solid has diagonal long range order $S(\mathbf{Q})$ at some non-trivial momentum.

In condensed matter physics, one has direct access to the response of the system to an external field [145]. For instance, one can distinguish a (super) conductor from an insulator by applying a voltage and measure the current / response of the system. The spectrum of the electron gas can be obtained using angular resolved photo emission spectroscopy (ARPES). Solid order can be accessed by neutron scattering or other crystallographic methods.

The methods used in modern atomic and molecular optics are different since the standard methods of condensed matter physics are not feasible for optical lattice systems. Since the first preparation of a BEC in 1995 [2–4], time-of-flight imaging has proven to be an essential probe for the detection of phase coherence. The basic idea is to prepare the system in some state and then suddenly turn off all confining potentials. After the system has evolved for some time, an absorption image is taken by shining in resonant laser light and recording the shadow of the atomic cloud with a CCD camera. Neglecting the initial size of the cloud (far-field approximation), the contrast of the time-of-flight (TOF) image resembles the momentum distribution of the state before the external

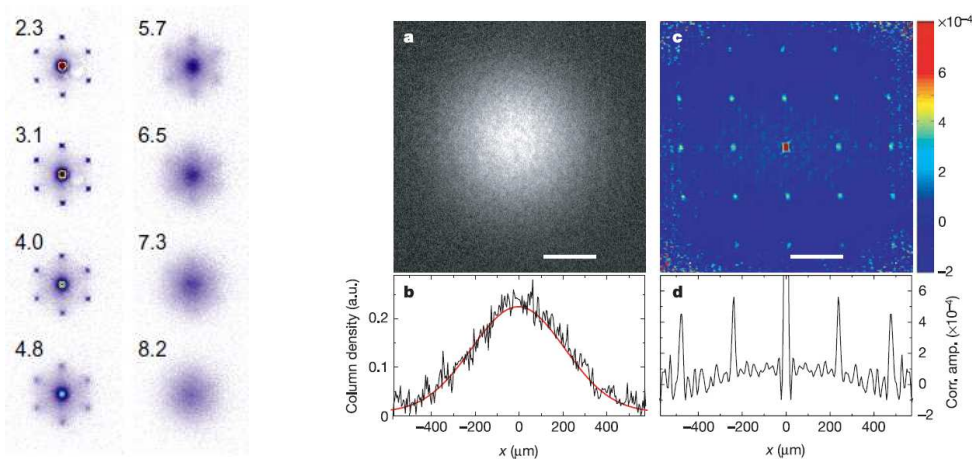


Figure 1.6.: **(Left)** TOF image as a function of lattice depths in a triangular optical lattice. For shallow lattices, one clearly sees the hexagonal structure of the reciprocal lattice in the interference pattern of the superfluid. As the system is driven towards the insulating regime (right column) the interference pattern vanishes and the density distribution resembles a Gaussian. Picture taken from [32]. **(Right:)** Density (a,b) and noise correlations (b,d) for a square-lattice Mott insulator measured after a free expansion by Fölling *et al.* [148].

potentials were turned off. In particular, the density distribution of the cloud after expanding for a time t is given as

$$n(\mathbf{x}) \propto G^1(M\mathbf{x}/t), \quad (1.18)$$

where M is the atomic mass and $G^1(\mathbf{k})$ is the momentum resolved single particle Green's function [16, 146]. For instance, the left hand side of Figure 1.6 shows the absorption image for the superfluid and Mott regime for a triangular lattice. In the former case, the interference fringes resemble the hexagonal structure of the reciprocal lattice whereas the interference pattern of the Mott phase is Gaussian from the superposition of incoherent particles localized at the sites of the optical lattice. Recent simulations show a remarkable agreement of the TOF image with experimental data [147].

The lack of phase coherence indicated by the loss of the Bragg peaks in the interference pattern in the TOF image suffices to show that the system is not a BEC. However, with respect to the solid phases found for the triangular and honeycomb realization of polar molecules, the detection of the spatial distri-

bution of the constituents in the optical lattice is crucial. Density correlation functions provide further insight into this issue [146]. In direct correspondence of the Hanbury Brown and Twiss setup [149–151], the intensity correlations $\langle n(\mathbf{x})n(\mathbf{x}') \rangle \propto 1 + 1/N^2 |\sum_{\mathbf{R}} \exp^{(\mathbf{x}-\mathbf{x}')\mathbf{R}M/t} n_{\mathbf{R}}|$ are sensitive to diagonal long-range order. In particular, the right hand side of Figure 1.6 shows the TOF image and the second-order correlation function for a square-lattice Mott insulator. Whereas the absorption image only displays a Gaussian distribution, the bunching of the atoms at $\mathbf{Q} = (0, 0)$ is visible in the intensity correlations [148]. Another example for an intensity correlation is given by the k -space ordering pattern of the 9/16 honeycomb VBS exemplified in Figure 6.7. Peaks in the first and second order correlations, obtained from shot-to-shot averages, (Equation (1.18)) can be used to identify the lattice supersolid [79, 152].

Recently, the resolution of single lattice sites in ultra-cold gases experiments offers new possibilities to probe the system directly [33, 153–155]. Solid structures can directly be observed by taking a picture of the atomic arrangement and resonances in the VBS might be also accessible. Moreover, the single site microscopy can also be used to make a holographic projection of an arbitrary laser potential [33]. Thus, the realization of complex lattice structures, normally involving the arrangement of multiple laser beams, is reduced to the production of a holographic image and, moreover, it becomes possible to create flat confining potentials avoiding the “wedding cake” structure usually obtained in harmonically confined systems.

Insight into the excitation spectrum can be obtained from Bragg spectroscopy using lattice shaking, as demonstrated by Stöfferle *et al.* [156]. In this setup, the lattice is modulated with some frequency inducing excitations with energy ν_{mod} . Measuring the amount of energy deposited by the lattice shaking is sensitive to the excitable modes and, thus, might be suitable for the detection of a supersolid.

Experimentally probing short-ranged resonances has been demonstrated by Trotzky *et al.* [157, 158]. They addressed superexchange interactions in a spin mixture of ultracold ^{78}Rb in an effective double-well potential generated by imposing a suitable superlattice. Superexchange leads to spin oscillations in time that can effectively be modeled, in the simplest case, by a two-site Bose-Hubbard model. This method can, in general, also be used to probe more complex res-

onating states like resonating valence bonds [159].

In principle, resonances in the VBS, discussed in Section 1.5 (see Chapter 6 for a detailed description), can be accessed using single-site addressability, Bragg spectroscopy or superlattice methods. However, the time scales of the resonance processes are important for the practical implementation of these detection schemes in experimental systems. For instance, a very fast resonance will always be “smeared out” in the images obtained from time resolved single site spectroscopy and the explicit hopping processes can not be observed directly. Thus, the feasibility of the aforementioned methods for the detection of complex resonant structures has to be considered for a concrete model system explicitly but has, so far, not been addressed in detail.

Two dimensional superfluids do not exhibit ODLRO at $T > 0$ but the physics is governed by a quasi long-range ordered critical theory. At large temperatures, a vortex unbinding transition, also referred to as Berezinskii-Kosterlitz-Thouless transition, takes place. The detection of topological vertex defects and the measurement of their vortex charge are crucial for the detection of half-vortices governing the physics of the pairsuperfluid described in Section 1.3. Using absorption images, Hadzibabic *et al.* demonstrate the detection of vortices in a two dimensional quantum degenerate Bose gas [160]. The proliferation of vortices can be identified by sharp dislocation in the interference pattern of two overlapping superfluids measuring phase [160–162]. The vorticity can be directly accessed using spinor condensates by spatially resolving the spinor orientation. From this information, the vorticity can be directly observed in situ [163].

2. Methods

2.1. Quantum Monte Carlo

The Metropolis-Hastings algorithm [164, 165] introduced in 1953, intended to calculate the equation of state for a two-dimensional Lennard-Jones gas of hard spheres, opened up a new era of numerical calculations. These days, the Monte Carlo method is one of the most powerful computational techniques [166] with applications to a vast variety of problem as protein folding [167], optimization algorithms [168, 169] and statistical physics [170].

In statistical physics, one faces systems with an exponentially large number of degrees of freedom. Consider, for instance, an Ising model on a square lattice with $N = 100$ sites and temperature $T = 1/\beta$. The evaluation of the partition function

$$Z = \sum_{\text{states } i} e^{-\beta E_i} \quad (2.1)$$

would involve the summation of $2^{100} \approx 10^{30}$ Boltzmann factors. The concept of Markov chain Monte Carlo is the stochastic sampling of an exponentially large phase space by creating a Markov process. Based on the idea of importance sampling [170], the steady state distribution of the Markov process should resemble the probability of the system to be found in the particular state given by the weight of each configuration e.g., the Boltzmann distribution for a classical system. Formally, the Markov process can be described by a master equation [170]

$$\frac{\Delta \mathbf{W}(t)}{\Delta t} = \mathbf{W}(t)P - P\mathbf{W}(t), \quad (2.2)$$

where the matrix P contains the transition probabilities from state i to state j ,

2. Methods

P_{ij} , and \mathbf{W} contains the weights of each configuration, W_i . Inserting the physical weights as the steady-state distribution function into Equation (2.2), one obtains an equation for the yet unknown transition matrix, namely

$$\sum_{ij} W_{ij} P_i = \sum_{ij} P_j W_{ij}. \quad (2.3)$$

One solution of this equation can be obtained by requiring that Equation (2.3) holds for every pair of summands. This condition is also referred to as detailed balance,

$$W_{ij} P_i = P_j W_{ij}, \quad \forall i, j. \quad (2.4)$$

Equation (2.4) has the form of a continuity equation stating that there is no net flow of probability. The stochastic nature of this process entails that a finite sampling will not give the exact value of the quantities of interest such as energy or particle number. In particular, Monte Carlo algorithms, provided they do not suffer from the notorious sign problem [171] i.e., $P_i \geq 0$ for all i , scale polynomially in the number of degrees of freedom, controlled by the lattice size, whereas the configuration space scales exponentially¹. Thus, the finite-size and sampling error, scaling like $1/\sqrt{N_{\text{samples}}}$, can be reduced systematically in polynomial time.

2.1.1. Generalized Directed Loop Algorithm in the Stochastic Series Expansion

The starting point for the derivation of the directed loop algorithm [172–176], that can be seen as a generalization the Handscomb method [177], is the series expansion of the partition function of a quantum mechanical system at temper-

¹Formally speaking, the Monte Carlo algorithm is in the complexity class bounded-error probabilistic polynomially (BPP) [171].

ature $T = 1/\beta$, whose dynamics is generated by a Hamilton operator H ,

$$Z = \text{Tr} e^{-\beta H} \quad (2.5)$$

$$= \sum_{|\alpha\rangle} \sum_{n=0}^{\infty} \frac{\beta^n}{n!} \langle \alpha | (-H)^n | \alpha \rangle. \quad (2.6)$$

The set $\{|\alpha\rangle\}$ is an orthonormal basis of the Hilbert space. The following discussion will be restricted to d -dimensional lattice systems with linear extend L containing $N \propto L^d$ sites. In particular, periodic boundary conditions are imposed in all lattice directions unless stated otherwise. The Hamiltonian has to be separable into a sum $H = -\sum_{\text{vertices } v} H_v$, where H_v denotes an interaction vertex where the number of sites on each vertex, N_{legs} , is small compared to the total number of lattice sites N .² For the class of Bose-Hubbard models, the Hamiltonian will contain hopping terms between nearest-neighbors, on-site interactions like a chemical potential, μn_i , and density interaction terms reading $V_{ijk\dots} n_i n_j n_k \dots$. The basis $\{|\alpha\rangle\}$ is the occupation number basis $\{|n_i n_j n_k \dots\rangle\}$, where $n_i = b_i^\dagger b_i$ denotes the density operator for lattice site i , and $|\alpha\rangle$ will, in the following, represent some boson configuration on the lattice. Thus, hopping terms will be referred to as ‘‘off-diagonal’’ operators H^{od} whereas potential terms are ‘‘diagonal’’ H^{d} . Inserting the vertex decomposition into the Hamilton matrix element in Equation (2.6) yields

$$\sum_{|\alpha\rangle} \langle \alpha | (-H)^m | \alpha \rangle = \sum_{|\alpha\rangle} \langle \alpha | \left(\sum_v H_v \right)^m | \alpha \rangle \quad (2.7)$$

$$= \sum_{|\alpha\rangle} \sum_{\{v_1, \dots, v_m\}} \langle \alpha | \prod_{p=1}^m H_{v_p} | \alpha \rangle \quad (2.8)$$

$$= \sum_{\{|\alpha(1)\rangle, \dots, |\alpha(m)\rangle\}} \sum_{\{v_1, \dots, v_m\}} \prod_{p=1}^m \langle \alpha(p) | H_{v_p} | \alpha(p-1) \rangle. \quad (2.9)$$

The subscript $\{v_1, \dots, v_m\}$ in Equation (2.8) denotes the summation over all combinations of vertices. A full set of basis is inserted between each pair of vertex operators in Equation (2.9) such that $|\alpha(0)\rangle = |\alpha(p)\rangle$. By inserting $(\Lambda - n)$ unit

²In particular, the number of interacting partners per lattice site is intensive. The case of long-range interactions i.e., where the number of interaction partners scales like the number of lattice sites N , will be considered in Section 3.3.2.

2. Methods

operators, $H_0 = \mathbb{1}$, one can extend the operator sequence $\{v_1, \dots, v_\Lambda\}$ to include $m = \Lambda$ elements. Introducing a cut-off Λ for the expansion order and extending each operator list to have Λ elements, the partition function reads

$$Z = \sum_{n=0}^{\Lambda} \sum_{\{\alpha(1)\}, \dots, \{\alpha(\Lambda)\}} \sum_{\{v_1, \dots, v_\Lambda\}} \underbrace{\frac{\beta^n (\Lambda - n)!}{\Lambda!} \prod_{p=1}^{\Lambda} \langle H_{v_p} \rangle}_{W(v_1, \dots, v_\Lambda)} \quad (2.10)$$

where $\langle H_{v_p} \rangle = \langle \alpha(p) | H_{v_p} | \alpha(p-1) \rangle$. The product in Equation (2.10) is referred to as operator string and has a graphical representation similar to the concept of world lines in the path-integral formulation of the worm algorithm [178–183], as shown in Figure 2.1. It constitutes the mapping from a d -dimensional quantum system to a $d + 1$ -dimensional classical system where the system is extended into imaginary time periodic in β .³ Thus, one can think of a vertex as a pair $[H_v | n_{\sigma_1} n_{\sigma_2} \dots n_{\sigma_{N_{\text{legs}}}}]$, where the n_{σ_i} are the occupation numbers of state $|\alpha(p-1)\rangle$ and $|\alpha(p)\rangle$ for $i \leq N_{\text{legs}}$ and $i > N_{\text{legs}}$, respectively. The cut-off Λ introduces a systematic error. However, as it will be shown in Section 2.1.2, the expectation value of the expansion order is proportional to the energy of the system, $\langle n \rangle = -\beta \langle H \rangle$. In particular, the leading contributions reside in a small windows around $\langle n \rangle$. Choosing $\Lambda \gg \langle n \rangle$ ensures that the systematic error is well below the numerical accuracy of the algorithm and Λ will be adapted during the thermalization of the system [176, 184].

The directed loop algorithm evaluates the partition function given in Equation (2.10) by sampling all operator strings given that all matrix elements $\langle \alpha(p) | H_{v_p} | \alpha(p-1) \rangle \geq 0$ assuring that the weights for all configurations are positive semi-definite. This can be achieved for diagonal operators by adding a constant $H_v^d + C + \epsilon$ with $C = \min_{|\alpha\rangle} \{ \langle \alpha | H_v^d | \alpha \rangle \}$ and $\epsilon > 0$ ensures that all vertices have a finite weight (ergodicity). Since this modification is only possible for diagonal operators, the application of the SSE algorithm is restricted to problems where the off-diagonal part of the Hamiltonian fulfill $\langle \alpha | H_v^{\text{od}} | \beta \rangle > 0$. This is the case for ferromagnetic exchange couplings or antiferromagnetic coupling

³The SSE operator levels do not correspond to a specific point in imaginary time as in the worm algorithm [180–183]. Nevertheless, one can derive the SSE algorithm from the path integral formalism by using the whole Hamiltonian as a perturbation.

on bipartite lattices since the sign of the off-diagonal exchange term can always be altered by a sublattice rotation.

The update process acting on the operator string has to change the expansion order n by inserting or removing operators and update the vertices themselves. It should also be noted, that the computational effort of this algorithm scales with the volume of the $d + 1$ dimensional classical system i.e., linearly in $1/\beta$ and L^d .

Diagonal Update

Changing the expansion order corresponds to either replacing a unit operator by a diagonal interaction vertex, $\mathbb{1} \rightarrow H_v^d$, or vice versa. The removal of v_x , for instance, modifies the vertex list as $(v_1, \dots, v_x, \dots, v_\Lambda) \rightarrow (v_1, \dots, 0, \dots, v_\Lambda)$. The transition is required to fulfill detailed balance, see Equation (2.4), with weights $W(v_1, \dots, v_\Lambda)$ given in Equation (2.10). The transition rates for inserting or removing a diagonal operator at level p read

$$P(\mathbb{1} \rightarrow H_v^d) = \min \left[1, \frac{N_v \beta \langle H_{v_p}^d \rangle}{\Lambda - n} \right] \quad (2.11)$$

$$P(H^d \rightarrow \mathbb{1}) = \min \left[1, \frac{(\Lambda - n + 1) \delta_{|\alpha(p-1)|, |\alpha(p)|}}{N_v \beta \langle H_{v_p}^d \rangle} \right]. \quad (2.12)$$

Off-diagonal Update

The off-diagonal update keeps the expansion order constant but alters the interaction vertices. One important constraint of the update is that the periodicity of the operator string has to be conserved thus local updates e.g., inserting a particle at some vertex, is not feasible and will inevitably lead to configurations with zero weight. A particular type of cluster update is the construction of directed loops. A loop is constructed by spawning a “worm” at some point in the $(d + 1)$ dimensional lattice and supplying the worm with a bosonic operator $\hat{O} = (b^{(\dagger)})^m$ i.e., the worm can create/annihilate m bosons and will act with \hat{O} on each state it encounters. The head of the worm is able to move along the time direction (“up” or “down”) along the operator string. If it encounters an interaction vertex at level p at site σ_i , the worm can either branch, go straight or bounce thus changing

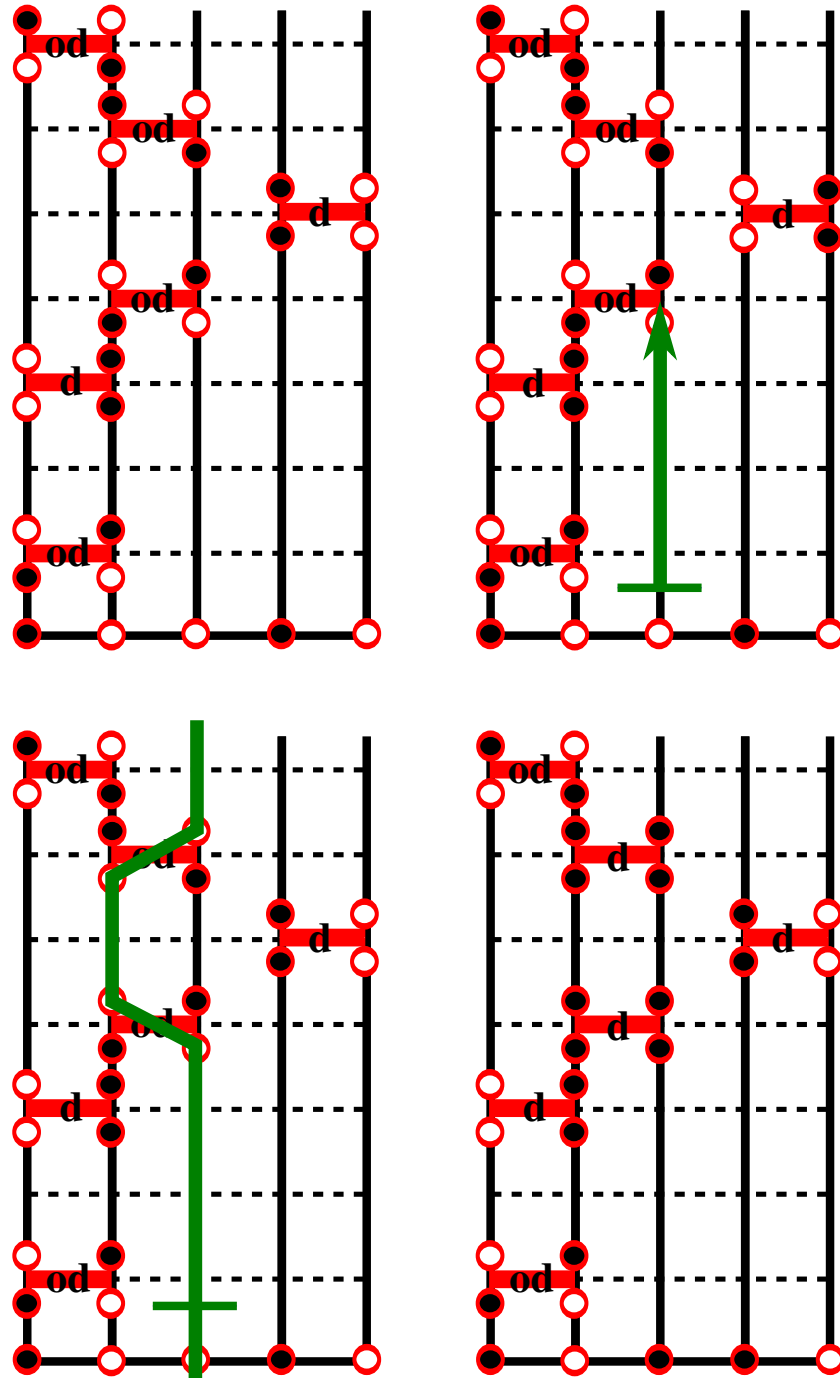


Figure 2.1.: (from left to right and top to bottom) Schematic representation of an operator string of length 8. A worm (green) with is spawned at level 1 at site 3 and is traversed until it reaches an operator at level 5 scattering to site 2 and moves up until is finally closes changing all states it traverses creating a new configuration.

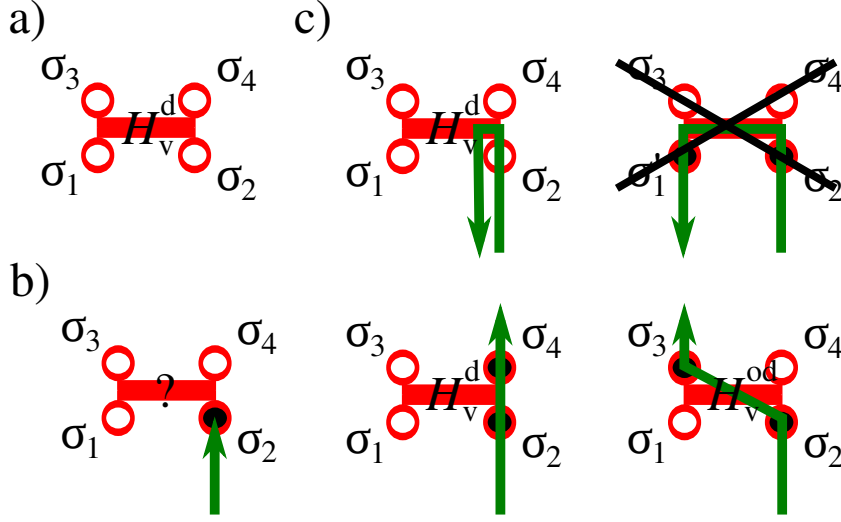


Figure 2.2.: a) Four-leg vertex $(n_{\sigma_1}, n_{\sigma_2}, n_{\sigma_3}, n_{\sigma_4})$ with diagonal Hamiltonian. b) Worm with operator \hat{O} enters leg 2; $n_{\sigma_2} \rightarrow \hat{O}n_{\sigma_2}$. c) Four possibilities to choose the exit leg of the worm updating the Hamiltonian.

the local vertices $[H_v | n_{\sigma_1} n_{\sigma_2} \dots n_{\sigma_{N_{\text{legs}}}}] \rightarrow [H'_v | n_{\sigma_1} n_{\sigma_2} \dots n'_{\sigma_{l_{\text{in}}}} \dots n'_{\sigma_{l_{\text{out}}}} \dots n_{\sigma_{N_{\text{legs}}}}]$, where l_{in} and l_{out} denote the entrance and exit leg of the worm and $n'_{\text{in}} = \hat{O}n_{\text{in}}$ and $n'_{\text{out}} = \hat{O}'n_{\text{out}}$, where \hat{O}' will be detailed below. An example of a scattering process is shown in Figure 2.2. If the worm changes its propagation direction, one has to substitute $\hat{O} \rightarrow \hat{O}^\dagger$, since particle number is conserved at each vertex, and $\hat{O}' = \hat{O}^\dagger$, $\hat{O}' = \hat{O}$ otherwise.. A special case is the “bounce” process, where $l_{\text{in}} = l_{\text{out}}$ and the worm undoes its previous steps. The scattering probabilities for a given l_{in} , $W_{l_{\text{in}}, l_{\text{out}}}$, are determined by the detailed balance condition in Equation (2.4) where the weights are given by the matrix element of the new interaction vertex

$$W_v(l_{\text{in}}, l_{\text{out}}) = \langle [H'_v | n_{\sigma_1} n_{\sigma_2} \dots n'_{\sigma_{l_{\text{in}}}} \dots n'_{\sigma_{l_{\text{out}}}} \dots n_{\sigma_{N_{\text{legs}}}}] \rangle. \quad (2.13)$$

After the vertex has been updated, the worm continues propagating until it reaches a new interaction vertex or returns to its starting point (“bites its tail”) and the update terminates. Thus, the construction of the directed loop can be summarized as follows:

- Spawn worm at site i and level l
- Choose operator $\hat{O} = (b^{(\dagger)})^m$ from a uniform distribution.

2. Methods

- Choose random propagation direction.
- Propagate worm head until it reaches an interaction vertex.
- Scatter and update interaction vertex.
- Continue propagation, until reaching a new interaction vertex or terminating the update by returning to the starting point.

Scattering Probabilities So far, the construction of the scattering probabilities has not been specified. One choice that fulfills detailed balance is given by the Heat-Bath solutions

$$P_{l_{\text{in}}, l_{\text{out}}} = \frac{W_v(l_{\text{in}}, l_{\text{out}})}{\sum_l W_v(l_{\text{in}}, l)}. \quad (2.14)$$

However, one can optimize the scattering probabilities in order to minimize autocorrelation times thus enhancing the efficiency of the update.

One strategy is the minimization of bounce processes [176] (minbounce) where the worm will tend to undo its changes and waste computer time. Thus, the set of detailed balance equations are optimized numerically with respect to the minimization of all diagonal scattering matrix elements $\sum_i P_{ii}$. This strategy is found to be superior to the Heat-Bath solutions in Equation (2.14) and particularly effective for large chemical potentials μ . This can be understood since a large chemical potential (or large magnetic field, as in the original paper by Alet *et al.* [176]) will lead to large weights of the diagonal configurations hence scattering events to off-diagonal operators will be suppressed by a large denominator in Equation (2.14). The numerical optimization is performed using the `lpsolve` [185] library.

A second strategy used in this work is based on the concept of optimal Monte Carlo updates (locopt) by Pollet *et al.* [186, 187]. Based on the Heat-Bath solutions, they iteratively construct - “Metropolize“ - solutions of the scattering matrix minimizing the higher eigenvalues of the transition matrix (see Equation (A.2)). This method has the advantage that one is not depended on a linear optimization hence the implementation of the locally-optimal scattering probabilities is much simpler and increases the portability of the program code. A detailed

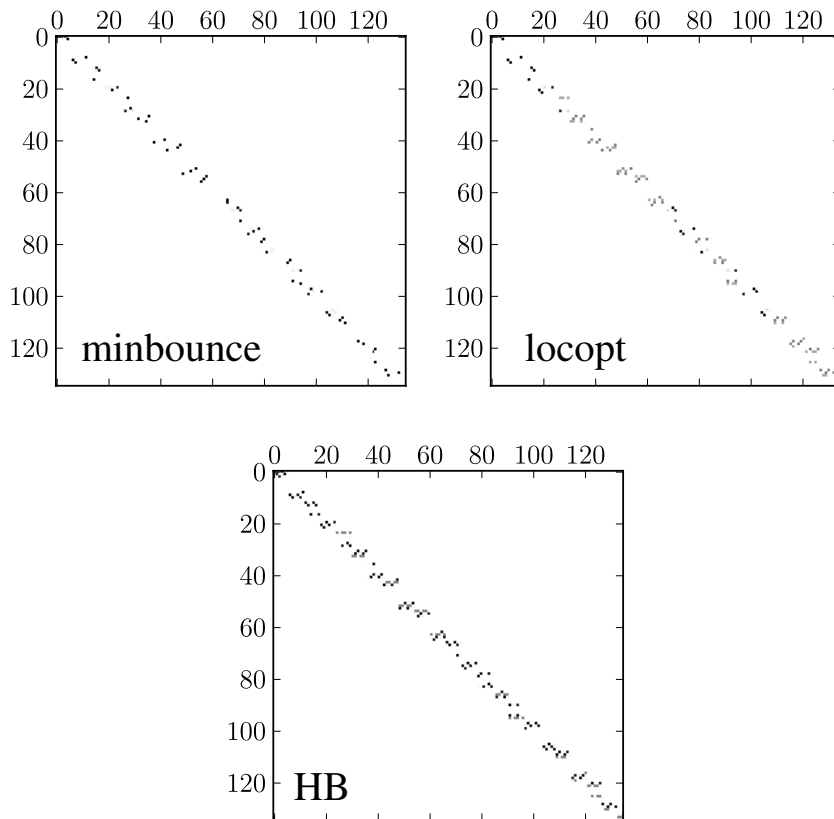


Figure 2.3.: Graphical representation of the scattering matrices for bounce minimization, local optimal scattering matrices and Heat-Bath for $t/V = 0.2$ and $\mu/V = 3$ in the hardcore triangular problem. The enumeration for the scattering probabilities for a vertex v , $P_{l_{\text{in}}, l_{\text{out}}}^v$, are given at coordinate $((l_{\text{in}} - 1)v + l_{\text{out}}, (l_{\text{in}} - 1)v)$. The scattering probability is encoded in the gray scale where white denotes zero probability and black probability 1.

summary of the construction of the scattering matrix can be found in Appendix A.

Both solutions are superior to the Heat-Bath solutions and perform equally well (at least for the Bose-Hubbard and Spin-3/2 chain [186]). For better comparison, Figure 2.3 shows a matrix plot of the scattering probabilities using the three different approaches. The minbounce updates clearly favor off-diagonal updates and has a strong selection on the allowed transitions whereas the locopt ansatz allows for more scattering probabilities. Throughout this work, minbounce and locopt scattering solutions are used and none is found to be advantageous in terms of performance.

2.1.2. Measuring Physical Observables

Estimators for Thermodynamic Expectation Values:

A general expression for the evaluation for the expectation value for an operator \hat{O} is given by

$$\langle \hat{O} \rangle = \frac{\text{Tr } \hat{O} e^{-\beta H}}{Z} = \sum_{n=0}^{\Lambda} \sum_{|\alpha\rangle} \sum_{\{v_1, \dots, v_m\}} \frac{\beta^n (\Lambda - n)!}{\Lambda!} \langle \alpha | \hat{O} \prod_{p=1}^m H_{v_p} | \alpha \rangle. \quad (2.15)$$

If the operator \hat{O} can be expressed in terms of m elementary excitations e.g., the total energy, $\langle H \rangle$, the kinetic energy $\langle H^{\text{od}} \rangle$ or the squared energy $\langle H^2 \rangle$, Equation (2.15) reduces to

$$\langle \hat{O}^m \rangle = \langle n^m \frac{(n-1)!}{(-\beta)^m (n-m)!} \rangle. \quad (2.16)$$

n^m counts the number of occurrences of the operator \hat{O}^m in the operator string. For example, the bond kinetic energy correlation $K_{\langle ij \rangle; \langle kl \rangle} = b_i^\dagger b_j b_k^\dagger b_l$ counts the number of occurrences of a hopping event on bond (ij) directly followed (except unit operators) by a hopping event on bond (kl) . In particular, the estimators

for the total, kinetic and potential energy of the system read

$$E = -\frac{\langle n \rangle}{\beta} + C + \epsilon \quad (2.17)$$

$$E^{\text{kin}} = -\frac{\langle n^{\text{od}} \rangle}{\beta} \quad (2.18)$$

$$E^{\text{pot}} = -\frac{\langle n^{\text{d}} \rangle}{\beta} + C + \epsilon \quad (2.19)$$

where $\langle n \rangle$ is the total number of elements in the operator string and $\langle n^{\text{od/d}} \rangle$ counts the number of (off-) diagonal operators [188]. Thus, the specific heat C_v reads [188]

$$C_v = \beta^2(\langle n^2 \rangle - \langle n \rangle^2 - \langle n \rangle). \quad (2.20)$$

Diagonal quantities like the density $1/N \sum_{\text{sites } i} n_i$ density correlations and structure factors can be accessed directly via the state $|\alpha(0)\rangle$. Though it is possible to average over all operator levels, one usually has strong autocorrelation and it suffices to measure those quantities only at the one state.

Finally, the estimator for the susceptibility is given as [188]

$$\chi = \int_0^\beta \langle \hat{O}_1(0) \hat{O}_2(\tau) \rangle d\tau \quad (2.21)$$

$$= \left\langle \frac{\beta}{n(n+1)} \left(\sum_{l=0}^{n-1} \hat{O}_1[l] \right) \left(\sum_{l=0}^{n-1} \hat{O}_2[l] \right) + \frac{\beta}{(n+1)^2} \sum_{l=0}^n \hat{O}_1[l] \hat{O}_2[l] \right\rangle \quad (2.22)$$

Superfluid Density:

The superfluid density, ρ_s , can be accessed through the response of the system to an artificial gauge-field threading the torus a system with periodic boundary conditions [189, 190]. This can also be thought of as employing twisted boundary conditions where the bosons acquire a phase when crossing the boundary of the system.⁴ In an gedankenexperiment, the source of this gauge-field is the rotation

⁴As pointed out by Prokof'ev and Boninsegni [189], the definition of the superfluid density is ambiguous in terms of the response of the system to twisted boundary conditions or by the kinetic term in the low-energy theory ($F = \int \rho_s/2(\nabla\phi)^2$). However, the difference of the two superfluid densities is negligible in two or more dimensions. In particular, the difference of the two definitions yields a constant factor $\sim 10^{-4}$ in two dimensions and will be discarded.

2. Methods

of a very large cylinder the superfluid is confined to. The superfluid density is then given by

$$\rho_s = \frac{m \langle W^2 \rangle}{L^{d-2} \beta}, \quad (2.23)$$

where m is the effective mass and $\langle W^2 \rangle$ are the winding numbers counting the number of bosons passing through the periodic boundary conditions [189, 190]. A detailed derivation of this estimator for the two-dimensional Bose-Hubbard model in the presence of pair-hopping is given in Appendix B.

Green's functions:

The measurement of Green's functions

$$G_m(i, j; \tau) = \langle (b_i^\dagger(0))^m (b_j(\tau))^m \rangle \quad (2.24)$$

is fundamentally different from the aforementioned estimators since it can not be accessed via a given operator string because the operator in Equation (2.24) corresponds to a local change in the occupation numbers. Since this work is only concerned with equal time Green's functions, the discussion is restricted to the case $\tau = 0$.⁵ However, $G_m(i, j; 0) = G_m(i, j)$ can be accessed during the construction of the directed loop. The worm carrying the operator $(b^{(\dagger)})^m$ is inserted at some site i level l and that does not necessarily contains an interaction vertex. As the worm passes through this level during the construction of the operator string the matrix element $w^m(ij) = \langle \tilde{\alpha}(l') | (b_i^\dagger)^m b_j^m | \tilde{\alpha}(l'') \rangle$ is recorded. If the worm is traveling in a positive direction $l' = l$ and $l'' = l - 1, l'' = l + 1$ otherwise. The estimator for the the Green's function is then given as

$$G^m(ij) = \langle w^m(ij) \rangle. \quad (2.25)$$

Thus, the off-diagonal update resembles the propagator of the physical system. It should also be noted that the evaluation of higher order Green's functions, namely $m > 1$, requires multi-particle updates. Generic problems and further

⁵A detailed description of the effective implementation of dynamic estimators is presented by Dorneich and Troyer [188].

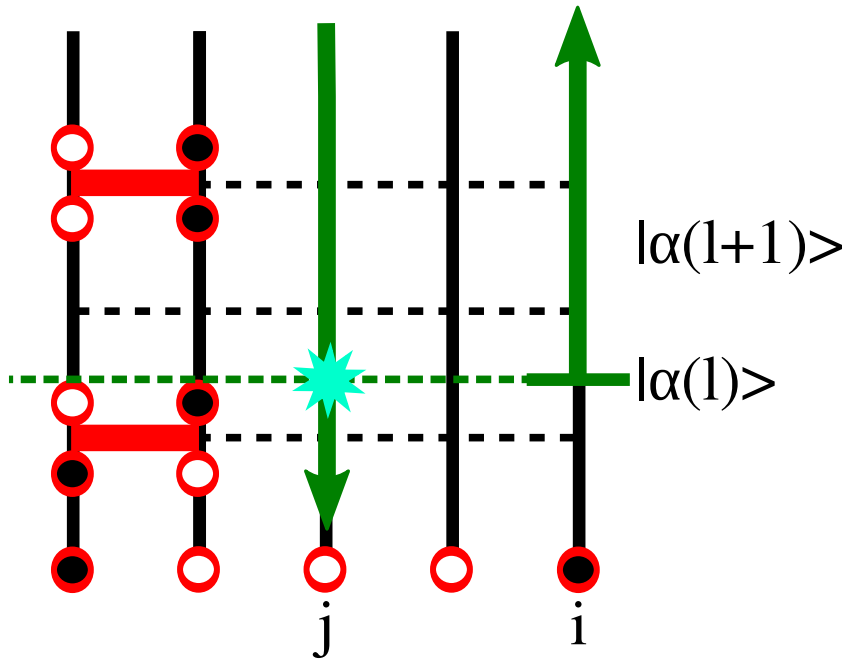


Figure 2.4.: Measurement of the Green's function $G(ij)$.

improvements of this estimator in terms of multiworms will be discussed in Chapter 3.5.

Error Estimation

Whereas the expectation value of some operator A can be determined directly from the sequence of measurements $\{A_i\}_{i=1}^{N_{\text{mc}}}$ generated by the Markov process,

$$\langle A \rangle = \frac{1}{N_{\text{mc}}} \sum_{i=1}^{N_{\text{mc}}} A_i, \quad (2.26)$$

the estimation of the error needs some attention. Since the A_i 's are correlated, the naive formula for the standard deviation,

$$\Delta A = \sqrt{1/[N_{\text{mc}}(N_{\text{mc}} - 1)](\langle A^2 \rangle - \langle A \rangle^2)}, \quad (2.27)$$

will underestimate the error. The integrated autocorrelation time can be obtained from a binning analysis [191], reading

$$\tau_A^{\text{int}} = \frac{1}{2} \left[\left(\frac{\lim_{n \rightarrow \infty} \Delta A^{(n)}}{\Delta A^{(0)}} \right)^2 - 1 \right]. \quad (2.28)$$

Here, $\Delta A^{(n)}$ denotes the error of the n th binning level. The true error of $\langle A \rangle$ is obtained by the saturation value of $\Delta A^{(n)}$ as $n \rightarrow \infty$.

The same applies for the evaluating of functions $\langle f(A, B) \rangle$ of observables such as the Binder ratio $\langle M^4 \rangle / \langle M^2 \rangle^2$ because Gaussian error propagation breaks down due to auto- and cross-correlations. The actual implementation utilized in this work performs a jackknife analysis for the error estimation of composite quantities [192].

2.1.3. Quantum Parallel Tempering

Exponentially large autocorrelation times in the presence of rough entropy landscapes with large entropic barriers, as they are found in problems like structure determination in material science [193], protein folding [194] or spin glasses [195], lead to the invention of a extended ensemble approaches like Wang-Landau sampling [196–198], replica Monte Carlo [199] or simulated tempering⁶ [201]. As the aforementioned methods, parallel tempering is based on the idea of an extended configuration space [199, 202–205]. Several replicas of the system are simulated at different set of parameters. In a second Monte Carlo update, that will be denoted as a global update, the replicas can switch positions in parameter space. This allows for a frozen system trapped in a local minimum of the potential landscape to diffuse to higher temperatures and relax with a much higher rate to the true thermodynamic state and then return to the parameter range with slow dynamics. In this way, one can circumvent dynamical freezing of the algorithm. Classically, the swap probabilities of two neighboring systems, Σ_i and Σ_{i+1} at different temperatures T_i and T_{i+1} are obtained from the detailed balance

⁶For a direct comparison of simulated and parallel tempering see also Ref. [200].

equation,

$$P([\Sigma_i, T_i] \rightarrow [\Sigma_i, T_{i+1}]) = \min(1, e^{\Delta\beta\Delta E}) \quad (2.29)$$

with $\Delta E = E_i - E_{i+1}$ and $\Delta\beta = 1/T_i - 1/T_{i+1}$. Quantum parallel tempering [203] allows for the extension of the configuration space not only in temperature but also in the coupling constant, $\kappa_i = T_i, \mu_i, t_i, \dots$. For the stochastic series expansion, one can insert the weights of the configuration, given by the product over the operator string of all vertices (see Equation (2.10)) into Equation (2.4) and obtains

$$P([\Sigma_i, \kappa_i] \rightarrow [\Sigma_i, \kappa_{i+1}]) = \min\left(1, \frac{W(\Sigma_i, \kappa_{i+1})W(\Sigma_{i+1}, \kappa_i)}{W(\Sigma_i, \kappa_i)W(\Sigma_{i+1}, \kappa_{i+1})}\right). \quad (2.30)$$

To be precise, $P([\Sigma_i, \kappa_i] \rightarrow [\Sigma_i, \kappa_{i+1}])$ actually denotes the transitions $[\Sigma_i, \kappa_i] \rightarrow [\Sigma_i, \kappa_{i+1}]$ and $[\Sigma_{i+1}, \kappa_{i+1}] \rightarrow [\Sigma_{i+1}, \kappa_i]$ but the latter expression is omitted for the sake of brevity. $W(\Sigma_i, \kappa_j)$ is the weight of the operator string of system i evaluated with the coupling constant κ_j . In general, this constitutes to the evaluation of $n_i \times n_{i+1}$ products. For specific cases, simple expressions for Equation (2.30) can be derived, though. First, consider parallel tempering in the temperature, $\kappa_i = T_i$. The vertex weights are unaffected by a change in parameter and only the prefactor β^n changes and the transition probability reads

$$P^T([\Sigma_i, T_i] \rightarrow [\Sigma_i, T_{i+1}]) = \min\left(1, T_i^{n_i - n_{i+1}} T_{i+1}^{n_{i+1} - n_i}\right). \quad (2.31)$$

For a hardcore boson model, where all hopping weights are equal to t , Equation (2.30) yields

$$P^t([\Sigma_i, t_i] \rightarrow [\Sigma_i, t_{i+1}]) = \min\left(1, t_{i+1}^{n_i^{\text{od}} - n_{i+1}^{\text{od}}} t_i^{n_{i+1}^{\text{od}} - n_i^{\text{od}}}\right). \quad (2.32)$$

n_i^{od} are the number of off-diagonal operators in the operator string of Σ_i .

The performance of parallel tempering strongly depends on the choice of the parameter set $\{\kappa_i\}$. If the steps between the κ_i are too large the swap probabilities drop substantially and the global update becomes inefficient. Choosing a small step size, on the other hand, will increase the swap rates but the range in

parameter space covered may be too small such that a regime with sufficiently high relaxation rates for the local updates is not reached. There are several schemes of how to optimize the parameter set to get best algorithmic performance in terms of restoring ergodicity and reducing the autocorrelation time. For a system with a constant specific heat a geometric progression of the temperature set ($T_{i+1} - T_i \propto C_V T_i$) is found to be optimal [206] since it will ensure a constant swap rate. In the vicinity of a phase transition, this ansatz will not be the optimal choice and the swap rates show a dip at the phase transition [207]. Katzgraber *et al.* propose an adaptive scheme where the replica diffusivity is maximized by iteratively changing the temperature set [207]. In particular, the temperature distribution will peak around the phase transition, where the dynamics is affected by critical slowing down, to assure transport of systems from one side to another. A different approach models the temperature set from the knowledge of the autocorrelation times [208] and allow for an a priori knowledge calculation of the temperature set. In addition, further extensions of the parallel tempering scheme are available that extend the global update scheme for perform “local” changes in each replica to enhance swap probabilities [209]. It has to be noted that, to the best of the authors knowledge, the performance of quantum parallel tempering in view of the an optimal choice of the parameter set has not been subject to a detailed numerical study and it appears worthwhile to investigate this issue further. In this thesis, in particular in Section 6.1.1, a geometric (T) or flat distribution is used across the first-order phase transition.

2.2. Tensor Network Renormalization Group

Over the last years, methods based on tensor networks, such as Projected Entangled Pair States [210, 211], the Multiscale Entanglement Renormalization Ansatz [212] or the Tensor Entanglement Renormalization Group [213] open a new way of understanding quantum mechanical problems from a information theory perspective. One goal of these approaches is to provide effective algorithms to attack problems that elude themselves from an effective numerical treatment. Most prominently, this are problems having (fermionic) sign problem [171] or are highly frustrated (Kagome antiferromagnet [214]). Recently, the

application of the Density Matrix Renormalization Group (DMRG) [215], that has proven to be a highly effective tool to study open and closed quantum mechanical systems in one dimension, to higher dimensional systems becomes more prominent [214, 216].

Whereas a detailed review of tensor network methods is far beyond the scope of this thesis, the Tensor Network Renormalization Group (TNRG) algorithm, that has been proposed by Levin and Nave [217], is presented in detail. By representing the partition function of a classical system as the contraction of a tensor network, an effective evaluation scheme in terms of an iterative coarse graining procedure is presented. This scheme can be thought of as a real-space renormalization group flow, similar to the block-spin picture presented by Kadanoff [218]. Recent works on classical systems like the triangular lattice Ising model [217, 219] or the Shastry-Sutherland Ising model [220] have proven the applicability of this method. The application of this methods to multibody interactions [144] is discussed in Chapter 6. As already suggested in the paper by Levin and Nave [217], this method can be extended to the evaluation of tensor network states in quantum-mechanical systems [221–223]. For this purpose, Xie *et al.* [222–224] present an extended renormalization procedure called “second RG” that improves the accuracy of the coarse graining of the wave function.

2.2.1. Coarse Graining the Tensor Network

The first step of applying the TNRG is the formulation of the partition function in term of the contraction of a tensor network,

$$Z = \sum_{\text{states } i} e^{-\beta E_i} = \sum_{klmno..} T_{klm}^a T_{lmn}^b T_{mno}^a \dots \quad (2.33)$$

In the case considered here, the tensors $T_{ijk}^{a/b}$ reside on the a/b sublattice of a two-dimensional honeycomb lattice. $T_{ijk}^{a/b}$ is a cyclically symmetric tensor of rank D i.e., $i, j, k = 1 \dots D$. In the following, the tensor is required to be normalized, $|T_{ijk}^{a/b}| \leq 1$ for all $i, j, k =$, i.e., $T_{ijk}^{a/b} = (T_0^{a/b})^{-1} \tilde{T}_{ijk}^{a/b}$ with $T_0^{a/b} = \max_{ijk} \{\tilde{T}_{ijk}^{a/b}\}$. The evaluation of the tensor network is infeasible but it can be approximated by

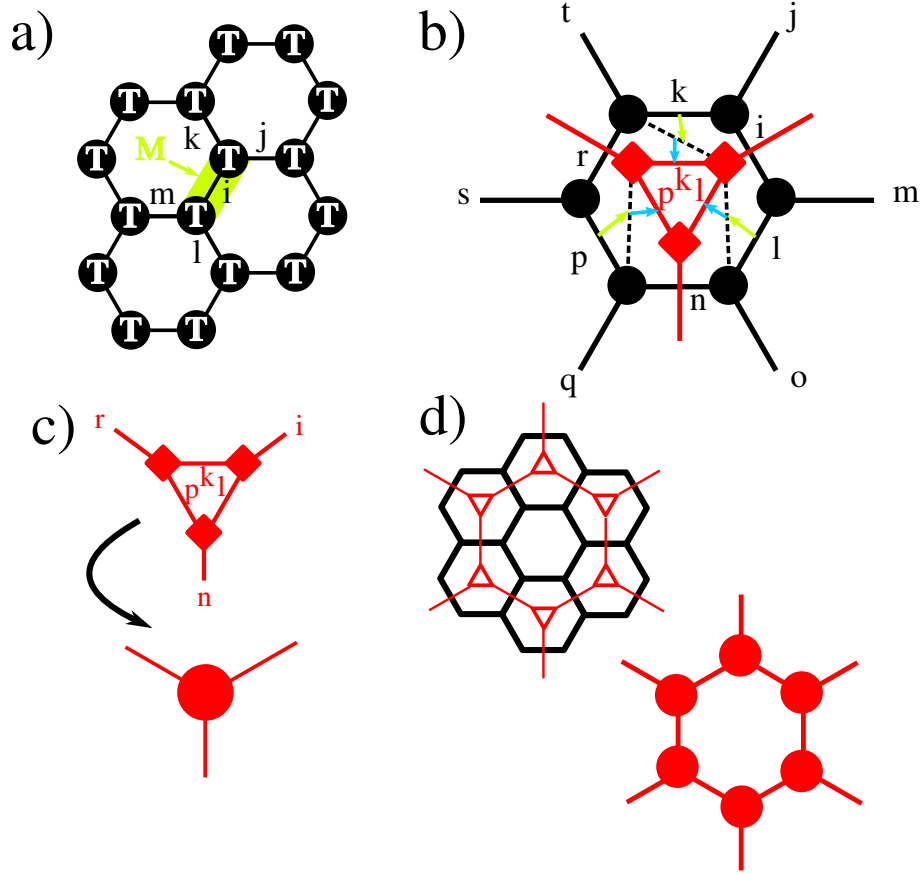


Figure 2.5.: a) The tensors T (dots) live on the sites of a honeycomb lattice and the indices denote bonds. The matrix $M_{jk,lm}$ (green bar) denotes a contraction of two tensors along the shared bond i . b) Contracting the tensors along the bonds of the honeycomb lattice yields three S tensors (red squares). c) Three S tensors are contracted along the inner bonds yielding a new tensor T' living on a honeycomb lattice. d) Schematic drawing of one iteration step. The sublattice indices of the tensors are omitted in this figure.

a coarse graining procedure. The contraction of a tensor along some bond i ,

$$M_{jk,ml} = \sum_{i=1}^D T_{ijk}^a T_{mli}^b \quad (2.34)$$

has a graphical representation, shown in Figure 2.5 a). $M_{ij,kl}$ is a $D^2 \times D^2$ matrix and the row and column indices are accessed as $M_{ij,kl} = M_{Di+j, Dk+l} = M_{\alpha,\beta}$ ⁷. In the first step, Equation (2.34) will be approximated by $S^{a/b}$, that are also real

⁷In the following, Latin indices will run from 1 to D whereas Greek indices cover the range from 1 to D^2 . A combination of Latin and Greek indices denotes $M_{\alpha,c} = M_{ij,0c}$, where $\alpha = Di + j$.

and cyclically symmetric tensors, such that

$$M_{jk,ml} \approx \sum_{i=1}^D S_{kmi}^a S_{lji}^b. \quad (2.35)$$

Performing the contraction along a hexagonal plaquette and introducing the $S^{a/b}$ -tensors (cf. Figure 2.5 b)), a new tensor network is obtained, where the information of the hexagonal plaquette is stored in three S^a or S^b -tensors. Contracting the internal degrees of freedom in a triangular plaquette, one obtains a new honeycomb lattice tensor network, as shown in Figure 2.5 c) and d). In the sense of a real-space RG, this corresponds to a rescaling of $\sqrt{3}$. The (properly normalized) tensors living on the new a and b sublattice in terms of the S tensors read

$$\tilde{T}(n+1)_{irn}^{a/b} = \frac{\sum_{p,k,l=1}^D S_{krp}^{a/b} S_{pnl}^{a/b} S_{lik}^{a/b}}{\left| T(n+1)_0^{a/b} \right|}. \quad (2.36)$$

The argument $n+1$ denotes the tensor after the $(n+1)$ th coarse graining step. So far, the only approximation is the reconnection of the lattice in terms of the S tensors in Equation (2.35). Namely, the sum can be interpreted as a matrix product, where S is a $D^2 \times D$ matrix $(S_{km,i}^a (S_{jk,i}^b)^T)$ and the factorization $M = S^a (S^b)^T$ can, in general, not be found. The renormalization scheme presented in this contexts tries to optimize the distance between the original matrix and the factorization, given by the Hilbert-Schmidt norm $\|M - S^a (S^b)^T\|^2$ [217]. One property of Hilbert-Schmidt norm is that it can be expressed in terms of the singular values of a matrix, namely

$$\|M - S^a (S^b)^T\|^2 = \sum_{i=1}^{D^2} (\sigma_i^2 - \sigma'_i)^2. \quad (2.37)$$

Here, σ_i and σ'_i denote the singular values of M and $S^a (S^b)^T$. The best approximation of Equation (2.35) with respect to the norm in Equation (2.37) is given by truncating the singular value decomposition of M , $M = U \Sigma V^T$ with $\Sigma = \text{diag}(\sigma_1, \sigma_2, \dots)$, after the D th singular value [217]. In particular, the ap-

2. Methods

proximation scheme reads

$$\begin{aligned}
M_{\alpha,\beta} &= \sum_{\gamma=1}^{D^2} U_{\alpha,\gamma} \Sigma_{\gamma} (V^T)_{\gamma,\beta} = \sum_{\gamma=1}^{D^2} U_{\alpha,\gamma} \Sigma_{\gamma} V_{\beta,\gamma} \\
&\approx \sum_{\gamma=1}^{D^2} U_{\alpha,\gamma} \Sigma'_{\gamma} V_{\beta,\gamma} = \sum_{c=1}^D S_{\alpha,c}^a S_{c,\beta}^b. \quad (2.38)
\end{aligned}$$

With $\Sigma' = \text{diag}(\sigma_1, \dots, \sigma_D, 0, \dots)$, one can directly identify $S_{k,mi}^a = \sqrt{\sigma_k} U_{mi,k}$ and $S_{l,ji}^b = \sqrt{\sigma_l} V_{ji,l}$. Iterating this procedure, the coarse grained tensor flows towards a fixed point T^* i.e., $T^*(n+1) = T^*(n)$, thus the information of the whole system is contained in T^* [217]. The discussion of the existence of a fixed point tensor is postponed to Section 2.2.2.

The rank of $T(n)$ increases exponentially with the number of coarse graining steps. Thus, one introduces a maximal tensor rank D_{\max} . So to say, one keeps at most D_{\max} singular values in the approximation scheme in Equation (2.38). The exact fixed point tensor is obtained for $D_{\max} \rightarrow \infty$. The actual implementation works as follows. Starting from an initial tensor with rank $D < D_{\max}$ the system is coarse grained and $T(n)$ truncated when it reaches D_{\max} . The iteration is continued until the convergence of the tensor is reached after n_{\max} iteration steps. Here, it suffices to monitor the behavior of the largest element $|T(n+1)_0^{a/b}|$ since the computation of the free energy only requires knowledge of this element and the full tensors $T^{a/b}(n)$ does not need to be stored. From the partition function for a system with $2N$ sites,

$$\begin{aligned}
Z &= \sum_{ijkl..} T_{ijk}^a(0) T_{jkl}^b(0) .. \\
&= (T_0^a(0) T_0^b(0))^N \sum_{ijkl..} \tilde{T}_{ijk}(0) \tilde{T}_{jkl}(0) .. \\
&= (T_0^a(0) T_0^b(0))^N (T_0^a(1) T_0^b(1))^{N/3} \sum_{ijkl..} \tilde{T}_{ijk}(1) \tilde{T}_{jkl}(1) .. \\
&= \sum_{m=0}^{n_{\max}} (T_0^a(m) T_0^b(m))^{N/3^m} \sum_{ijkl..} \tilde{T}_{ijk}(m) \tilde{T}_{jkl}(m) .. \\
&= e^{\sum_{m=0}^{n_{\max}} N/3^m \ln(T_0^a(m) T_0^b(m))} \sum_{ijkl..} \tilde{T}_{ijk}(m) \tilde{T}_{jkl}(m) .., \quad (2.39)
\end{aligned}$$

one can directly evaluate the free energy $f = -1/(2N\beta) \ln Z$. Under the assumption that the tensor is converged after n_{\max} steps, the free energy can be written in terms of the largest tensor elements like

$$\begin{aligned}
 2\beta f &= - \sum_{m=0}^{\infty} \left[\frac{\ln T_0^a(m) T_0^b(m)}{3^m} + \underbrace{1/N \ln \sum_{ijkl..} \tilde{T}^a_{ijk}(m) \tilde{T}^b_{jkl}(m)}_{\text{scales away in TDL}} \right] \\
 &= - \sum_{m=0}^{n_{\max}-1} \frac{\ln T_0^a(m) T_0^b(m)}{3^m} - \ln T_0^a(n_{\max}) T_0^b(n_{\max}) \sum_{m=n_{\max}}^{\infty} 3^{-m} \\
 &= - \sum_{m=0}^{n_{\max}-1} \frac{\ln T_0^a(m) T_0^b(m)}{3^m} - \ln T_0^a(n_{\max}) T_0^b(n_{\max}) 3^{-n_{\max}} \sum_{m=0}^{\infty} 3^{-m} \\
 &= - \sum_{m=0}^{n_{\max}-1} \frac{\ln T_0^a(m) T_0^b(m)}{3^m} - \frac{1}{2} \ln T_0^a(n_{\max}) T_0^b(n_{\max}) 3^{1-n_{\max}}.
 \end{aligned} \tag{2.40}$$

The thermodynamic quantities can be accessed as derivatives of the free energy.

2.2.2. Convergence and Performance

The previous discussion about the coarse graining procedure has certain open issues. First, one has to find a tensor network decomposition of Equation (2.33). For models with nearest-neighbor interactions this can be obtained directly since the i th leg of the T tensor represents the bond-degrees of freedom. Recent works on the triangular [217, 219], Shastry-Sutherland [220] or honeycomb lattice [144] provide explicit parametrization for the initial tensor. In general, however, it is possible to find a tensor by triangulating a general lattice, as depicted in Figure 2.6. Summing up the internal degrees of freedom in each triangle yields a function that only depends on the boundary states of the triangle. Each boundary can be represented by the leg of a tensor living in the center of the triangle. The tensor elements, in this case, represent the possible boundary states of the triangle [217].

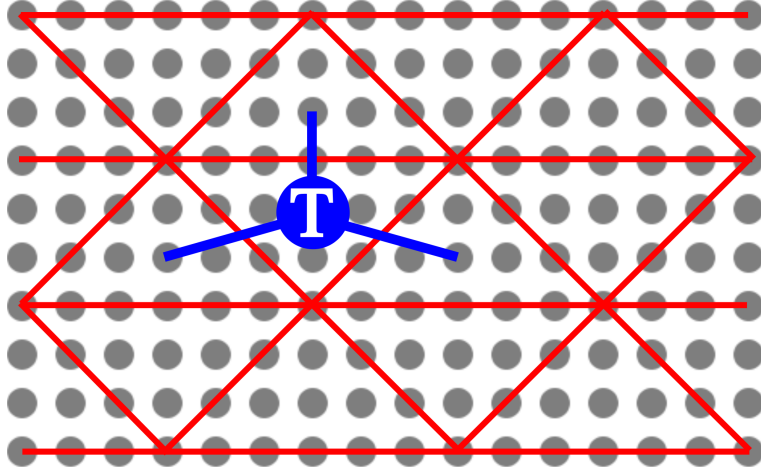


Figure 2.6.: One way of to construct the initial tensor T by using a triangulation of the lattice (red triangles) and sum over all internal degrees of freedom of each triangle. The edge degrees for freedom represent the legs of the tensor at which the contraction will take place.

A second issue is the convergence of the tensor and the error of the truncation of the singular value decomposition in Equation (2.38). By considering the tensor obtained in the triangulation (cf. Figure 2.6) as the wave function of a one-dimensional model of spins living on the edges, the coarse graining procedure resembles the evolution of the system in imaginary time – along the radial direction of the triangle – yielding the whole $(1+1)$ dimensional quantum system. In particular, the state can be chosen as $|\Psi(a, b, c)\rangle \approx \sum_{ijk=1}^D T_{ijk} |\Psi^a(i)\rangle \otimes |\Psi^b(j)\rangle \otimes |\Psi^c(k)\rangle$, where T_{ijk} is the tensor and the $\Psi^a(i)$ are the eigenstates corresponding to the i th largest eigenvalue of the density matrix of the corresponding side of the triangle. If the classical system is not critical the quantum system will be gapped and thus only weakly entangled. The eigenvalues of the density matrix will decrease exponentially in the thermodynamic limit, thus, the error of the approximation of the state $|\Psi\rangle$ will decrease like $\exp(-\text{const}(\ln D)^2)$ [217, 225].

2.3. Accessing Phase Transitions

Since the early works by Ginzburg and Landau, the concept of spontaneous symmetry breaking is intimately related to phase transitions. A local order parameter is used to distinguish the symmetry broken and the disordered state. The most famous example surely is the exactly solvable, two-dimensional Ising model [226–229]. At zero field and low temperatures, the Ising spins align parallel and the ferromagnetic state breaks spin rotation invariance – the associated order parameter is the modulus of the total magnetization, $|M|$. The inherently local nature of the order parameter distinguishes this class of phase transition from the so called “topological” phases. The latter attract a lot of interest in the last years in the context of quantum Hall systems [230] and topological insulators [231–233]. They can be characterized by topological invariants, that are intrinsically non-local objects, such as the Chern index. The discrete nature of this winding number, for instance, leads to a quantization of the Hall conductance in a two-dimensional electron gas, as predicted by Thouless, Kohmoto, Nightingale and den Nijs [230] almost twenty years ago. Even though the field of topological phases is most fascinating, the further discussion will be restricted to topologically trivial phases with local order. Furthermore, the phenomenon of deconfined criticality [234, 235] is excluded from the discussion. In this case, that goes beyond the Ginzburg-Landau paradigm for phase transitions, the transition between two ordered phases with distinct symmetries that do not contain each other can be continuous and exhibit intriguing critical properties.

2.3.1. First and Second Order Phase Transitions

A phase transition is defined as a non-analyticity in the thermodynamic potential or the ground state energy in the case of a thermal or quantum phase transition [57, 236, 237]. Quantum and thermal phase transitions can be related to each other by the famous classical-quantum mapping i.e., a d dimensional quantum system at temperature $T = 1/\beta$ can be thought of as a classical system in $d + z$ dimensions periodic in imaginary time $\tau \in [0, \beta)$ [57, 178, 179, 236]. Here, z denotes the dynamical critical exponent. Besides this similarity, the main difference is that a quantum phase transition is only defined at $T = 0$ and is driven

2. Methods

by quantum fluctuations. It can be thought of as having two competing states whose energy difference can be controlled by some parameter. The quantum phase transition is the point of an avoided crossing. A thermal phase transition, on the other hand, is driven by thermal fluctuations and occurs at finite temperatures. For ease of simplicity, the parameter driving the phase transition is called g and the transition point is at $g = g_c$. First and second order phase transitions can be classified by the behavior of the correlation length ξ . It is a measure of the length scale over which fluctuations are relevant. In the vicinity of a second order phase transition, the correlation length diverges like

$$\xi \propto |g - g_c|^{-1/\nu}. \quad (2.41)$$

The divergence of the correlation length indicates that there is no intrinsic length scale in the problem and, moreover, the system is scale invariant⁸. It was the insight of Wilson [240] that led to the powerful tool of renormalization group (RG). Most importantly, the system does not depend on its microscopic details but shows universal behavior. Its universality class can be determined by a finite set of numbers, such as the critical exponents. The self-similarity also constrains the form of the correlation functions since they have to be form invariant under a change of length scale. Of particular interest for the study of phase transitions is the behavior of

- the specific heat, $C_V \propto |t|^{-\alpha}$,
- the susceptibility, $\chi \propto |t|^{-\gamma}$,
- the order parameter, $M \propto -t^\beta$,
- the correlation length, $\xi \propto |t|^{-1/\nu}$,

in the vicinity of the critical point. The critical exponents α , β , γ and ν are not independent but related to each other by the so called scaling relations [236].

Using numerical techniques, such as quantum Monte Carlo, one is usually restricted to finite lattices with linear dimension L . This also implies that the

⁸In fact, the system is conformal invariant and the critical point can be described by a conformal field theory [238, 239].

correlation length is cut off at $\xi \sim L$ and the energy or thermodynamic potential of the system will always be smooth. In the RG picture, a finite correlation length due to a finite lattice can be thought of as being at finite distance $(g - g_c)/g_c \sim L^{-1/\nu}$ away from the critical point. In the scaling regime $x = (g - g_c)/g_c \ll 1$, physical observables can be expressed as

$$f(x, L) = L^{\kappa/\nu} G(xL^{1/\nu}), \quad (2.42)$$

where G is an analytic function and κ is a universal critical exponent associated to the observable f and ν is the critical exponent of the correlation length. The scaling behavior, although, is only asymptotic and in practice it can be difficult to reach the scaling regime with the system sizes and data resolution accessible. By expanding the universal function $G(xL^{1/\nu}, x_2L^{y_2}, \dots)$ in the not relevant fields, x_i , Beach *et al.* [241] obtain corrections to Equation (2.42) reading

$$f(t, L) = L^{\kappa/\nu} (1 + cL^{-\omega}) G(tL^{1/\nu} - dL^{-\phi/\nu}). \quad (2.43)$$

ω and ϕ are universal exponents. A detailed discussion of the extraction of critical properties from a set finite-size data is provided in Section 4.2.

As discussed in the previous chapter, a finite temperature method is employed to study quantum phase transitions that is a $T = 0$ phenomenon. There are actually two ways to intuitively understand why quantum critical behavior can be accessed even though. First, a finite-size system has a gap Δ . The closing of the gap at the critical point is controlled by the dynamical critical exponent, $\Delta \propto \xi^{-z}$. If the temperature of the system is chosen well below the gap, $T/\Delta \ll 1$, the system will remain in its ground state since thermal excitations above the gap are exponentially suppressed. Inserting the finite size cut-off shows, that the temperature has to be scaled with increasing system size like $TL^z = \text{const.} \ll 1$ i.e., $T \propto L^{-z}$. From the RG perspective, a non-zero temperature is a finite-size cut-off of the correlation length in the imaginary time direction (this correlation length is also referred to as correlation time τ). The scaling regime is recovered in the limit $x \ll T^{-z/\nu}$ and, since $x \sim L^{1/\nu}$, one recovers $T \propto L^{-z}$.

At a first-order or discontinuous phase transition the correlation length remains finite. The order parameter is discontinuous across the phase boundary and

exhibits a jump at the transition point where the ordered and disordered phases coexist and form domains. Numerically, a first-order phase transition is indicated by a pronounced discontinuity of the order parameter that gets sharper as the system size is increased. ξ does not diverge but can be very large and the first-order nature can only be observed when $L \gg \xi$. In the case of a weak first-order transition, it can in fact be very hard to distinguish the transition from a continuous one since the system will look “quasi-critical” for $L \ll \xi$ and even mimic scaling behavior for small enough system sizes. Therefore, it is essential to analyze histograms of the thermodynamic quantities, and the order parameter in particular. Phase coexistence will be indicated by a two-peak structure of the histograms in the thermodynamic limit.

2.3.2. Berezinskii-Kosterlitz-Thouless Transition

The Mermin-Wagner theorem forbids the breaking of continuous symmetries in $d < 3$ dimensions at finite temperature. Berezinskii [242] and Kosterlitz and Thouless [243] (BKT) realized that a two dimensional system with a continuous symmetry can undergo a phase transition where the behavior of its correlation functions changes. In a two dimensional XY model,

$$H^{XY} = - \sum_{\langle ij \rangle} \cos(\theta_i - \theta_j), \quad (2.44)$$

with $\theta_i \in [0, 2\pi)$, the low temperature phase is critical and has quasi-long range order i.e., all correlations decay algebraically. The total phase change across a closed path has to be an integer multiple v of 2π since θ is periodic. The continuum field theory of Equation (2.44) captures the low-energy description of a two-dimensional Bose-Hubbard model at finite temperature [244]. With respect to the following discussion, v is denoted as “vorticity”. In the low-temperature state, the vorticity is zero and the spin fluctuations along the closed path are small. The creation of a vortex, $v = 1$, costs a finite amount of energy and can not persist at low temperatures. The state of the system chosen at finite temperatures, however, is an interplay between minimizing the energy and maximizing the entropy (it minimizes $F = E - TS$). For low temperatures, vortex-antivortex pairs are bound and the net vorticity vanishes. At some temperature, the gain in

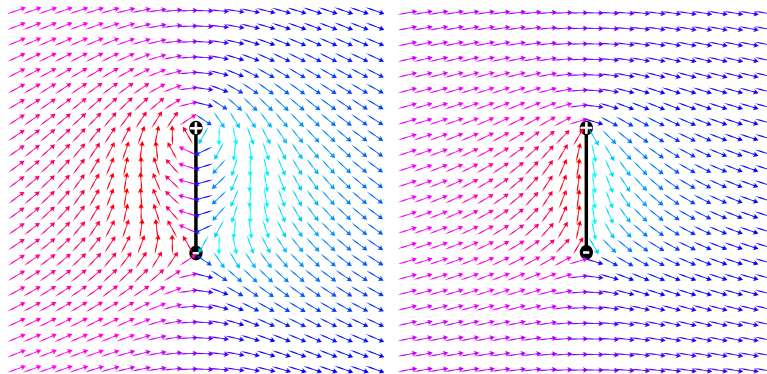


Figure 2.7.: Spin configuration for the 2D XY model with **Left:** a vortex-antivortex, **Right:** a half-vortex-antivortex pair.

entropy from separating the vortex-antivortex pair (cf. Figure 2.7) will outgrow the energy penalty and the system is in a state is given as a gas of vortices generating a finite correlation length [242, 243]. Note, that the vorticity is a non-local quantity and the concept of the BKT transition lies beyond the Ginzburg-Landau paradigm. Numerically, the defect unbinding is accessed via the universal jump of the helicity modulus

$$\Upsilon = \frac{\rho_s}{m} = \frac{T}{2v^2} \langle \mathbf{W}^2 \rangle. \quad (2.45)$$

at T_{BKT} , namely $\Upsilon = 2T_{\text{BKT}}/(v^2\pi)$. Here, ν is the elementary vorticity. Following the analysis of Weber and Minnhagen [245] and Harada and Kawashima [246], one defines $A(T) = \pi/4 \langle \mathbf{W}^2 \rangle$. Solving the BKT renormalization group equations, one obtains logarithmic finite size corrections to A at T_{BKT} reading

$$A(T; L) = A(T) \left(1 + \frac{1}{2 \log \frac{L}{L_0}} \right). \quad (2.46)$$

A precise estimate for T_{BKT} can be obtained by fitting the finite size data $A(T; L)$ for each T to Equation (2.46) getting $A(T)$ and L_0 . The transition temperature is given by $A(T_{\text{BKT}}) = v^2$ ($v = 1$ for the normal BKT transition).

In general, the elementary vorticity v does not need to be 1, as in the standard XY model on the square lattice. Since the scaling form Equation (2.46) is only valid close to T_{BKT} , one can infer the elementary vorticity from the universal

2. Methods

value of $A(T = T_{\text{BKT}})$ that can be obtained by the best fit of $A(T; L)$ to Equation (2.46) [58]. For instance, Korshunov showed that the antiferromagnetic XY model on the Kagome lattice exhibits $\nu = 1/3$ elementary vortices [247]. In Chapter 3.4, a detailed analysis of the unbinding of half-vortices due to the formation of atom pairs, as drawn in Figure 2.7, in an extended Bose-Hubbard model is given [58, 60, 248, 249].

3. Pairsuperfluidity in Dynamically Constrained Bose Systems

This chapter presents the numerical study of the ground state and thermal phase diagram for the attractive ($U < 0$) Bose-Hubbard model,

$$H = -t \sum_{\langle ij \rangle} b_i^\dagger b_j + \frac{U}{2} \sum_i n_i - \mu \sum_i n_i, \quad (3.1)$$

with a dynamical three-body constraint, $(b^\dagger)^3 = 0$, as it has been introduced in Section 1.3. Nevertheless, the main features of this model will be reviewed briefly. The three-body constraint arises dynamically as a result of a Zeno-like suppression of triply occupied sites due to strong three-body loss processes that also stabilize the system against collapse. The model in Equation (3.1) exhibits an intriguing phase diagram, shown in Figure 3.1 for the case of a two-dimensional square lattice. Recent analytical calculations [12, 45, 250, 251] and numerical works for the one-dimension case [45, 250, 251] exhibited that besides the trivially insulating phases at $n = 0$ and $n = 2$, the system stabilizes two kinds of superfluid phases. The atomic superfluid (ASF) is characterized by a finite atomic condensate with $\langle b_i \rangle \neq 0$ and a finite superfluid response ρ_s . For strong interactions $|U| \gg t$ however, a pair superfluid phase (PSF) [252] is stabilized, which is characterized by a vanishing atomic condensate and $\langle b_i \rangle = 0$, but a finite dimer condensate density with an order parameter $\langle (b_i)^2 \rangle \neq 0$. Such single-component PSF phases have been observed before in models with explicit correlated or pair hopping processes [253–255]. In the PSF phase, the $U(1)$ symmetry of the Hamiltonian is partially broken down to \mathbb{Z}_2 , and at the PSF to ASF transition, this remaining \mathbb{Z}_2 symmetry gets broken. With respect to this partial internal symmetry breaking, PSF are thus related to spin nematic

3. Pairsuperfluidity in Dynamically Constrained Bose Systems

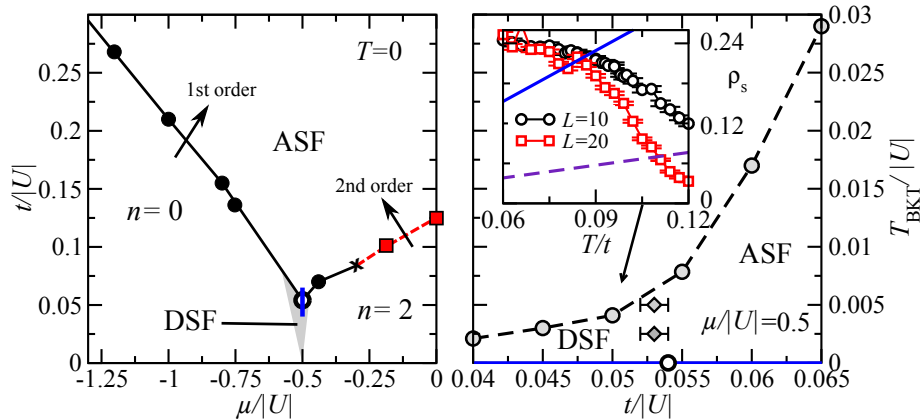


Figure 3.1.: Ground state phase diagram of the three-body constrained Bose-Hubbard model with attractive on-site interactions on the square lattice. Continuous (first-order) quantum phase transitions are shown by dashed (solid) lines. The cross indicates a tricritical point. The gray area contains the estimated PSF region. Right panel: Finite temperature phase diagram along $\mu/|U| = -0.5$. The inset shows the temperature dependence of the superfluid density ρ_s at $t/|U| = 0.05$ (PSF) for $L = 10$ and 20 along with lines for normal $2T/\pi$ (dashed line) and anomalous $8T/\pi$ (solid line) universal stiffness jumps.

states [256]. Within Ginzburg-Landau theory, a Feshbach resonance term couples the ASF and PSF order parameter fields, which implies an effective $U(1) \times \mathbb{Z}_2$ symmetry similar as in the boson Feshbach resonance problem [12, 54, 250, 257]. From such analysis, the ASF-PSF transition was found to be Ising-like at unit filling, $n = 1$, and driven first-order by fluctuations via the Coleman-Weinberg mechanism [258] for $n \neq 1$ [250, 251].

The two-dimensional model on the square lattice, with linear extend L and $N = L^2$ sites, is accessed using a directed loop algorithm, as described in Section 2.1.1. Periodic boundary conditions are employed in both lattice directions. The superfluid phases are identified by the superfluid density $\rho_s = T\langle \mathbf{W}^2 \rangle / (2t)$, measured via the winding number fluctuations $\mathbf{W} = (W_x, W_y)$ (see also Section 2.1.2), and atomic and pair condensates $\langle b \rangle$ and $\langle b^2 \rangle$. Using two kinds of directed loops, in which the worm heads carry either a single creation (annihilation) operator b^\dagger (b) or a pair operator $(b^\dagger)^2$ [(b^2)], provides direct access to the equal-time Green's function, see Equation (2.24) in Section 2.1.2, that can be accessed in the off-diagonal update. Single and pair worms are inserted with an equal prob-

ability during the off-diagonal update. The atomic and pair condensate densities can then be accessed as

$$C_1 = \frac{1}{N^2} \sum_{ij} \langle G_1(i, j) \rangle \quad (3.2)$$

$$C_2 = \frac{1}{N^2} \sum_{ij} \langle G_2(i, j) \rangle. \quad (3.3)$$

The Mermin-Wagner theorem [59] excludes the existence of off-diagonal long-range order finite temperatures since the condensate breaks a continuous $U(1)$ symmetry. Thus, the data has to be extrapolated to the thermodynamic limit, $L \rightarrow \infty$, and $T \rightarrow 0$, as will be detailed in the following.

3.1. Effective Feshbach Model

Before presenting quantum Monte Carlo results studying the phase diagram of the aforementioned model, the general features and its effective description will be discussed. Following an elaborate field theoretic analysis of Equation (3.1) [250, 251, 259], an effective description in terms of Feshbach models, as introduced by Romans *et al.* [53] and Radzihovsky[54, 257] is obtained. The local Hilbert space, containing of the particle number state $|\alpha\rangle$, $\alpha = 0, 1, 2$ is extended to a new vacuum state $|\text{vac}\rangle$. The bosonic states are generated from the vacuum by three operators $t_{i\alpha}$,

$$|\alpha\rangle = \frac{1}{\sqrt{\alpha!}} t_{i\alpha}^\dagger |\text{vac}\rangle, \quad (3.4)$$

obeying the holomorphic hardcore constraint $\sum_\alpha t_{i\alpha}^\dagger t_{i\alpha} = 1$. Defining $X_i = 1 - n_{i1} - n_{i2}$ ($n_{i\alpha} = t_{i\alpha}^\dagger t_{i\alpha}$), the kinetic Hamiltonian reads

$$H^t = -t \sum_{\langle ij \rangle} \left(\underbrace{t_{1i}^\dagger X_i X_j t_{1j}}_{\text{I}} + \underbrace{2t_{2i}^\dagger t_{2j} t_{1j}^\dagger t_{1i}}_{\text{II}} + \underbrace{\sqrt{2}(t_{2i}^\dagger t_{1i} X_j t_{1j} + t_{1i}^\dagger X_i t_{1j}^\dagger t_{2j})}_{\text{III}} \right). \quad (3.5)$$

Part I and II describe to movement of atoms and pairs; part III is a bi-local Feshbach term where two atoms are transformed into a paired (molecule) state.

3. Pairsuperfluidity in Dynamically Constrained Bose Systems

The continuous Feshbach model [53, 54, 257], describing the low energy sector of Equation (3.1), has two order parameter fields associated to the condensation of atoms (Ψ_1) and pairs (Ψ_2). Due to global particle number conservation, $|\Psi_1|^2 + 2|\Psi_2|^2 = \text{const.}$, the symmetry is $U(1) \times \mathbb{Z}_2$. In the presence of a Feshbach coupling, three states are found to exist, namely an uncondensed state with $\langle \Psi_1 \rangle = \langle \Psi_2 \rangle = 0$, an atomic superfluid (ASF) having $\langle \Psi_1 \rangle \neq 0$ and $\langle \Psi_2 \rangle = 0$ and a pair superfluid (PSF) with $\langle \Psi_1 \rangle = 0$ and $\langle \Psi_2 \rangle \neq 0$. A pure pair condensate, however, is not stable due to the Feshbach coupling $\sim \alpha \Re[\Psi_2^\dagger \Psi_1^2]$ [257]. The transition from the PSF with broken $U(1)$ symmetry to the ASF breaks the remaining \mathbb{Z}_2 symmetry. From there, one can naively infer, that the transition is in the 3D Ising universality class. However, it turns out, that fluctuations from the Goldstone mode, associated with the $U(1)$ symmetry breaking of the PSF, coupling to the Ising field can drive the transition first-order [53, 257, 259–262] by the Coleman-Weinberg mechanism [258]. The Ising nature of the one-dimensional ASF-PSF transition has been studied in detail using DMRG [263, 264] but no evidence of a first-order behavior is reported. Returning to the microscopic model in Equation (3.1), it turns out, that the ASF-PSF transition is weakly first-order everywhere but at $n = 1$ where the system exhibits a 3D Ising transition. The correlation length is found to diverge, in the vicinity of the critical filling, as $(n - 1)^{-6}$ [259]. It is noteworthy that the existence of a continuous supersolid in the strong coupling regime is argued in Ref. [251]. The existence of this phase relies on the enhancement of the $U(1)$ symmetry to $SO(3)$ giving rise to the coexistence of diagonal and off-diagonal long range order at $n = 1$.¹ This symmetry, however, does only persist in second order perturbation theory but is broken explicitly by higher order terms [259].

The mechanism of the ASF-PSF transition is closely related to the nematic phase [256] found in spin-1 systems where spin rotational symmetry is partially broken but time reversal symmetry is preserved i.e., there is not magnetic (quasi) order. In one dimension, the PSF phase corresponds to the $XY2$ phase found for

¹The effective model in the regime of tightly bound pairs is an effective antiferromagnetic Heisenberg model [251, 259]. The easy-plane anisotropy, favoring longitudinal ordering/superfluidity, vanishes in second order perturbation theory but is restored in higher order [259]. Even though the $U(1)$ easy-plane symmetry would be enhanced to the full $SO(3)$ symmetry, it is still questionable whether this isotropic case should be regarded a supersolid. Nevertheless, no evidence is found for diagonal ordering in the PSF regime.

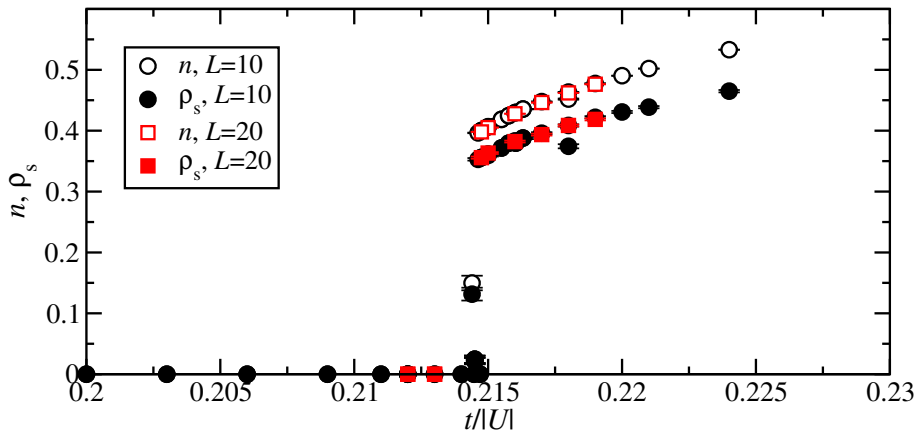


Figure 3.2.: Filling n and superfluid density ρ_s at the first-order ASF-insulator transition at $\mu/|U| = 1$ for $TL = 0.08|U|$.

spin-1 chains with single-ion anisotropies [265, 266] or the spin-quadrupolar phase in the spin-1 chain with bi-linear and bi-quadratic coupling terms that gives rise to a rich phase diagram characterized by a nematic ordering tensor [267, 268]. A similar model with a local three-body constraint can also be realized using rubidium spinor condensates [255].

3.2. ASF-Insulator Transition

First, the quantum phase transitions between the ASF and the (trivially) insulating phases at $n = 0$ and $n = 2$ is addressed. While SF to insulator transitions are often continuous, they can be driven first-order for attractive interactions [12, 54, 262]. In fact, the transition from the empty system ($n = 0$) to the ASF is indeed first-order over an extended parameter regime. This is evident from robust discontinuities in both the filling n and superfluid density ρ_s , such as those shown in the left panel of Figure 3.2 at $\mu/|U| = -1$. From an effective potential approach, Lee and Yang propose a scenario including a tricritical point separating the line of first-order ASF-insulator transition from a line of continuous dilute bose-gas transitions [12]. In fact, the transition is predicted to turn continuous beyond a tricritical point near $\mu/|U| \approx -0.9$. However, no evidence for a continuous transition at least down to $\mu/|U| = -2$ is found in the presented simulations. This indicates stronger effects of the Feshbach reso-

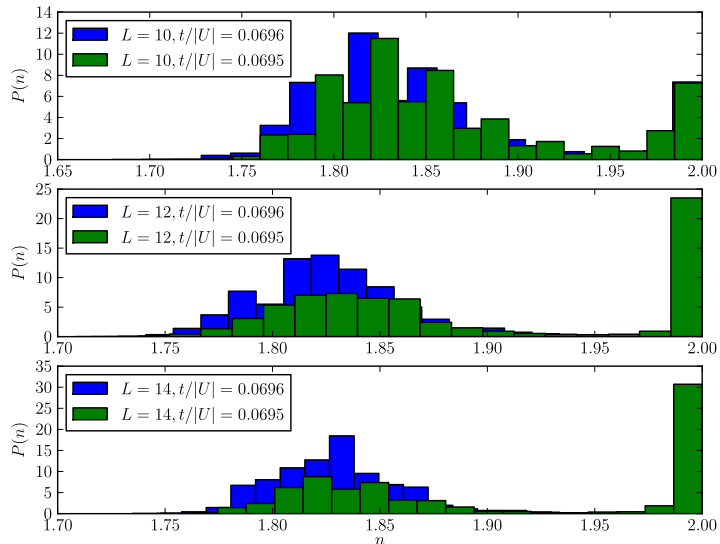


Figure 3.3.: Histogram of the filling n for different system sizes L at $\mu/|U| = -0.42$. The appearance of a clear two-peak structure indicates a discontinuous ASF-insulator transition at $t/|U| \approx 0.0696$.

nance coupling for $\mu/|U| < -0.5$, than anticipated in Ref. [12]. On the other hand, the proposed scenario is found to be realized for the transition from the ASF to the full system ($n = 2$), which is continuous beyond $\mu/|U| \approx -0.3$, cf. Figure 3.1. A discontinuity in the filling n and the superfluid density $\mu/|U|$ are found for $\mu/|U| \leq -0.43$ (not shown). In the vicinity of the transition, a robust two-peak structure is obtained, see Figure 3.3 for the density histograms at $\mu/|U| = -0.42$, that is a clear indication for a first-order phase transition. As shown in Figure 3.4, no discontinuity in n or ρ_s is encountered at $\mu/|U| = 0$. To assess if this transition corresponds to that of a dilute bose gas of holes [57], we analyze the behavior close to the transition point in more detail. In that case and for two dimensions, the density ($2 - n$) of the holes should exhibit a linear increase $(2 - n) = a(\tau - \tau_c) \ln(b/(\tau - \tau_c))$ with a logarithmic correction [269] in the vicinity of the transition point at $\tau_c = 0.125$, while $\rho_s = (2 - n)$ in the dilute limit [270]. Note, that $\tau = t/|U|$. As seen from Figure 3.4, both observables fit well to these functional forms and; the dynamical critical exponent equals $z = 2$ at this transition [57], while our QMC temperature scales are sufficiently low to sample the finite system's ground state. Thus, the insulator-ASF phase

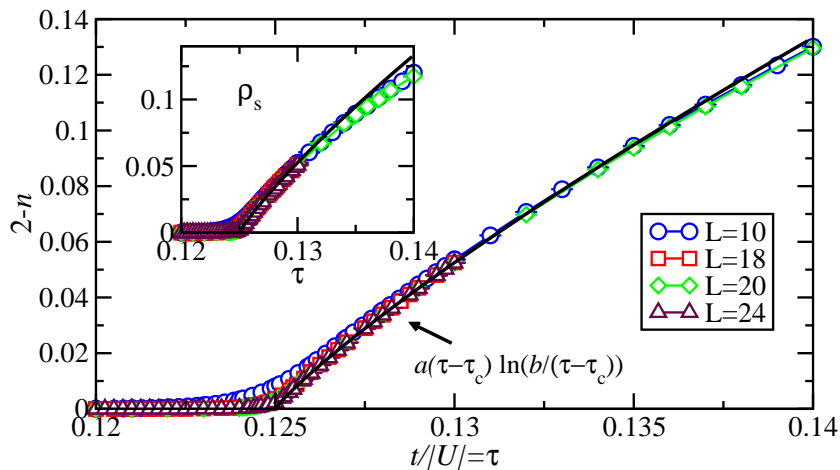


Figure 3.4.: Hole density $(2-n)$ at $\mu = 0$ and $T/|U| = 0.08/L$ for various system sizes fitted to $(2-n) = a(\tau - \tau_c) \ln(b/(\tau - \tau_c))$ for the dilute Bose gas transition at $\tau_c = 0.125$. The inset shows the superfluid density that obeys the same functional behavior, $\rho_s = n$, near the transition.

boundary is in good agreement with the effective potential approach [12].

3.3. Accessing the Superfluid Phases

Fixing $\mu/|U| = -0.5$, the ASF and PSF phase is accessed by varying the hopping amplitude $t/|U|$. In order to establish ODLRO in the atomic and pair channel, the temperature has to be chosen low enough to access the ground-state properties of the system. In particular, the temperature has to be well below the Berezinskii-Kosterlitz-Thouless transition. One can see from the finite-temperature phase diagram in the right panel of Figure 3.1, that will be discussed in detail in Section 3.4, that T_{BKT} reduced in the PSF since the energy scales for the hopping processes is not t but $t^2/|U|$. In particular, close to the ASF-PSF transition it is found to be $T_{\text{BKT}}/t \approx 0.1$ and the system size dependent temperature is fixed to $TL = 0.01|U|$ (for a dynamical critical exponent $z = 1$) in order to extrapolate to the $T = 0$ phase in the thermodynamic limit.

3.3.1. ASF-PSF Transition

First, the ASF-PSF transition is accessed. For $\mu/|U| = -0.5$, the filling is always slightly greater than unity for finite $t/|U|$, thus, a discontinuity in C_1 is

3. Pairsuperfluidity in Dynamically Constrained Bose Systems

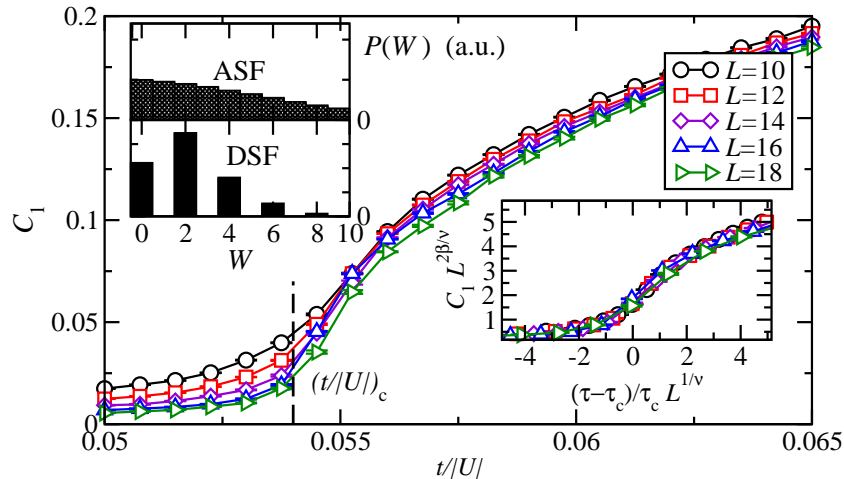


Figure 3.5.: QMC data for C_1 obtained for different system sizes along $\mu/|U| = -0.5$ for $T/|U| = 0.01/L$. The critical coupling $(t/|U|)_c \approx 0.054$ is denoted by a vertical bold line. Right inset: data collapse based on three-dimensional Ising critical exponents. Left inset: Histogram $P(W)$ of the winding number W taken in the ASF ($t/|U| = 0.06$) and PSF ($t/|U| = 0.045$) region at $T/|U| = 0.001$ ($L = 14$).

expected [251, 259]. However, the ASF-PSF transition is weakly first-order with a diverging correlation length $\xi \sim (1-n)^{-6}$ in the vicinity of the Ising critical point at $n = 1$ [259]. The order parameter C_1 across the ASF-PSF transition, shown in Figure 3.5, exhibits scaling in the vicinity of the transition point $\tau_c = (t/|U|)_c$ i.e.,

$$C_1 = L^{-2\beta/\nu} g(L^{1/\nu}(\tau - \tau_c)/\tau_c). \quad (3.6)$$

A scaling plot, using 3D Ising critical exponents $\beta = 0.3264(4)$ and $\nu = 0.6298(5)$ [271], is found in the right inset of Figure 3.5, yielding a critical hopping of $(t/|U|)_c = 0.054(1)$. Unfortunately, from the system sizes available, the true nature of this transition can not be discerned. In fact, large correlation length, $\xi \gg L$, would mimic a quasi-critical behavior that is controlled by proximity of the Ising critical point. Also, the order parameter histograms in the vicinity of the critical point give no evidence of phase coexistence. Given the above estimate of $(t/|U|)_c$, the mean-field value $(t/|U|)_c \approx 0.044$ [45] is found to underestimate the stability of the PSF phase by about 20%. Improvements over the mean-field solution by accounting for quantum fluctuations show similar deviations [251].

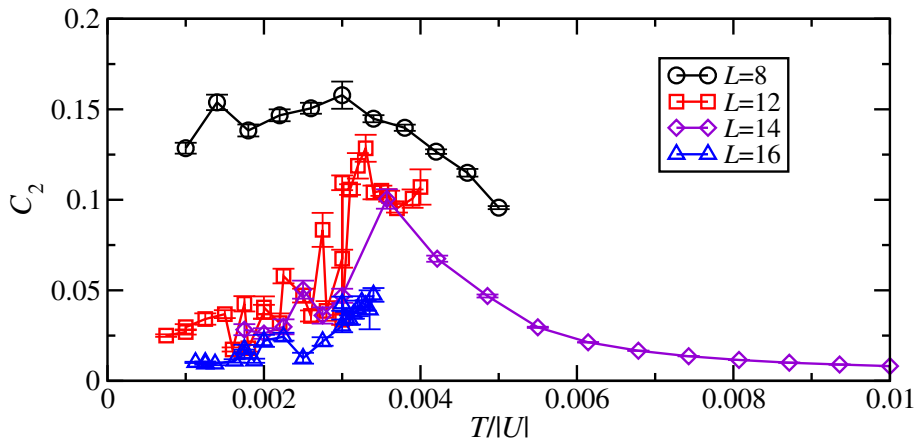


Figure 3.6.: Pair condensate fraction C_2 for different system sizes L as a function of temperature $T/|U|$ obtained at $t/|U| = 0.045$ and $\mu/|U| = -0.5$. With the onset of a fat-tailed distribution at $t/|U| \approx 0.004$, that is close to T_{BKT} , the condensate fraction decreases rapidly as the temperature is lowered.

Basically, one should try to access the ASF-PSF transition for different values of $\mu/|U|$ and, in particular, for the case $n = 1$ by projecting the measurements to the subspace of unit filling. Further insight into this transition can also be obtained from larger system sizes. It turns out, however, that the worm update shows a peculiar behavior in the vicinity of the PSF that makes simulations at $\mu/|U| \neq -0.5$ and in the PSF phase unfeasible. In order to understand the algorithmic behavior, look at the temperature dependence of the pair condensate C_2 (Figure 3.6) for $\mu/|U| = -0.5$ and $t/|U| = 0.045$ i.e., well inside the PSF. For large temperatures, where the system is in the disordered phase, C_2 tends to grow as the temperature is decreased. This finite-size behavior is expected since the power-law decay of the Green's function is related to the superfluid density. At low temperatures, however, C_2 breaks down and the obtained data points show large fluctuations. This behavior is related to a fat-tailed distribution of the estimator for C_2 . Before going into the details of the actual distribution of C_2 , one has to recall how the mean and error are obtained in Monte Carlo. Namely, the Markov process generates a series of measurements, $\{C_2^i\}$ distributed by some function $P(C_2)$. If P is normalizable and the first and second moment i.e., mean and variance, are well defined, the binning analysis of the timeseries $\{C_2^i\}$ will converge towards a Gaussian distributional with the true mean and

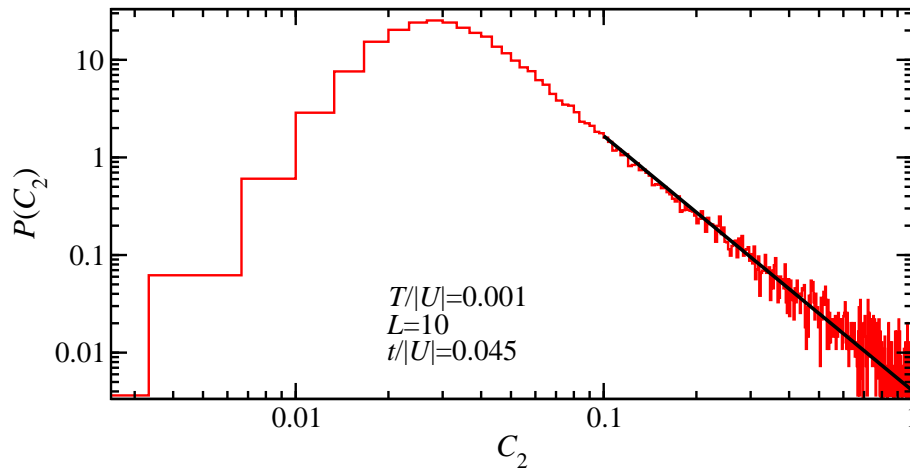


Figure 3.7.: Histogram of the pair condensate C_2 for $t/|U| = 0.045$ and $T/|U| = 0.001$. The black line is a power law fit.

variance [56]. The distribution of C_2 in the PSF, however, has a fat tail, namely, shows extremely large kurtosis and its asymptotic behavior is given by a power-law i.e., $P(x) \propto x^{-\alpha}$ for large x . For $\alpha < 3$, the variance of P diverges and the central limit theorem does not hold. A generalized central limit theorem, nevertheless, states that in this case the distribution will weakly converge towards a stable distribution [56] that will not be Gaussian. Figure 3.7 shows $P(C_2)$ deep inside the PSF regime. One can clearly identify the asymptotic power-law behavior with $\alpha \approx 2.2$ and, in fact, it can be fitted to a Fréchet distribution. The unexpected behavior of C_2 as a function of temperature can now be explained in this context. The fat tail indicates that rare events of extremely large values of C_2 are the main contribution to the mean value. The algorithm fails to sample the rare events correctly thus the mean value of this distribution is underestimated. Considering the example shown in Figure 3.7, that is for a very small system with $L = 10$, the mean value from the (invalid) Monte Carlo sampling yields $C_2 \approx 0.1$. Fitting the tail of the distribution and taking the tail into account analytically, however, yields $C_2^{\text{fat}} \approx 0.13$. The missing of the rare events in the sampling procedure, that can be thought of as an effective cut-off of $P(C_2)$, is the reason why the binning analysis seems to converge and gives an error estimate even though the variance is ill defined. The divergence of the variance also implies, that this sampling procedure can not be used to get a physical estimate of the condensate density. Moreover, the distribution of C_2 has also drastic

consequences on the performance of the algorithm. C_2 is measured during the worm update and basically counts how often the worm head crosses its initial level thus, rare events of C_2 signify long worms. This is observed indeed, that extremely long pair worms appear that do not close and make simulations away from $\mu/|U| = -0.5$, where the problem seems to be less severe, infeasible, as adumbrated beforehand. It is common practice that the problem of extremely long worms is circumvented by introducing a cut-off for the worm length i.e., if the worm exceeds a certain length (much larger than Λ such that the worm can actually wind around the imaginary time direction) it will be terminated and its change undone [184]. This procedure, however, is not well controlled but usually the rejection probability is very small, since the weights of “rare events“ in conventional Monte Carlo is greatly suppressed, such that the error can be neglected. In the fat tailed case, on the other hand, those events are relevant and must not be cut-off. Thus, this method is infeasible and will not be pursued.

3.3.2. On an Efficient Monte Carlo Update for the Pair Phase

The appearance of sampling problems in the pair phase can be understood by considering the construction of pair worms. Since no explicit pair hopping is present in the Hamiltonian but the PSF is dominated by pair processes, also reflected in the even-odd effect in the winding numbers shown in the left inset of Figure 3.5, the pair worm can only perform an off-diagonal move if it encounters a bond shared by a singly occupied site. Singly occupied sites are greatly suppressed in the PSF. Motivated by the lack of pair processes, the Hamiltonian in Equation (3.1) will be extended to include these processes explicitly. The easiest way is to include nearest-neighbor pair processes

$$H_1 = H - t' \sum_{\langle ij \rangle} (b_i^\dagger)^2 (b_j)^2. \quad (3.7)$$

Physically, this term also appears in a setup realizing a Bose-Hubbard model with three-body hardcore constraint using rubidium spinor condensates [255].

3. Pairsuperfluidity in Dynamically Constrained Bose Systems

Another approach is to include long-range hopping between all sites,

$$H_2 = H - \frac{h}{N} \sum_{ij} \left[(b_i^\dagger)^2 (b_i)^2 \right] + \frac{K}{N} \sum_{ij} \mathbb{1}. \quad (3.8)$$

The factor $1/N$ ensures that the energy is extensive. This approach resembles a linear coupling scheme since the long-range hopping term is just the pair condensate C_2 . Furthermore, the second approach also leads to an additional estimator for C_2 since the pair condensate density can be expressed in terms of kinetic energies, namely

$$C_2 = -\frac{1}{Nh} \langle H_h \rangle + \frac{1}{N^2 t^2} \langle H_t(b) H_t(b) \rangle. \quad (3.9)$$

Here, $\langle H_h \rangle$ denotes the average kinetic energy of the long-range vertices and $\langle H_t(b) H_t(b) \rangle = 1/\beta^2 n_{tt} (n-1)$ is the bond short-range kinetic energy correlation (c.f. Equation (2.16)). n_{tt} is the occurrence of two consecutive kinetic energy t -terms on bond b .

The actual implementation of Equation (3.8) requires some modifications to the diagonal update scheme presented in Section 2.1.1, based on the update scheme for arbitrary long-range interactions presented by Sandvik [174]. Firstly, a diagonal update is performed inserting or removing only short-range vertices with probabilities given in Equation (2.11) and Equation (2.12). In order to perform long-range off-diagonal updates in the worm update, one has to insert long-range dummy operators given by the last expression in Equation (3.8). The insertion probabilities can be obtained using Heat-Bath i.e., $P_{\mathbb{1} \rightarrow H_K}^{\text{lr}} = \sum_{\text{bonds } b} W_b / (\Lambda - n + \beta \sum_{\text{bonds } b} W_b)$, where Λ denotes the length of the operator string and n does not denote the filling but the total number of non-unity operators. Since the weights W_b of all diagonal long-range operators are identical and $\sum_{\text{bonds } b} W_b = N_{\text{bonds}} K/N$, one can directly write down the insertion and remove probabilities

$$P_{\mathbb{1} \rightarrow H_K}^{\text{lr}} = \frac{\beta N_{\text{bonds}} K/N}{\Lambda - n + \beta N_{\text{bonds}} K/N} \quad (3.10)$$

$$P_{H_K \rightarrow \mathbb{1}}^{\text{lr}} = \frac{\Lambda - n + 1}{\Lambda - n + 1 + \beta N_{\text{bonds}} K/N}. \quad (3.11)$$

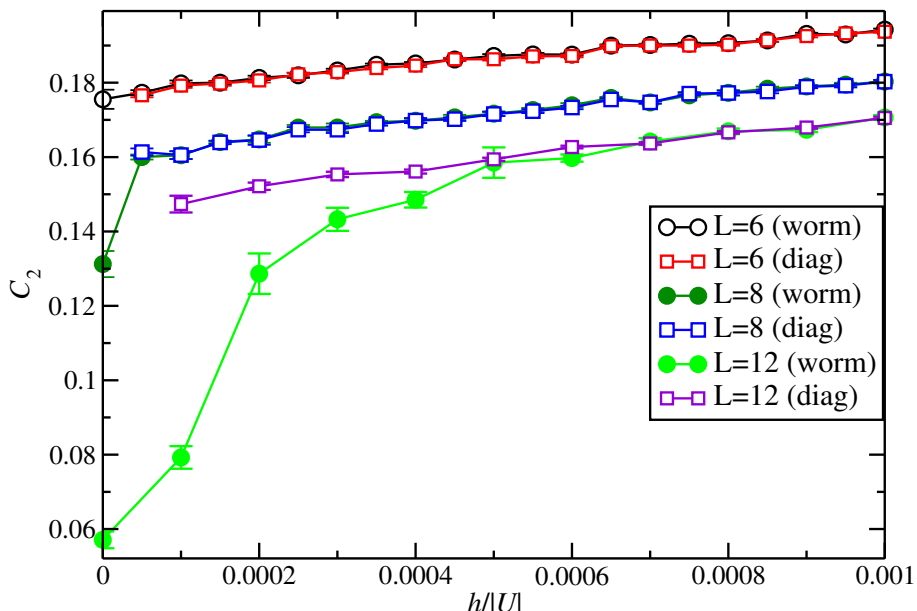


Figure 3.8.: Condensate density C_2 as a function of field h for different system sizes obtained with the kinetic-energy estimator (diag) and from the worm update (worm) for $TL = 0.01|U|$.

If an insertion move is accepted a diagonal long-range operator is inserted at a random bond chosen from a uniform distribution. Furthermore, it is found that adjusting the weight of the long-range diagonal vertices using $K = h$ yields a good performance for this algorithm.

Figure 3.8 shows the pair condensate C_2 obtained with the two estimators as a function of $h/|U|$. For small systems or large values of $h/|U|$ both estimators agree and it is found that the distribution $P(C_2)$ behaves well such that the variance is well defined. At $L = 12$, however, one can clearly see, that, for $h/|U| = 0.005 (= t/9)$, the measurement of C_2 during the worm update is suppressed whereas the kinetic energy estimator remains stable. The limit of zero pair hopping is reached by extrapolating $C_2(h, t')$ to $h \rightarrow 0$ or $t' \rightarrow 0$, respectively. Figure 3.9 illustrates, that one is in a linear regime for small enough values of the pair coupling, thus, C_2 is extrapolated by a linear fit from the pair-hopping data and the error bars are estimated by a Bootstrap analysis [191]. The extrapolated results for the condensates in the ASF and PSF regime is found in Figure 3.10. For $t/|U| = 0.1$ one is well within the ASF phase and the expectation values of both C_1 and C_2 are finite. For $t/|U| = 0.045$ and 0.05 , however, the atomic condensate, that is obtained without extrapolation since its distribution resembles

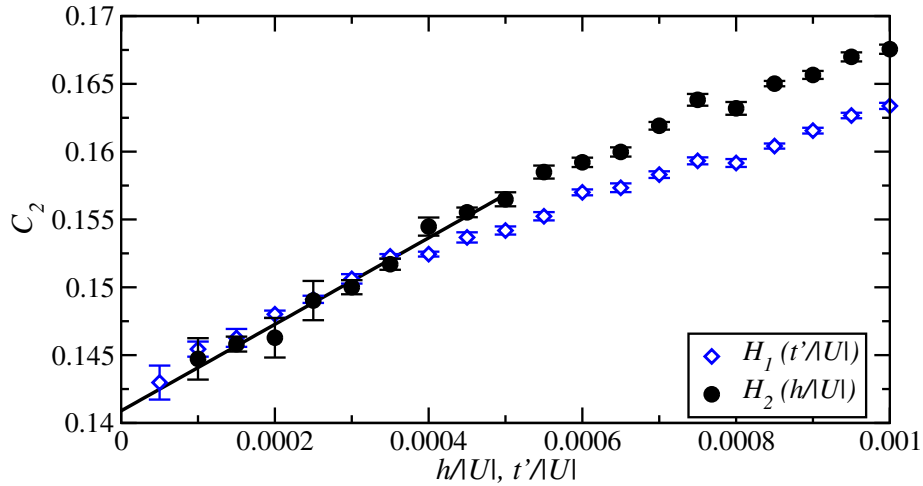


Figure 3.9.: Extrapolation of the condensate fraction C_2 to $h, t' \rightarrow 0$ at $t/|U| = 0.045$, $L = 14$, $\mu/|U| = -0.5$ and $TL = 0.01|U|$.

a Gaussian, vanishes but the system exhibits true long range order solely in the pair channel.

3.4. The Thermal Half-Vortex Unbinding Transition

The pairing mechanism that leads to the suppression of an atomic condensate C_1 at $T = 0$ is also reflected in the finite temperature behavior. Exploring the finite temperature phase diagram, see right panel in Figure 3.1, one finds an even-odd effect in the winding numbers when crossing from the ASF to the PSF. Whereas the ASF can have even or odd winding numbers, the PSF phase is confined to even parity sectors. Figure 3.5 shows histograms of the modulus of the winding number on both sides of the ASF-PSF phase transition. The winding numbers count the number of particles crossing the periodic boundary conditions and a purely even winding number indicates that the superflow through the system is solely composed out of boson pairs. The paired nature of the PSF leads to the proliferation of half-vortices [58, 247] (see also Figure 2.7 for a comparison of a vortex and halfvortex excitations in the XY model) resulting in an unconventional jump of the helicity modulus at the BKT transition that has also been predicted in the context of Feshbach models by Romans *et al.* [53]. Namely, the elementary vorticity is $\nu = 1/2$ and the helicity jump is increased by a factor of $1/\nu^2 = 4$, as shown in Section 2.3.2. The factor of four can also be understood by a simple

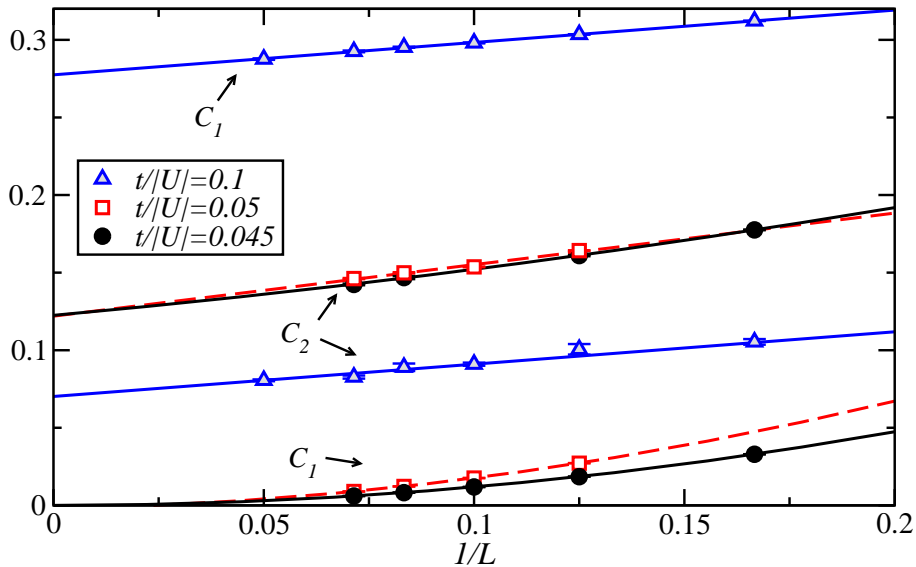


Figure 3.10.: Finite size scaling analysis of the extrapolated condensate densities C_1 and C_2 in the ASF and PSF regime for $\mu/|U| = -0.5$ obtained for $TL = 0.01|U|$.

consideration. In the paired phase, singly occupied sites can be neglected and the superflow is generated via second order hopping processes. Thus, Equation (3.1) can be rewritten as

$$H = -t'' \sum_{ij} \left(d_i^\dagger d_j + \text{h.c.} \right), \quad (3.12)$$

where $t'' \sim t^2/|U|$ and $d_i = (b_i)^2$. Equation (3.12) describes a gas of free hard-core "pair"-bosons. The winding numbers of the "pair" particles, however, is increased by a factor of 2 due to the compound nature – $\langle W_{\text{pairs}}^2 \rangle \rightarrow 4\langle W^2 \rangle$. The inset in the right panel of Figure 3.1 shows the superfluid density across the BKT transition in the PSF phase and the straight lines denote the universal jump for vortices and half-vortices. It becomes clear, that the BKT transition is not governed by the formation of normal vortices. Note, that the BKT temperature is highly suppressed in the PSF regime and simulations facing the algorithmic problems on the one and the low temperature scales on the other side are very challenging.

Ng and Yang, exploring the finite temperature phase diagram of this model as well [60], consider a slightly different route using a multi-worm update, as

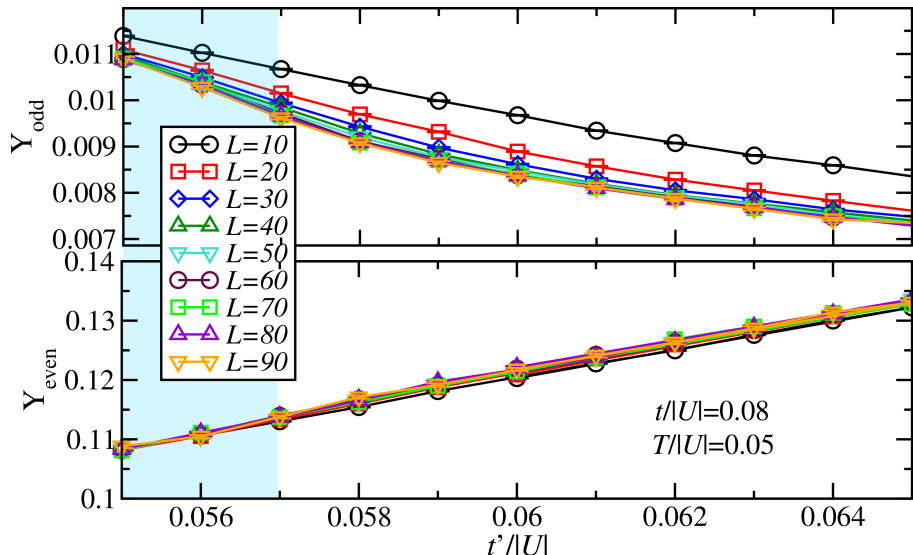


Figure 3.11.: Υ_{even} and Υ_{odd} for $\mu/|U| = -0.5$, $t/|U| = 0.08$ and $T/|U| = 0.05$. The blue shaded area denotes the parameter regime where the system exhibits quasi long-range order in the atomic channel.

discussed in Section 3.5. First, they increase the energy scales (and thus the temperature scale for the BKT transition) by adding a nearest-neighbor repulsion term. Also analyzing the unconventional helicity jump, they focus on the discrimination of the finite temperature superfluid phases. Since they do not access the of the Green's function (the implementation of the Green's function in the multi-worm algorithm is not as straight forward as in the pairworm formulation used in this work), they characterize the phases via the even-odd effect of the winding numbers. In particular, two "superfluid densities", ρ_{even} and ρ_{odd} , are defined that only involve the corresponding winding number sectors. This approach, although it seems to give reasonable results in this case, has to be handled with care. ρ_{even} and ρ_{odd} do not have a physical interpretation as a response function, unlike the superfluid density ρ_s ($\neq \rho_{\text{even}} + \rho_{\text{odd}}$), or an order parameter since the phase shifts affects both the atomic and paired component (see also Appendix B). The partitioning of the winding numbers has led to false physical conclusions in different contexts as detailed in the comment [272] by Eckholt and Roscilde on the recent Letter about the proliferation of a Feshbach condensate [273]. In addition to that, it is not clear whether the onset of ρ_{odd} is accompanied by the onset of quasi long-range order of the atomic Green's function.

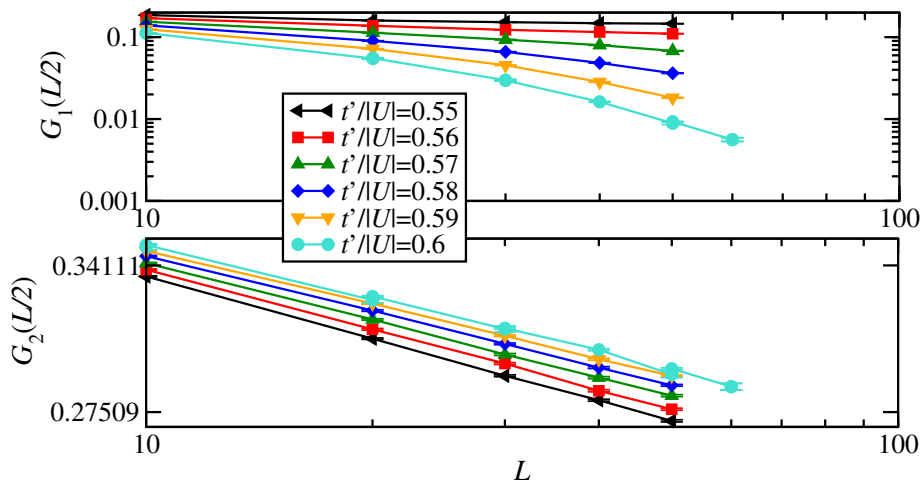


Figure 3.12.: Atomic and pair Green's function $G_1(L/2)$ and $G_2(L/2)$ for different system sizes evaluated at $x = L/2$. The quasi long-range order in the atomic channel vanishes at $t'/|U| \approx 0.57$. The data is obtained for $\mu/|U| = -0.5$, $t/|U| = 0.08$ and $T/|U| = 0.05$.

To clarify this situations, the $t - t'$ model, as introduced in Equation (3.7), is revisited. Fixing $\mu/|U| = -0.5$ and $t/|U| = 0.08$ – well in the ASF regime – the ASF-PSF transition is driven by gradually increasing $t'/|U|$. Figure 3.11 and Figure 3.12 show the helicities Υ_{even} and Υ_{odd} and the real-space resolved Green's functions. Performing this analysis for a large temperature range, it is found that in this case the loss of quasi long-range order in the atomic channel is no accompanied by a confinement of the system to an odd winding sector. This proves that the partitioning of the superfluid density is not suitable to distinguish the ASF and PSF in the generic case and one has to return to the measurement of the real-space resolved Green's function on the cost of a loss of performance, though.

3.5. Perspectives towards a Parallel Multi-Worm Algorithm

Tackling the physics of multi-component systems [84, 262, 274–277] or Hamiltonians with correlated and pairing hopping terms using QMC [60, 253, 273, 278, 279] is challenging since one has to update multiple dynamical and competing degrees of freedom. Multi-component worm updates have been introduced resembling

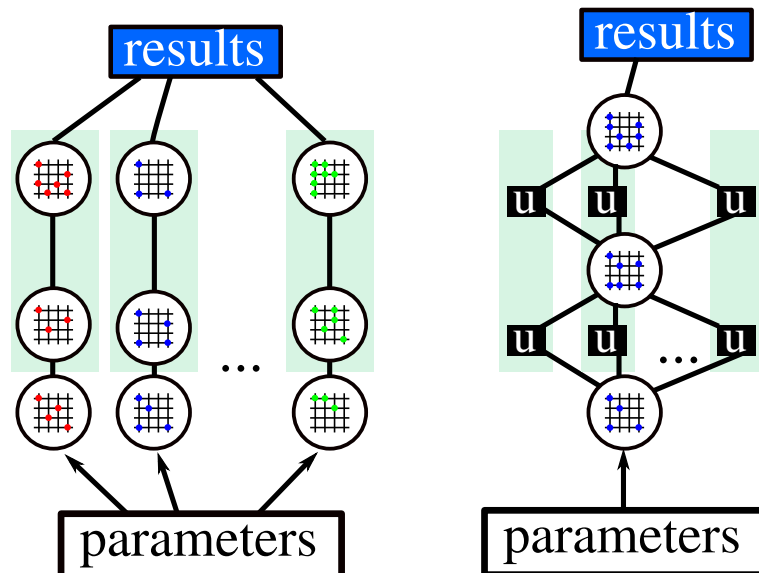


Figure 3.13.: Left: One task is executed serially on certain computation nodes (green bars) and the results are collected in the end. This method is also referred to as "farming". Right: The updates on one system are executed in parallel and the system is synchronized after each update step.

the hopping processes of each species [84] and proven to be very efficient in this context.

An application of a multi-worm update scheme on the problem presented in this chapter was presented recently [60, 279]. Instead of using a worm carrying a pair creation or annihilation or creation operator, Ng and Yang [60] use an update scheme where two worms, each carrying just a single boson operator, spawn at the same point in the operator string. The main difference to the pair worm update is that the two worms can branch i.e., travel as two independent worms and merge eventually. It seems that this implementation does not suffer from diverging loop lengths since the problem that no explicit dimer hopping term is present and off-diagonal moves are suppressed, is diminished by the possibility to branch. However, this approach does not allow for a straight-forward measurement of the pair Green's function and, notably, the condensate has not been addressed in their approach [60, 279].

Nonetheless, this approach yields potential to improve not only problems involving pair processes but also the directed loop scheme in general. One of the main problems of QMC, and the world line methods in particular, is that it

does not show hard scaling and parallelization is usually implemented trivially as multiple replicas of each parameter set are farmed across a parallel computer platform. That is to say, each processor performs serial updates on one particular system. Performing measurements on multiple independent replicas can be done very effectively using farming since the samples from each realization of the system will be independent. However, the accessible system sizes and temperatures are limited by the serial performance on one computer core. For instance, each core has to thermalize the system separately. Of course, the system can be thermalized on one computing node and afterwards be distributed to a parallel environment where each process performs independent updates and measurements on the thermalized system. This ansatz, on the other hand, introduces correlations between the measurements on each core. Since, in general, the number of measurement should be much larger than the thermalization steps to be effective, one can argue, that the thermalization time is of no consequence. For extremely large system sizes, however, even thermalization can be challenging and can take days or even weeks of computer time and will not be speed up with the conventional ansatz. One problem with the parallelization of the worm update is its indeterministic nature. In particular, the worms have to be synchronized after each step one has to check whether they merge or not. An effective implementation can be achieved on a SMP platform where the update step for each worm is performed by different threads. Since the threads have access to the same physical memory synchronization is much faster as on distributed memory machines. The actual implementation, however, is still work in progress.

4. The Supersolid Nucleation Transition

The hardcore Bose-Hubbard model with nearest neighbor repulsions, as introduced in Chapter 1.4, is considered in this section. Geometrical frustration leads to the proliferation of an extended supersolid sandwiched between the two insulating phases at filling one third and two thirds. Although this model has been investigated thoroughly in the last years [70, 72–75, 88, 89], the true nature of the supersolid quantum nucleation is not completely understood. Indeed, analytical calculations [88, 261] and a numerical mean-field approach [280] point towards an interplay between a first-order and continuous transition, however, no exact numerical treatment of this transition has been performed, yet.

Quantum nucleation of the triangular lattice supersolid into the superfluid phase is governed by the underlying \mathbb{Z}_q symmetry in three dimensions. In the generic case i.e., for $\mu/V \neq 3$, the \mathbb{Z}_3 vector model undergoes a discontinuous disordering transition [112]. Therefore, the supersolid nucleation transition is predicted to be first-order as well. This conclusion is consistent with Monte Carlo simulations for the thermal melting transition of the supersolid which undergoes at BKT transition related to the superfluid part and a two-dimensional $q = 3$ Potts transition of the solid component [75], as expected from the classical theory, and a recent mean-field analysis of the triangular lattice supersolid [93, 280, 281]. At $\mu/V = 3$, symmetry arguments imply that the supersolid-superfluid transition is continuous and in the 3D XY universality class since the discreteness of the \mathbb{Z}_q vector model becomes irrelevant for $q \geq 5$ in three dimensions [114–117]. The behavior of the classical two-dimensional \mathbb{Z}_6 model implies that the supersolid melting transition at the particle-hole symmetric point driven by thermal fluctuations should exhibit three transitions and, in particular, a XY quasi-solid with algebraic density correlations [114–118]. Though, this intermediate phase has not been observed but Boninsegni *et al.* report [75] that the melting tran-

4. The Supersolid Nucleation Transition

sition is consistent with $q = 3$ Potts behavior even at $\mu/V = 3$ and the BKT and Potts transition occur simultaneously within numerical uncertainties. This does not need to imply that the quantum melting transition is discontinuous and the scenario of symmetry enhancement is false. So far, the coupling of the superfluid density to the solid order parameter has been neglected. In the 2+1 dimensional case, this coupling is not relevant for the 3D XY fixed point[88, 261]. The interplay of superfluidity and solid order in two dimensions is not fully resolved and thus the symmetry enhancement picture can break down in the lower dimensions giving rise to the behavior observed by Boninsegni *et al.* Also, the stability of the XY quasi-solid is questionable since frustration, that is essential for the prevention of phase separation between the superfluid and solid, is irrelevant and the XY quasi-solid will not be present in two dimensions. This chapter provides a comprehensive numerical analysis, that has been submitted to Physical Review Letters and can be found on the arXiv preprint server [92], of the quantum nucleation transition supporting the scenario of symmetry enhancement. Clear evidence for the proliferation of a (weak) first-order transition and unbiased estimates of the universal properties of the critical end-point are presented.

4.1. Generic Case

Distinguishing a (weakly) first- and second-order phase transition can be challenging due to restrictions in the accessible lattice sizes with respect to the relevant correlation length. Far away from $\mu/V = 3$ in the vicinity of the solid phase the system exhibits a clear jump for sufficiently large system sizes L in the filling n , superfluid density ρ_s and the structure factor S/N at the supersolid-superfluid transition, as shown in Figure 4.2 and Figure 4.4. The phase coexistence is also reflected in the histograms recorded in the vicinity of the transition point and a clear two-peak structure emerges (see Figure 4.3 and the inset in Figure 4.4). Moving even closer towards $\mu/V = 3$, the jump Δ of the structure factor S/N at the transition is obtained from the distance of the peak in the order parameter histogram at the transition point, as sketched in Figure 4.3.

Moving in parameter space towards $\mu/V = 3$, the DLRO (and also ρ_s) weakens,

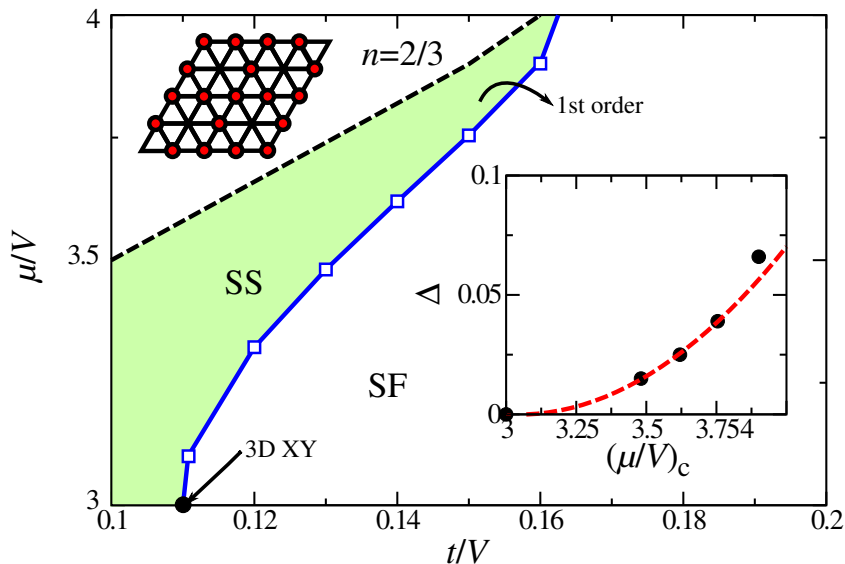


Figure 4.1.: Ground state phase diagram for hardcore bosons with nearest neighbor repulsion on the triangular lattice near the superfluid-to-supersolid transition region. The blue line denotes a the first-order supersolid nucleation transition whereas the black dashed line represents the 3D XY solid-supersolid transition. The line of first-order transitions terminates in a critical (3D XY) end-point (black circle) at the particle-hole symmetric point $\mu/V = 3$. The lower inset shows the jump Δ of the order parameter corresponding to the solid order shown in the upper inset along the transition line as a function of the critical ratio $(\mu/V)_c$. The dashed line in the inset is a quadratic fit for $\Delta < 0.05$ to the deviation of $(\mu/V)_c$ from 3 (half-filling).

4. The Supersolid Nucleation Transition

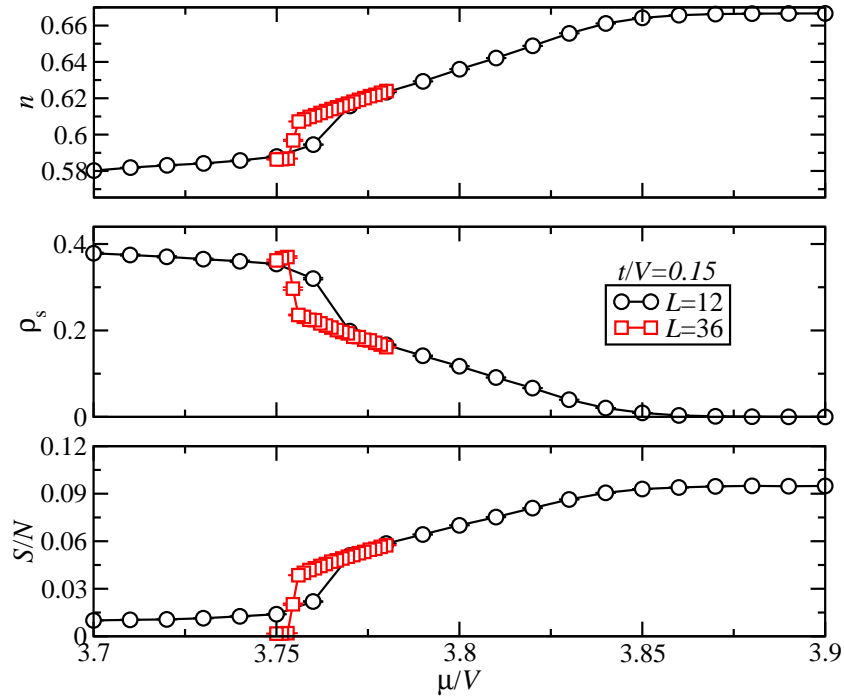


Figure 4.2.: Filling n , superfluid density ρ_s and structure factor S/N for $L = 12$ and 36 and $\beta = 100V$ at $t/V = 0.15$.

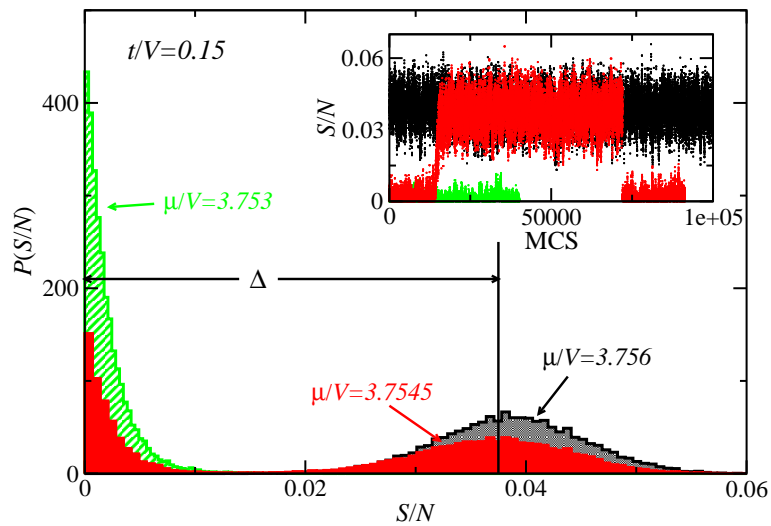


Figure 4.3.: Histogram for the order parameter S/N at $t/V = 0.15$ for $L = 36$ and $\beta = 100V$. A clear two-peak structure emerges at $\mu/V \approx 3.7545$. The inset shows a part of the Monte Carlo timeseries from which the histograms are obtained.

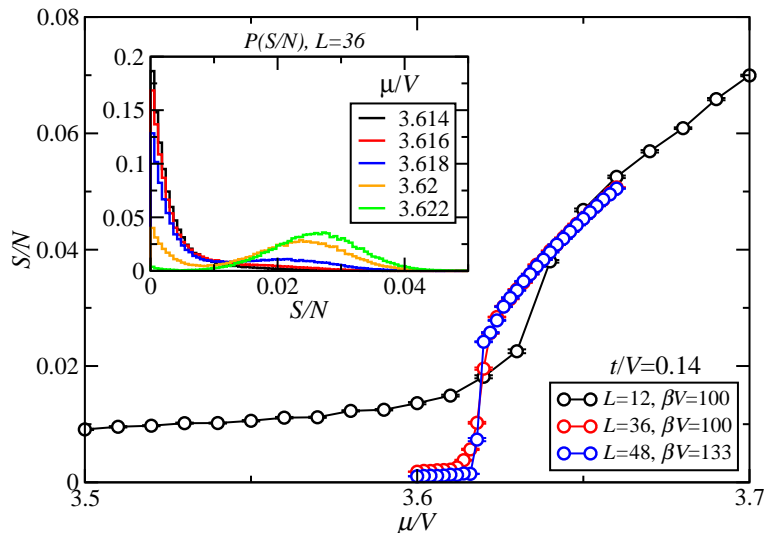


Figure 4.4.: Structure factor for $L = 12, 36$ and 48 at $t/V = 0.14$ across the supersolid-superfluid transition. The inset shows the order parameter histograms at different values of the chemical potential μ/V for $L = 36$.

and the jump Δ in the order parameter decreases, as seen from the inset of Figure 4.1. Figure 4.5 shows the filling n , the superfluid density ρ_s and the order parameter S/N as functions of μ/V for $t/V = 0.13$, in the vicinity of the SF-SS quantum phase transition. The data appears to vary smoothly across the transition, in contrast to the results shown in Figure 4.2. Thus, former numerical investigations concluded that the supersolid-superfluid transition is continuous in the generic case [72]. The histograms of S/N shown in Figure 4.6 for sufficiently large systems, however, reveal the emergence of a two-peak structure at $(\mu/V)_c \approx 3.48075$, which remains stable in the thermodynamic limit, as shown in the inset of Figure 4.6 and give a clear indication for a (weak) first-order transition. The jump of the order parameter at the transition point for $t/V = 0.13$ is estimated as $\Delta \approx 0.0125$. Looking at the data for $\mu/V = 3.1$ in Figure 4.7 obtained for very low temperatures ($TL = 0.2V$) or the histograms for $t/V = 0.12$ in Figure 4.8, a regime of phase coexistence can not be identified. In the vicinity of $\mu/V = 3$, Δ becomes very small and can be approximated by a quadratic fit $\Delta \propto ((\mu/V)_c - 3)^2$ (cf. the inset of Figure 4.1). Thus, the jump of the order parameter at $t/V = 3.1$ is estimated to be $\Delta \sim 0.002$. Taking into account the resolution of the order parameter scaling like $1/N$, it becomes clear

4. The Supersolid Nucleation Transition

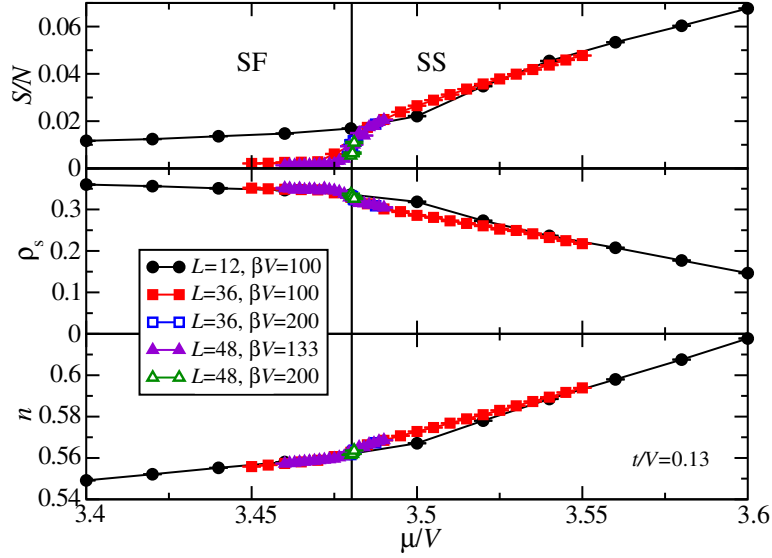


Figure 4.5.: Filling n , superfluid density ρ_s and structure factor S/N for $t/V = 0.13$ for various system sizes as functions of μ/V across the superfluid-supersolid transition.

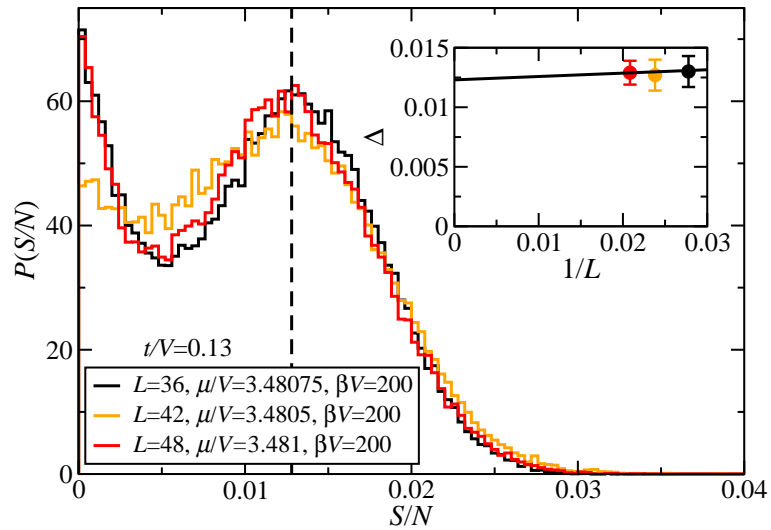


Figure 4.6.: Histograms of S/N obtained at $t/V = 0.13$ for different system sizes. Inset: Extrapolation of the peak position Δ to the thermodynamic limit.

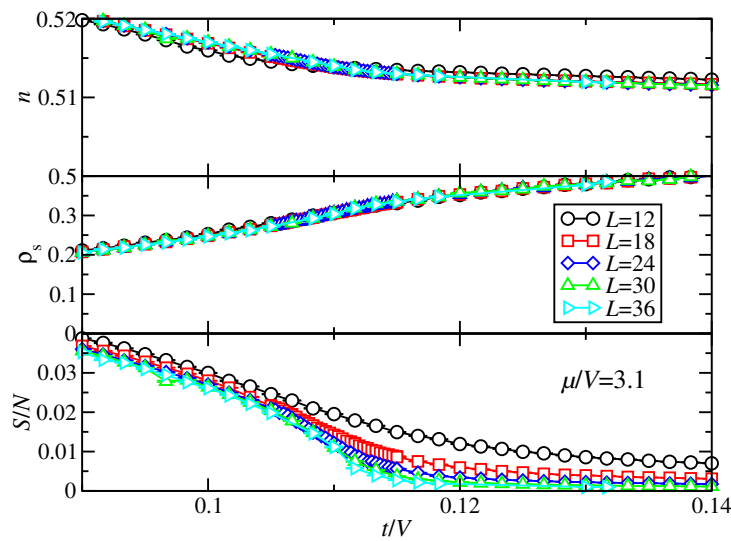


Figure 4.7.: Filling n , superfluid density ρ_s and structure factor S/N for $L = 12$ to 36 and $TL = 0.2V$ at $\mu/V = 3.1$.

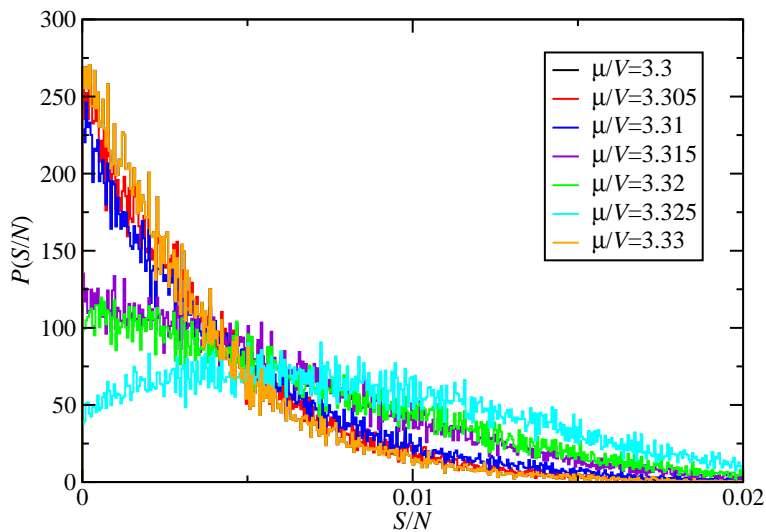


Figure 4.8.: Histograms of the order parameter S/N at $t/V = 0.12$ for $\beta = 200V$.

that a first-order transition, if it exists, is too weak to be accessed within the system sizes and temperatures available.

4.2. Critical Properties of the Particle-Hole Symmetric Point

After providing clear evidence for a first-order supersolid-superfluid transition over a wide range of parameters away from half-filling, with decreasing discontinuity upon approaching $\mu/V = 3$, the particle-hole symmetric point is considered. Fixing $\mu/V = 3$, the transition is expected to be continuous and no evidence of a first-order transition is found. In order to check whether the transition is within the 3D XY universality class, the critical exponents β , γ and ν (see Section 2.3) are extracted from a finite-size scaling analysis of the structure factor S/N and the associated susceptibility (cf. Figure 4.9)

$$\chi = (1/N) \int_0^\beta d\tau \langle \sum_{i,j} e^{i\mathbf{Q}(\mathbf{r}_i - \mathbf{r}_j)} n_i(\tau) n_j(0) \rangle. \quad (4.1)$$

The time dependent density operator is given as $n_i(\tau) = e^{H\tau} n_i e^{-H\tau}$. The scaling ansatz, as given in Equation (2.42), reads

$$S/N = L^{-2\beta/\nu} g[(t - t_c)/t_c L^{1/\nu}] \quad (4.2)$$

$$\chi = L^{\gamma/\nu} h[(t - t_c)/t_c L^{1/\nu}]. \quad (4.3)$$

The critical exponent, the critical point t_c and the exact form of the scaling functions $g(x)$ and $h(x)$ are not known a priori. The scaling analysis is performed in the following way. Firstly, the scaling functions are expanded into a Taylor series $g(x) = A + Bx + Cx^2 + Dx^3 + Ex^4 + \mathcal{O}(x^5)$ ($h(x)$ in analogy). This approximation is reasonable since $x = (t - t_c)/t_c L^{1/\nu}$ will, in general, be small in the scaling regime. The critical exponents and the critical point t_c as well as the Taylor coefficients are determined by a least-square fit of the numerical data for different systems sizes using a modified Levenberg-Marquardt algorithm [191]. Furthermore, the influence of a variation of the starting parameters of the fit has to be checked since the least-square fitting procedure can get stuck in local

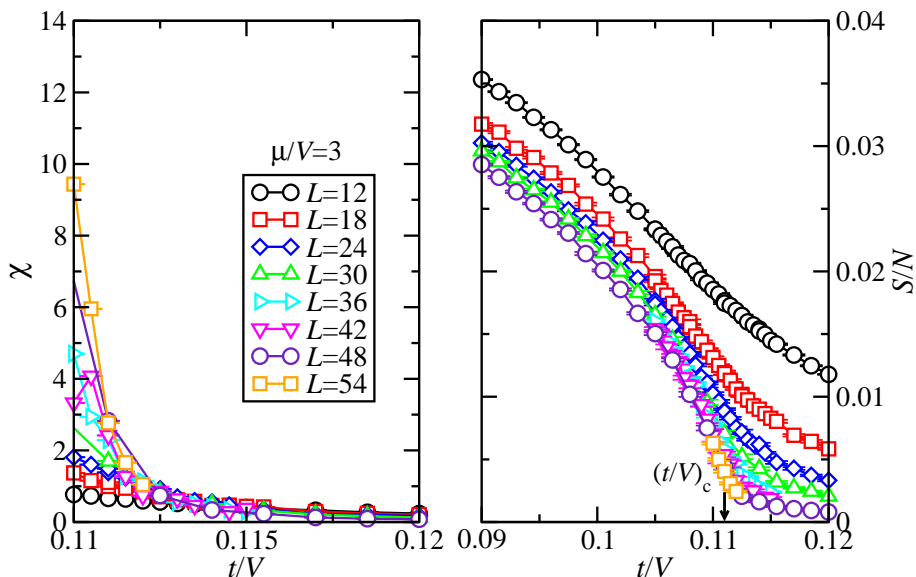


Figure 4.9.: Susceptibility χ and structure factor S/N for $\mu/V = 3$ and $TL = 0.1V$ for various system sizes.

minima, particularly, if the number of fitting parameters is large. Scaling is only valid asymptotically ($x \rightarrow 0$) in the scaling regime. However, the range of validity of Equation (4.3) is not known in advance and the influence of the fitting range has to be taken into account. Moreover, fixing a fitting range requires an increasing t resolution as the system sizes increase. In particular, a fitting range $|x| < 1$ corresponds to the interval $|t/t_c| \lesssim 1.025$ at $L = 12$ but $|t/t_c| \lesssim 1.002$ at $L = 60$ (using the 3D XY value for ν).

The actual implementation utilizes a `scipy` [282] wrapper for MINPACK [283]. The error on the fitting parameters is obtained by performing a Bootstrap analysis [191] using, for each data point, a Gaussian distribution around the mean value with a variance given by the Monte Carlo error. The expected critical behavior of 3D XY type has a dynamical critical exponent $z = 1$ [261], and therefore the simulations are performed fixing $LT = 0.1V$. The results from the Bootstrap analysis, only taking lattice system greater than $L = 12$ using Gaussian random noise and random starting variables for the fit in a certain interval, yields values for the critical exponents and the t_c as tabulated Table 4.1. The goodness of the fit is determined by the χ^2/DOF that is between one and three for the fits of S/N and about two to four for the susceptibility. Figure 4.10 shows a two dimensional scatter plot of the bootstrapped critical exponents,

4. The Supersolid Nucleation Transition

	S/N	χ	3D XY [284]	3D Heisenb. [285]	3D Ising [285]
β	0.32(2)	-	0.3468(1)	0.365(12)	0.3028(12)
ν	0.67(2)	0.68(4)	0.6717(1)	0.710(6)	0.631(2)
γ	-	-1.3(2)	-1.3178(2)	-1.300(6)	-1.2385(25)
$(t/V)_c$	0.1108(2)	0.1105(3)	-	-	-

Table 4.1.: Critical exponents obtained from quantum Monte Carlo data of the order parameter S/N and the susceptibility χ for $\mu/V = 3$ in comparison with high-precision value for the 3D XY, Heisenberg and Ising universality classes.

where the size and the color of the data points denote the goodness of the fit. All histograms for the critical exponents are shown in Figure 4.11. It is noticeable that the critical exponent for 3D $O(N)$ models¹ (see Table 4.1) are very similar thus small deviations or an insufficient quality of the Monte Carlo data can lead to ambiguous results² and it is necessary to have at least three critical exponents to compare i.e., β and γ are consistent with 3D XY and 3D Ising whereas ν is compatible with 3D XY and 3D Heisenberg exponents (taking a $1-\sigma$ interval). The data collapse with the obtained critical exponents is shown in Figure 4.12. Thus, this work concludes that the supersolid-superfluid transition is continuous and compatible with a 3D XY quantum phase transition.

This part concludes with commenting on the question why only simple scaling was used and corrections to scaling, as given in Equation (2.43), are not taken into account. It turns out that in this case the goodness of the fit is not increased significantly when including scaling corrections. At the same time one increases the number of fitting parameters (c , ω and d , ϕ) rendering the fit unstable. For instance, there is a competition between the c and $L^{-\omega}$ thus the fitting algorithm can run into a situation where c becomes large and positive but is compensated by a large value of ω and vice versa. This is reflected in the case where additional attractors appeared during the fitting procedures that can be traced back to

¹ $N = 1$: Ising, $N = 2$: XY, $N = 3$: Heisenberg

²It has been reported [76] that the supersolid-superfluid transition in a square-lattice bilayer antiferromagnet is in the 3D Ising universality class by checking the goodness of the data collapse (in an unspecified way) with the exact critical exponent. This is in contrast to the field-theoretical expectation for a checkerboard supersolid state [261, 286] but due to the similarity of the 3D critical exponents only an unbiased determination of the critical exponents will shed some light to this issue.

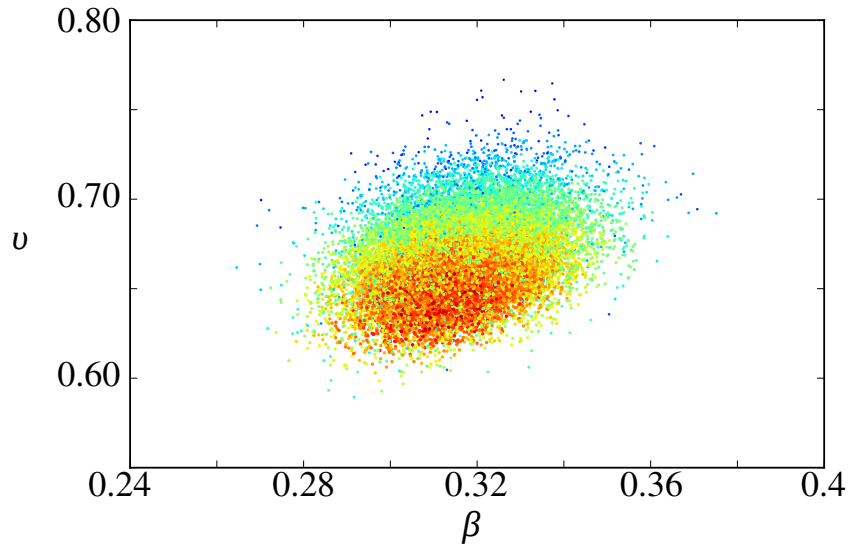


Figure 4.10.: Results for the bootstrapping analysis of the S/N data. The color denotes the χ^2/DOF (from 1.5 (red) to 3 (blue)).

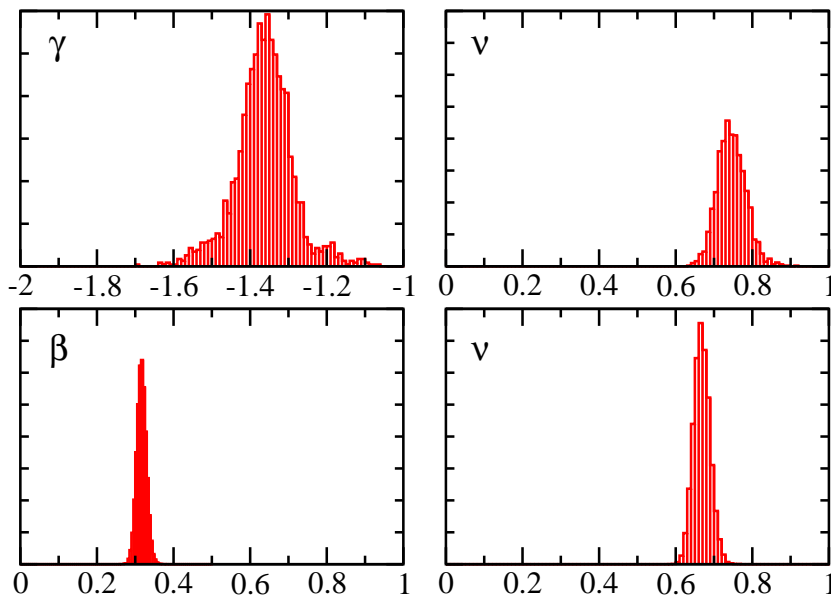


Figure 4.11.: Histograms of the Bootstrap analysis from the susceptibility (first row) and structure factor (second row).

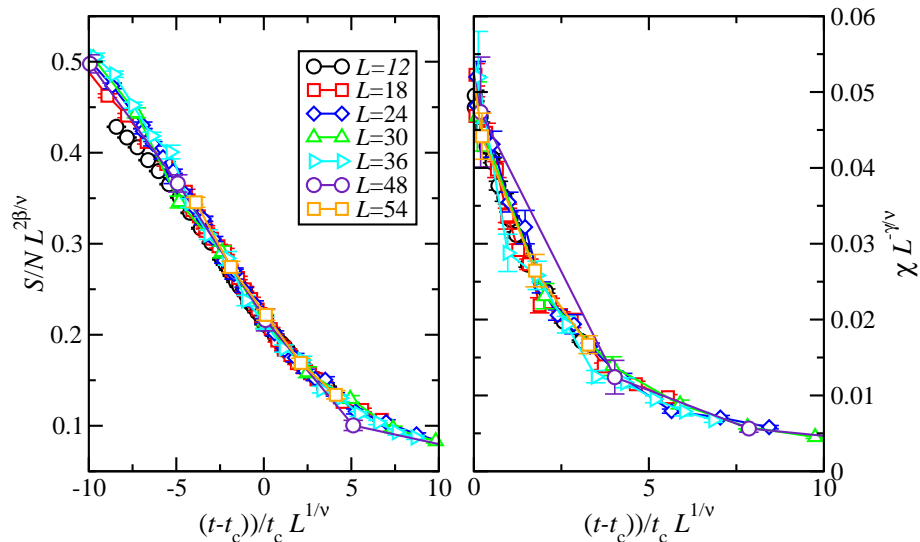


Figure 4.12.: Data collapse of the structure factor S/N and the susceptibility χ for $\mu/V = 3$ and $LT = 0.1$.

the aforementioned situation and the fitting procedure is complicated severely. Neglecting the smallest system sizes ($L = 6$ and $L = 12$) and choosing x small enough seem sufficient for the case considered.

4.3. SS-C at Finite Temperatures

A recent cluster-mean field analysis [89] predicts the existence of a third supersolid phase with an ordering pattern $(\epsilon, -\epsilon, 0)$, SS-C, at finite temperatures. SS-C is obtained for $t/V = 0.1$ for temperatures $T/t > 0.5$ up to $T/t = 6$. This temperature regime, however, is far beyond the thermal melting transition found by Boninsegni *et al.* and, furthermore, SS-C is excluded at $T = 0$ by symmetry arguments [75]. A robust way to numerically distinguish the supersolid phases, despite looking directly at the generalized magnetization, given in Equation (1.11), is to monitor the histograms of the local densities [75]. Denoting by

$$\bar{n}_i = \beta^{-1} \int_0^\beta d\tau n_i(\tau) \quad (4.4)$$

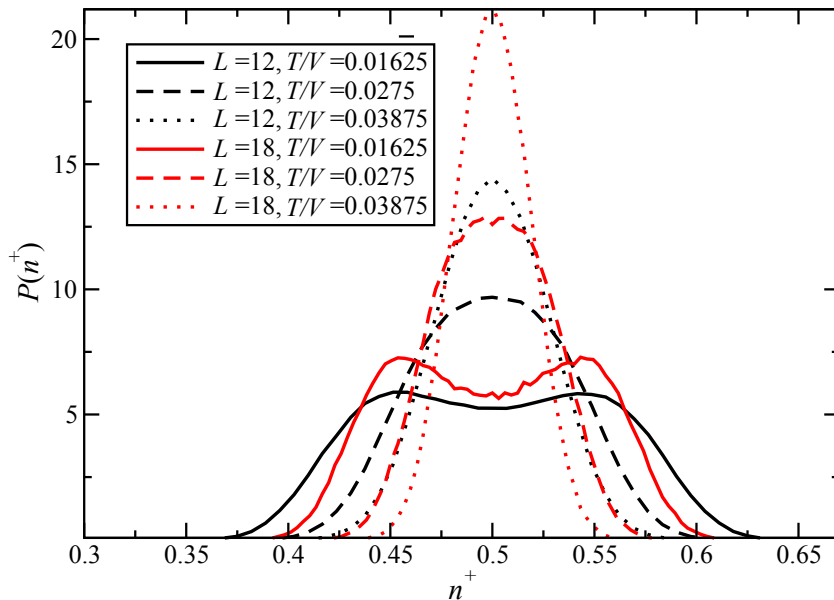


Figure 4.13.: Histograms P of n^+ taken at $W = 0$, $t/V = 0.1$, $\mu/V = 3$ for different temperatures and system sizes.

the imaginary time averaged local density at site i , one obtains the fraction of sites with mean occupation $\bar{n}_i > 1/2$ from the observable

$$n^+ = \frac{1}{N} \sum_{i=0}^N \theta(\bar{n}_i - 1/2), \quad (4.5)$$

where θ denotes the Heaviside function. From the sublattice density patterns one can immediately see, that the histogram of n^+ , $P(n^+)$, is peaked below (above) $1/2$ for SS-A (B) and right at $1/2$ for SS-C. The high-temperature results at $\mu/V = 3$ for $P(n^+)$ are shown in Figure 4.13. As temperature is increased, the peaks move towards $1/2$ and eventually, they become indistinguishable for T/t beyond 0.25 due to their finite width. In addition, thermal disorder leads to a substantial weight at $n^+ = 1/2$ that does not come from density fluctuations from a SS-C phase. Within quantum Monte Carlo, the SS-C thus remains elusive.

5. Triangular Supersolid beyond Two-Body Interactions

In Chapter 4 it was shown that geometrical frustration leads to a rich phase diagram when placing hardcore bosons with nearest-neighbor repulsion on a triangular lattice. The supersolid-supersolid transition and the critical properties of the supersolid nucleation crucially depend on the particle hole symmetry of the Hamiltonian in Equation (1.7) around $\mu/V = 3$. Polar molecules offer the possibility to realize a Bose-Hubbard like system where one can explore a regime beyond nearest-neighbor two-body interactions. In particular, tunable two- and three-body interactions can be accessed by appropriately adjusting the interactions of polar molecules in the presence of external fields. The three-body Hamiltonian reads

$$H = -t \sum_{\langle ij \rangle} b_i^\dagger b_j + \sum_{ij} \frac{V_{ij}}{2} n_i n_j + \sum_{ijk} \frac{W_{ijk}}{6} n_i n_j n_k - \mu \sum_i n_i, \quad (5.1)$$

where $V_{ij} = V/r_{ij}^6$ and $W_{ijk} = W \left[1/r_{ij}^3 r_{ik}^3 + 1/r_{ij}^3 r_{jk}^3 + 1/r_{ik}^3 r_{jk}^3 \right]$ are the two- and three-body couplings. The leading contribution $\sim 1/r_{ij}^3$ can be neglected in the relevant parameter regime [142].

This chapter will provide a detailed study of the impact of nearest-neighbor and extended two- and three-body interactions on the triangular supersolid using large-scale quantum Monte Carlo simulations with an extended cluster approach. In this context, the concept of nearest-neighbor three-body interactions fits the tripartite nature of the triangular lattice as it resembles plaquette interactions penalizing fully occupied triangles. Classically, Ising (Baxter-Wu model) and Potts (Schick-Griffiths model) models with two- and three-body have been studied both numerically and by analytical methods [95, 287–290]. From these results,

5. Triangular Supersolid beyond Two-Body Interactions

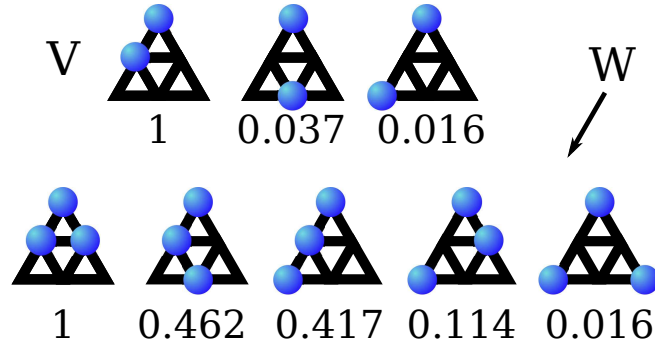


Figure 5.1.: Leading contributions to the many-body interactions for polar molecules on a triangular optical lattice. Numbers below the interaction terms denote the relative strength of the two- (three-) body terms in units of the nearest-neighbor values V (W).

one can anticipate the proliferation of the $n = 2/3$ solid in the case of purely three-body interactions and the stabilization of the $n = 1/3$ solid as two-body repulsions are increased.

This chapter is concerned with the question, whether the main features of the triangular supersolid still persist in the presence of three-body interactions and the interplay between two- and three-body interactions is studied in the quantum regime. First, only the nearest-neighbor case is considered and, in the second step, up to fifth-nearest neighbor interactions are taken into account. This is done by using a vertex decomposition of the Hamiltonian in terms of six-site cluster, as shown in Figure 5.1, for the directed loop algorithm. Since the potential decays rapidly like $1/r^6$, this decomposition is a good trade-off between an efficient implementation and capturing the main features of the extended interactions. This discussion will follow the results already published in Physical Review B [78]. One remarkable result of this investigation is that a supersolid phase will be stabilized for arbitrarily small two-body interactions i.e., geometrical frustration immediately drives the supersolid transition even if the $n = 1/3$ solid is unstable. Moreover, particle-hole symmetry will be restored dynamically and the first-order supersolid-supersolid transition, discussed in Chapter 4, is recovered. This insight is compatible with mean-field theory and Monte Carlo simulations by Zhang *et al.* [281] who concentrate on a detailed analysis of a small range of two- and three-body interactions. The inclusion of extended interactions does not take into account the exact asymptotic $1/r^6$ behavior but a cut-off is introduced such

that the interactions can be described by a set of finite-size interaction vertices maxing out the capabilities of the vertex decomposition in the stochastic series expansion framework (cf. Section 2.1.1). The inclusion of long-range interactions leads to new features like proliferation of low-energy metastable state [291] and exotic transition mechanism like the Spivak-Kivelson bubble transition [292], as found by Pollet *et al.* for the triangular supersolid including all $1/r^3$ long-range interactions [293]. However, in contrast to the square lattice case [286] no evidence for the proliferation of new supersolid regimes are found but new insulating plateaus at unconventional fillings appear. In conclusion, the triangular supersolid is robust towards extended two- and three-body interactions as they can be realized in a setup with polar molecules and is a promising candidate for the realization of lattice supersolidity in future experiments.

5.1. Nearest-Neighbor Interactions

Classically, the phase diagram of Ising (Baxter-Wu model) and Potts (Schick-Griffiths model) models with two- and three-body is well understood [95, 287–290]. Thus, the classical, $t = 0$, model, see Equation (1.8), will exhibit a $n = 2/3$ solid for $V/W = 0$. Turning on the two-body interactions, nearest-neighbor occupied sites will be penalized and the $n = 1/3$ will proliferate.

The full ground-state phase diagram obtained from quantum Monte Carlo simulations is shown in Figure 5.2. It is divided into a regime where $V > W$ (upper panel) and $W < V$ and the hopping is chosen such that $t = 0.1\max(W, V)$. For $W/V = 0$, one recovers the results from Chapter 4 where two SS-A and SS-B are sandwiched between the $n = 1/3$ and $2/3$ solid. In analogy to Chapter 4, the solid, superfluid and supersolid order is identified by the structure factor S/N and the superfluid density ρ_s . Figure 5.3 shows these quantities for different values of W/V . It is found, that the supersolid state, realized on the triangular lattice in the absence of three-body interactions remains stable even for large values of W/V . However, the supersolid regime narrows but only in the limit of purely three-body interactions ($V = 0$) is the supersolid destroyed. The solid phase of filling $n = 1/3$ is stable up to $W \approx 2V$. This destabilization of the $n = 1/3$ solid is consistent with results obtained for the classical limit ($t = 0$) [95, 290].

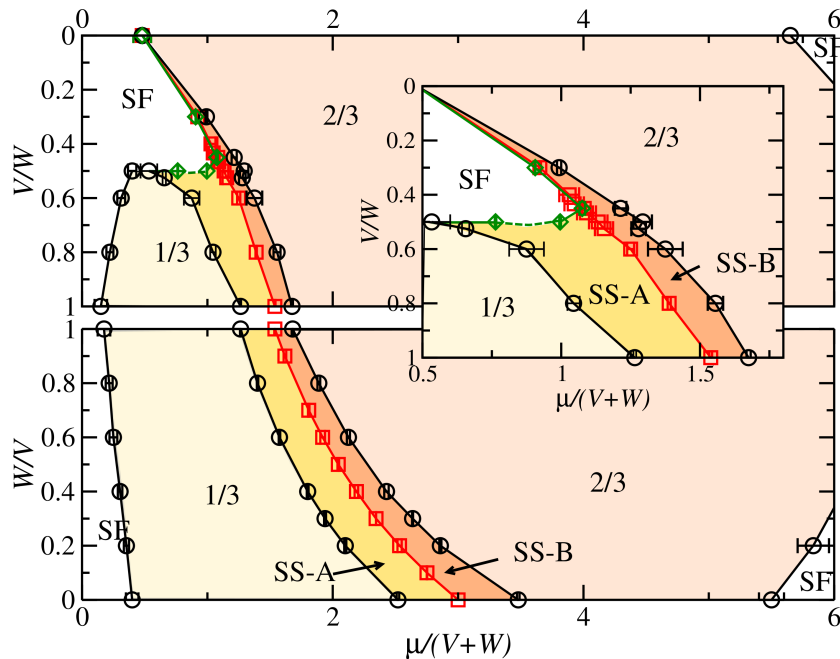


Figure 5.2.: (Color online) Ground state phase diagram of polar molecules on a triangular lattices. The upper (lower) panel shows the regime $W > V$ ($V > W$), at $t/W = 0.1$ ($t/V = 0.1$). SF denotes superfluid regions, SS-A and SS-B the two supersolid regimes, that meet at a first-order quantum phase transition along the line of half-filling, $n = 1/2$ (squares). Diamonds trace the SS-SF transition line. The inset focuses in on the large- W region.

This results emphasizes the importance of the frustrating nature of the two-body interactions on the triangular lattice for the stabilization of a supersolid.

5.2. Extended Model

In the extended model the long-range nature of the dressed dipolar interactions is approximated by taking into account only interaction vertices drawn in Figure 5.1. First, consider the region where the supersolid is stabilized. In particular, Figure 5.4 shows n , ρ_S and S as functions of μ at $t/V = 0.1$ for different ratios $W/V < 1$ around the SS regime. An extended SS phase is clearly identified between the $n = 1/3$ and the $n = 2/3$ solid. Of particular interest are incompressible phases beyond the supersolid regime stabilized by three-body interactions. To explore these, the limiting case of purely three-body interactions

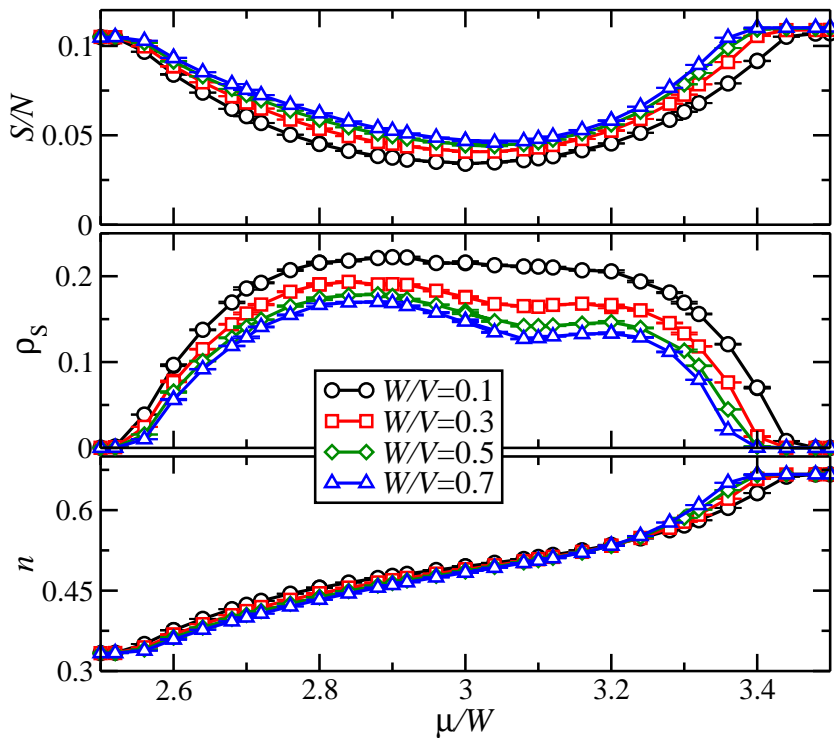


Figure 5.3.: Filling n , superfluid density ρ_s and structure factor S/N as a function of the chemical potential μ for various values of W/V at $t/V = 0.1$, taken for $L = 12$ and $T/t = 0.1$.

is considered ($V = 0$). Figure 5.5 shows quantum Monte Carlo data of the filling as a function of μ for different ratios t/W at $V = 0$. In addition to the previously identified density plateaus at fillings $n = 1/3$ and $n = 2/3$, incompressible phases at fillings $n = 3/8$, $1/2$, and $3/4$ are seen to emerge upon decreasing t/W . The spatial structures that characterize these solids are shown in Figure 5.6. In the $n = 3/8$ solid, the system forms irregular patterns based on nearest neighbor dimers. From inspecting various real space density distributions from the quantum Monte Carlo configurations, it is concluded that these dimers do not arrange in any periodic pattern. This dimerization leads to a strong energy penalty for finite values of V , such that this phase is unstable for $V > W$. Similarly, the $n = 1/2$ phase, where stripes of empty and occupied lattice sites alternate, is not observed within this parameter regime. The solid phase at $n = 3/4$ however remains stable; for example it is observed for $W/V = 0.2$, $t/V = 0.1$ around $\mu/V = 14$.

Due to the frustration induced by the competition between the two- and three-

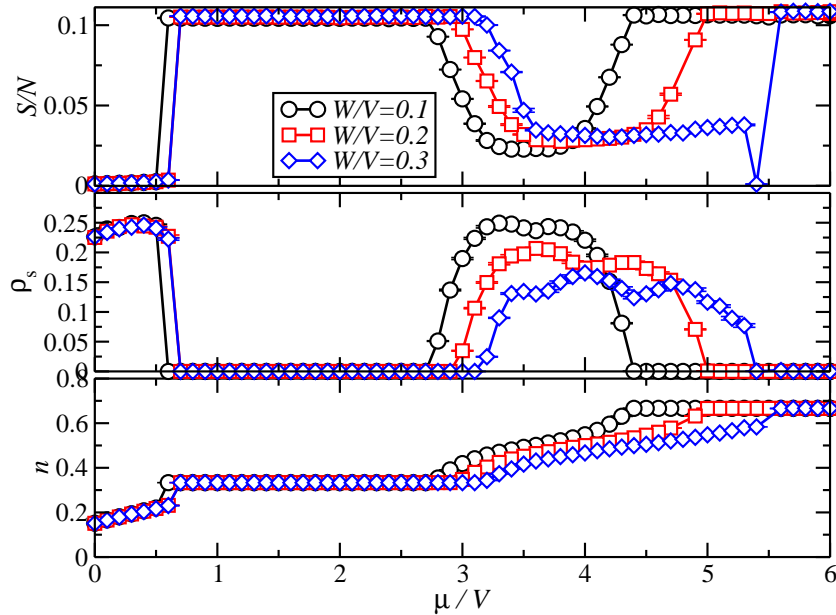


Figure 5.4.: Filling n , Superfluid density ρ_s , and the density structure factor S as functions of the chemical potential μ for different values of W/V at $t/V = 0.1$, taken for $L = 12$ and $T/t = 0.1$ in the extended model.

body interaction terms, one is able to perform ergodic simulations for the extended model only for ratios W/V up to about 0.3. For example, as the dip in the data for S/N near $\mu/V = 5.5$ in Figure 5.4 illustrates, one cannot reliably resolve the transition region between the SS phase and the $n = 2/3$ solid for the extended model. Using annealing techniques, the simulations did not improve within the transition region. It remains possible, that another, maybe incommensurate, phase appears here. Still, this issue remains inconclusive from the current simulations. Multi-body interactions at larger distances, as seen above for the case of purely three-body interactions, are in fact expected to stabilize additional plateaus at further fractional fillings, with the possible proliferation of low-energy metastable states [291] and Spivak-Kivelson bubble-type transitions between solid and superfluid regions [292]. However, a reliable numerical study of these issues is beyond the present approach. [69]

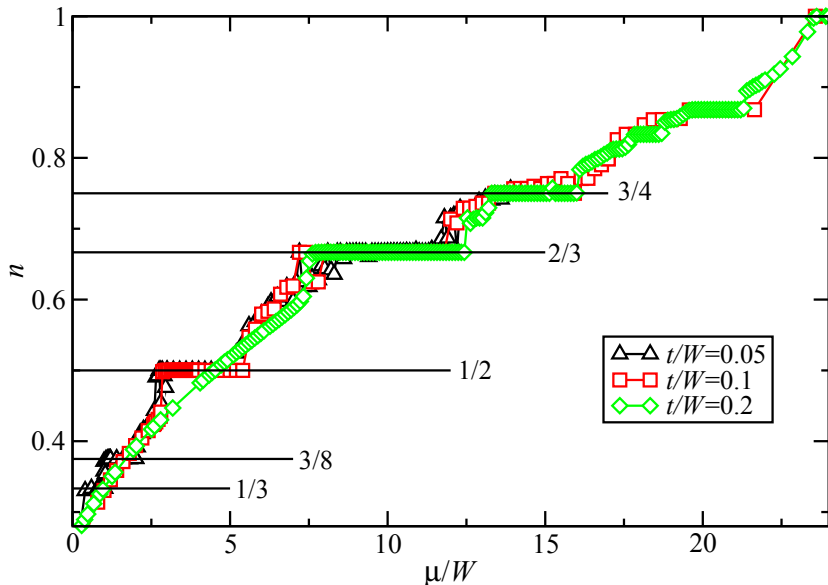


Figure 5.5.: Density n as a function of the chemical potential μ within the extended model for different values of t/W at $V = 0$, taken for $L = 12$ and $T/t = 0.1$.

5.3. Supersolid-Supersolid Transition

The supersolid-supersolid transition for $W = 0$ discussed in Chapter 4 is related to particle-hole symmetry around $\mu/V = 3$. The three-body interactions break this symmetry explicitly, as one can see from the data shown for various values of W/V in Figure 5.3 and Figure 5.4. Nevertheless, ρ_s and S/N , given in Figure 5.7 for $W/V = 0.3$, show a dip at half-filling. This feature is characteristic for the supersolid-supersolid transition for $W = 0$ [75], see Chapter 4. By monitoring the histograms of the time-integrated densities n^+ , previously introduced in Equation (4.5), the case of half-filling is visited and clear evidence for the existence of a SS-A to SS-B transition is found.

As an example, see the distributions $P(n^+)$ obtained for the nearest-neighbor and extended model in Figure 5.8 and Figure 5.9. First, note that the phases away from half-filling are actually of SS-A/B type, as $P(n^+)$ shows only one sharp peak close to $1/3$ and $2/3$ respectively, as displayed in the left panel of Figure 5.8. Right at $n = 1/2$, however, a solid two peak structure emerges, as the system size is increased, showing that particle-hole symmetry is restored dynamically at $n = 1/2$ for the minimal and extended set of interactions. The distribution of

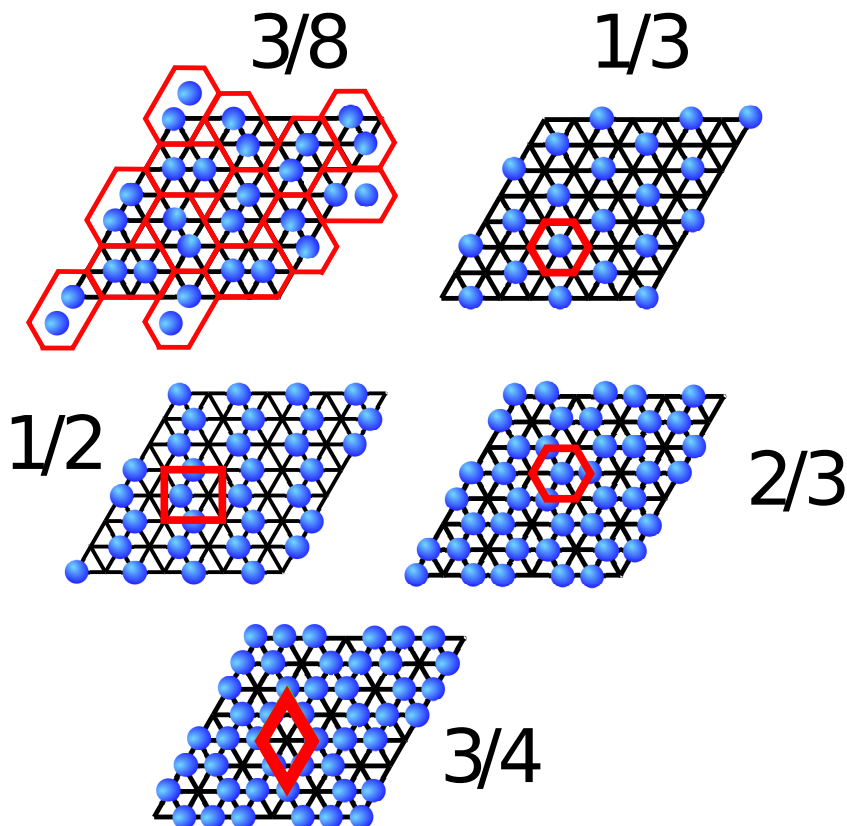


Figure 5.6.: Real-space structures of incompressible phases stabilized in the extended model, labeled by their filling fraction n . For crystalline states, the crystal unit cell is also indicated. For the $n = 3/8$ phase, which does not exhibit a periodic structure, a typical state is shown, consisting of an irregular arrangement of isolated dimers (pairs of neighboring occupied sites).

n^+ also rules out the possibility of the proliferation of a third supersolid phase, such as SS-C. Moreover, the suppression of superfluidity observed in Figure 5.7 is an indication for the discontinuous supersolid-supersolid transition.

It is argued in Section 5.1 that the $n = 1/3$ solid is stable up to $W \approx 2V$ but the supersolid phase in the nearest-neighbor model persists down to arbitrarily small values of W . The inset of Figure 5.2 shows a close-up of the parameter regime where the $n = 1/3$ solid vanishes. At the tip of the $1/3$ lobe, one observes a supersolid reentrance phenomenon where, for a fixed ratio of V/W , the system undergoes a solid-SS-A transition upon increasing $\mu/(V + W)$. However, the SS-A does not have a direct transition to SS-B but enters the superfluid and reenters SS-A before reaching the supersolid-supersolid transition at $n = 1/2$.

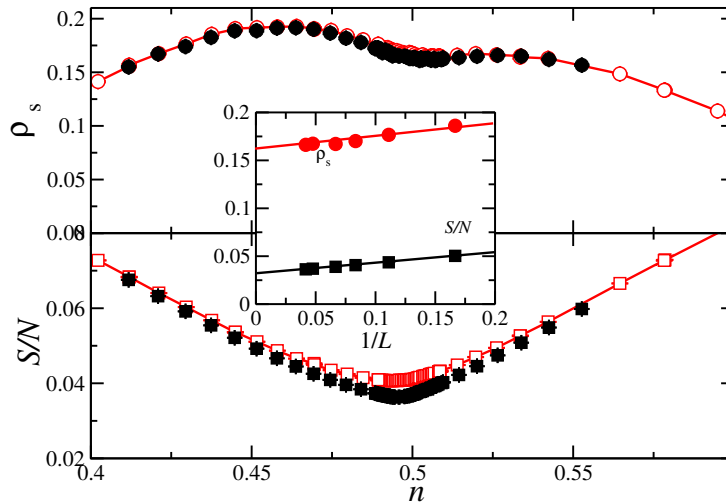


Figure 5.7.: Superfluid density ρ_s and structure factor S/N for different fillings n . **Inset:** Finite-size extrapolation of ρ_s (circles) and S/N .

This behavior is exemplified for $V/W = 0.5$ and $t/W = 0.1$ in Figure 5.10. SS-A melts at $\mu/W \approx 1.09$ into a superfluid and supersolid order is recovered at $\mu/W = 1.5$ and $n < 1/2$. The SSA-SSB transition occurs at $\mu/W \approx 1.8$. Within the remaining supersolid stripe it is also confirmed, that SS-A is stable i.e., there is no direct transition from the superfluid into SS-B but the supersolid stripe always features a SS-A and SS-B stripe. In particular, for $W/V = 0.3$, one enters the supersolid at $n = 0.48(1) < 1/2$. However, the density of interval of SS-A and SS-B become narrower as W/V decreases and eventually meet at $W = 0$ where no evidence for a supersolid phase is obtained.

5. Triangular Supersolid beyond Two-Body Interactions

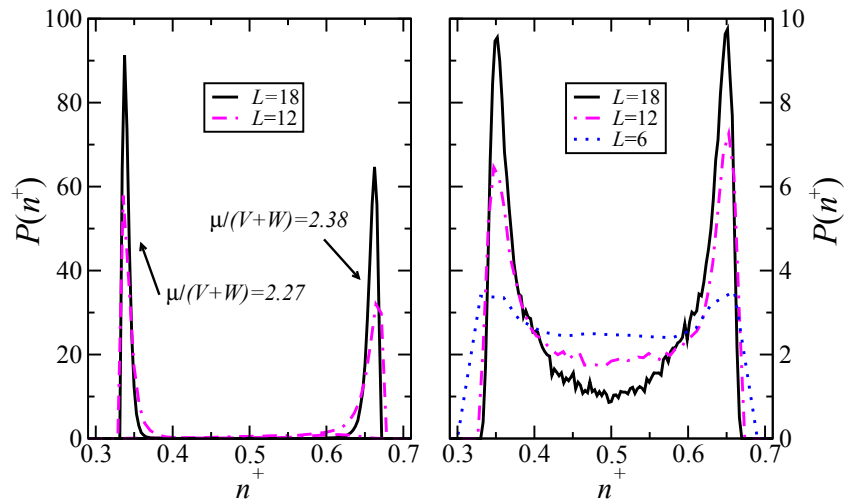


Figure 5.8.: Histogram P of n^+ for different system sizes taken at $t/V = 0.1$, $W/V = 0.3$, and $T/t = 0.05$ within the SS-A and SS-B phase (left panel) and at the SS-SS transition at $n = 1/2$ (right panel).

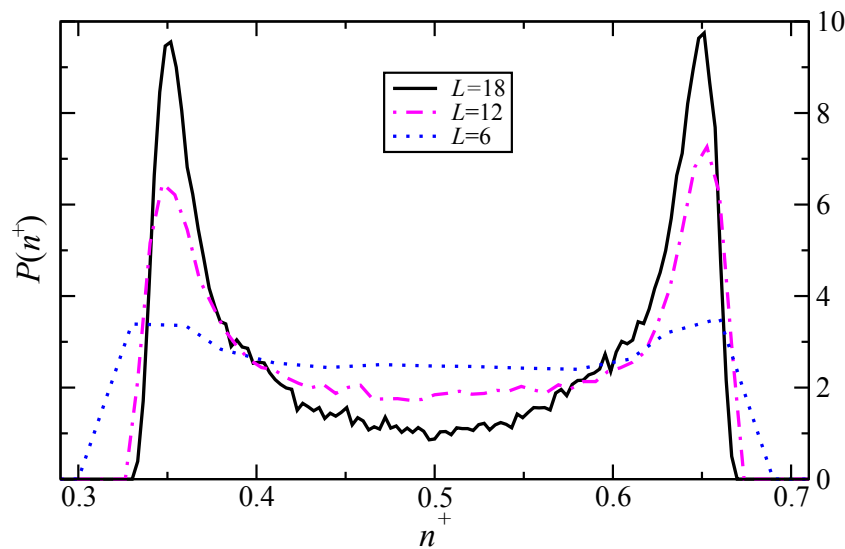


Figure 5.9.: Histograms P of n^+ for different system sizes taken for the extended model at $W/V = 0.1$, $t/V = 0.1$ and $T/t = 0.1$ at half-filling $n = 1/2$.

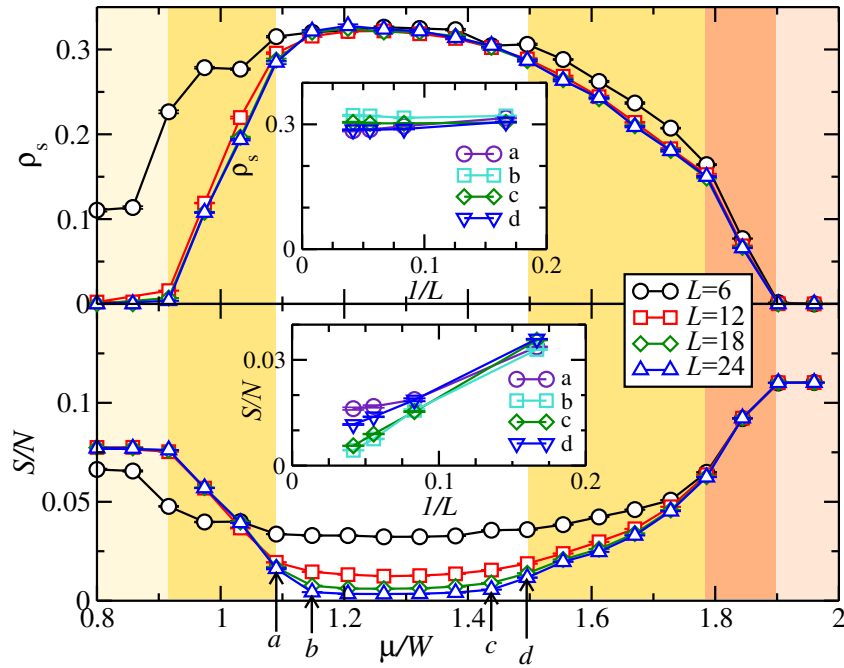


Figure 5.10.: Superfluid density ρ_s (upper panel) and structure factor S (lower panel) at $V/W = 0.5$, $t/W = 0.1$ for different system sizes. The different phases are highlighted (light) yellow for (the low density solid) SS-A and (light) red for (the high density solid) SS-B, respectively. The inset shows finite size extrapolations for the structure factor at $\mu/W = 1.09$ (a), 1.148 (b), 1.438 (c), and 1.496 (d).

6. Frustrating Three-body Interactions on the Honeycomb Lattice

The interplay of competing interactions and quantum fluctuations is known to allow for interesting phases to emerge in many-body quantum systems. This route towards novel phases of matter has been explored intensively in recent years, in particular in the field of low-dimensional quantum magnetism [294], and in the context of ultra-cold quantum gases on optical lattices, where one gains a high degree of control of the interaction strength [16]. The dominant inter-particle potentials in such systems are typically described by two-body interaction and exchange terms. Following from the discussion in Section 1.5. it appears fruitful to explore also realistic set-ups of many-body quantum systems that are dominated – via engineered interaction potentials – by multi-body interaction terms of e.g. three-particle type. Indeed, recently, polar molecules have been proposed as promising candidates towards realizing such many-body systems. In a recent work [142] an effective interaction potential was derived for polar molecules on an optical lattice in the presence of static electric and microwave fields. It was found, that upon appropriately tuning the external fields, the interactions between the polar molecules become characterized by extended strong two- as well as three-body interactions, as detailed in Section 1.5.

Frustration in statistical physics, manifesting itself in an extensive ground-state degeneracy emerging from energy constraints that can not be satisfied simultaneously, can give rise to interesting phenomena such as order-by-disorder [143] where fluctuations lift the ground-state degeneracy by selection certain states that have larger kinetic energies (quantum fluctuations) or maximize the entropy (thermal fluctuations). By placing hardcore Bosons with three-body interactions on a honeycomb lattice a multitude of different phases emerge that

show signs of frustration in the classical limit. This frustration can be understood in terms of complex solid structures emerging at unconventional filling factors. This chapter presents an extensive numerical study of the phase diagram of this model. Large scale classical and quantum Monte Carlo simulations are performed and the results are published in *New Journal of Physics* [144]. The interplay of nearly-degenerate degrees of freedom and the complexity of the appearing (valence bond) solid structure call for advanced numerical techniques and an appropriate vertex decomposition in combination with extended ensemble methods (namely, parallel tempering [194, 199, 203, 205, 207, 208]). Attention is drawn to the rich valence bond solid (VBS) structure in the quantum regime lifting the classical degeneracies and gives rise to effective models in terms of random tiling and quantum dimer models with both density and bond ordering.

Adding competing two-body interaction leads to a cascaded transition to the checkerboard solid that has been identified for the pure two-body case [295]. In the classical limit, the cascaded transition can be understood by an explicit construction of checkerboard domain walls inspired by the $n = 9/16$ solid that corresponds to a close-packing of bosons minimizing the three-body interaction. The extremely large superstructure make the effective simulation on finite-size systems very hard since one has many competing low-energy states and the problem of commensurability of the lattice structure with the finite system size. The complexity of the emerging models underlines the special properties of three-body interactions on the honeycomb lattice.

Lastly, a novel tensor algorithm for classical systems, the Tensor Network Renormalization group (TNRG) [217], is implemented. By rewriting the partition function as a contraction of a tensor network, a real space coarse graining procedure can be applied that allows for a systematic approximation of Z in the thermodynamic limit. The correct choice of the initial tensor allows the incorporation of three-body interaction into the TNRG framework, that is derived in detail in Section 2.2. The renormalization scheme can be used to effectively access the high temperature properties of classical systems. However, the applicability of the update scheme is found to be limited by rounding errors. The large range of the tensor elements, that basically are given by Boltzmann factors, becomes much large than the precision of the floating point arithmetics.

Resorting to high-precision floating point implementations [296], the regime of convergence of the TNRG algorithm can be extended. However, the numerical performance is restricted by the need for high numerical accuracy beyond `long double` precision¹ floating point arithmetics.

The interaction potential for polar molecules within an optical lattice in the parameter regime, where three-body and two-body interactions are present takes the form

$$V_{\text{eff}} = \frac{1}{2} \sum_{ij} V_{ij} n_i n_j + \frac{1}{6} \sum_{ijk} W_{ijk} n_i n_j n_k, \quad (6.1)$$

with $V_{ij} = V/r_{ij}^6$ and $W_{ijk} = W/(r_{ij}^3 r_{jk}^3 + \text{perm.})$. Here, r_{ij} denotes the spatial separation between particles on lattice sites i and j , and n_i the local density at site i . The two-body interaction V and the three-body interaction W can be tuned to be of similar strength, $V \gtrsim W$, by varying the external electric and microwave fields, as derived in [142].

In the following, the particular the case of bosonic polar molecules is considered. Since the extended interactions decay rapidly with the inter-particle separations (c.f. Figure 6), the interactions are truncated after the leading terms, resulting thus in an extended hardcore Bose-Hubbard model with two- and three-body nearest neighbor interactions only,

$$H = -t \sum_{\langle ij \rangle} \left(b_i^\dagger b_j + \text{h.c.} \right) + V \sum_{\langle ij \rangle} n_i n_j + W \sum_{\langle ijk \rangle} n_i n_j n_k - \mu \sum_i n_i. \quad (6.2)$$

Here, b_i and b_i^\dagger denote boson annihilation and creation operators respectively, and the local density operator $n_i = b_i^\dagger b_i$ has eigenvalues 0 and 1 in the hardcore limit. Furthermore, t denotes the nearest-neighbor hopping matrix element, that is controlled by the depth of the confining optical lattice (i.e. the laser intensity in a laser-based realization of the optical lattice), and μ is a chemical potential, allowing to control the filling (i.e. the density) of the system between $n = 0$ (empty) and $n = 1$ (full).

¹The actual implementation of the `long double` depends on the actual compiler and platform. In this theses, `long double` refers to a 16 byte floating point number and has to be distinguished from quadruple precision denoting a 32 byte data type.

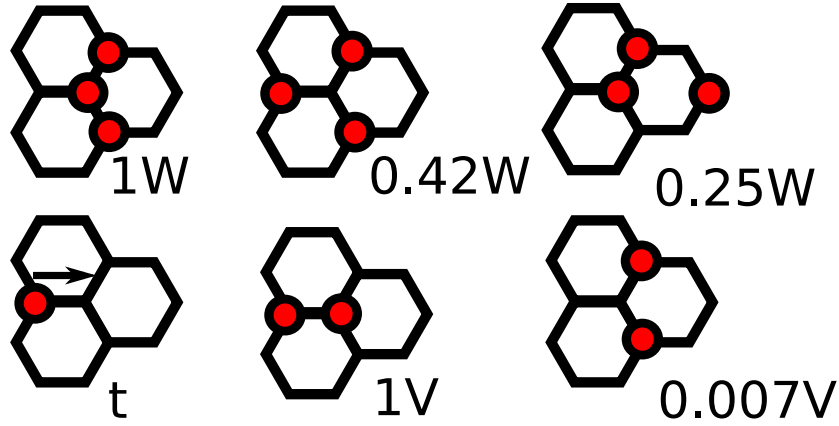


Figure 6.1.: Top row: Leading three-body repulsion terms and their relative strengths on the honeycomb lattice. Bottom row: Illustration of the nearest neighbor hopping term, and the relative strengths of the leading two-body repulsion terms on the honeycomb lattice.

6.1. Three-Body Interactions

In this section, the two-body interactions are neglected, $V = 0$, in order to explore explicitly the effects of three-body repulsions on the honeycomb lattice. The ground state phase diagram in Figure 6.2 summarizes the results from our analysis. It exhibits at low values of t/W a variety of incompressible phases of different (unconventional) fillings $n = 9/16$, $5/8 (= 10/16)$, $2/3$ and $3/4 (= 12/16)$. Due to the incompressible nature of these incompressible phases, they lead to finitely extended plateaus in the μ -dependence of the density n , as shown e.g. for fixed $t/W = 0.3$ in the inset of Figure 6.2. The actual nature of these phases and the quantum phase transitions between them, will be discussed below. For larger values of $t/W \gtrsim 0.4$, the system is eventually driven by its kinetic energy from these solid phases via first-order quantum melting transitions into a uniform superfluid phase with a finite superfluid density ρ_s . In the QMC simulations, the superfluid density is obtained as $\rho_s = \langle w^2 \rangle / (\beta t)$ from measuring the bosonic winding number w fluctuations in the standard way (see Section 2.1.2). The first-order nature of the melting transitions follows from pronounced jumps that are observed upon crossing the transition lines in both the density and the superfluid density. As a typical example, Figure 6.3 shows the behavior of n and ρ_s near the quantum melting transition between the $n = 9/16$ incompressible phase

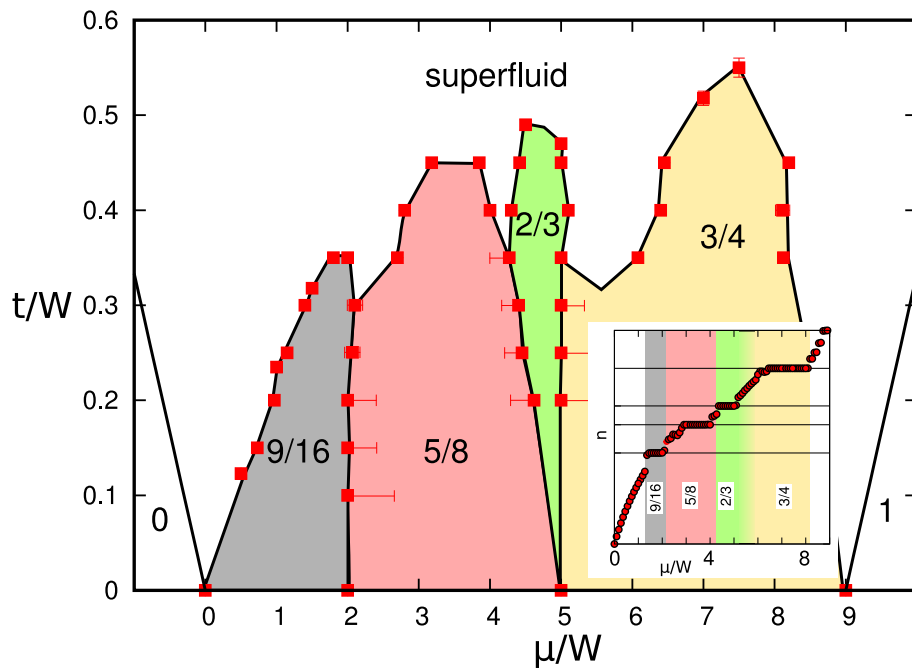


Figure 6.2.: Ground-state phase diagram of hardcore bosons on the honeycomb lattice for $V = 0$ in terms of μ/W and t/W . The incompressible phases at fillings $n = 9/16$, $5/8$, $2/3$ and $3/4$ are labeled by n and underlaid by different colors. Uncertainties on the estimated phase boundaries are indicated by error bars. The inset shows the density n as a function of the chemical potential μ/W for fixed $t/W = 0.3$, linear system size $L = 12$ and an inverse temperature of $\beta = 20W$.

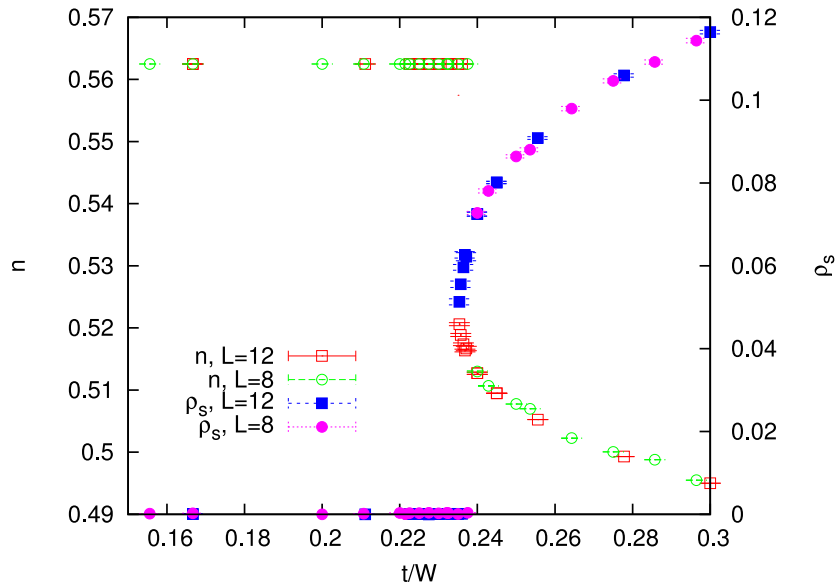


Figure 6.3.: Behavior of the density n and the superfluid density ρ_s near the quantum melting transition between the $n = 9/16$ incompressible phase and the superfluid phase at $\mu/W = 1$ and $V = 0$ taken at $\beta = 100$.

and the superfluid phase at $\mu/W = 1$. The first-order nature of the quantum melting transitions is indeed expected, since (as shown below) the incompressible phases break the space group symmetry, whereas in the uniform superfluid $U(1)$ symmetry breaking occurs at $T = 0$.

6.1.1. Quantum Monte Carlo

In order to perform the SSE QMC simulations for the current model, a cluster decomposition of the Hamiltonian in terms of trimers of nearest-neighbor sites is performed, such that each cluster carries one of the three-body interaction terms. The addition of the nearest neighbor two-body repulsions V , proceeds in this decomposition scheme as well, with each two-body term being shared by four such trimers. While the algorithm performed well for large values of the hopping t , it is not feasible reach significantly below $t/W \approx 0.1$ due to the dynamical freezing in the Monte Carlo configurations, once the competing diagonal interaction terms dominate the Hamiltonian (which is a general issue of the SSE for Hamiltonians dominated by large diagonal terms). In terms of the simulation temperature T , it is found that an inverse temperature $\beta = 1/T = 20 - 50W$ ($k_B = 1$) provided an

optimal trade-off between the finite temperature incoherence and the algorithmic performance. Furthermore, in order to be commensurate with all superstructures identified in the incompressible phases, the linear system size L is required to be an integer multiple of 6 (the total number of lattice sites being $N = 2L^2$, as the honeycomb lattice contains two sites per unit cell, forming the two sublattices A and B). Within the above temperature regime, systems up to $L = 24$, in some cases up to $L = 36$ in linear extend are simulated. In phases with large superstructures – described below – it is found that the autocorrelation times of the bosonic structures increase such that the algorithm is not able to tunnel between different realizations of the ordering pattern even within several 10^6 QMC sweeps, but resides in one particular sector of the ground-state manifold (which however varies upon performing independent runs with different random-number streams for a given set of model parameters). During a first stage of the thermalization process, the system is annealed in a cyclic way by heating it up and cooling it down slowly such that it is able to relax globally into one of the equivalent ground-states. A fixed temperature thermalization was then performed in the second stage of the thermalization process. This annealing approach yields better performance than parallel tempering over an extended temperature ranges, since the main interest is in the ground-state phase diagram of the system, where β is large.

Furthermore, quantum parallel tempering in μ or t [203] (cf. Section 2.1.3) is performed at fixed low temperatures in certain regions of the phase diagram, in particular in order to study the quantum phase transitions between neighboring VBS phases. This issue will be discussed in Section 6.1.3. The special analysis of the model in the classical limit (i.e. for $t = 0$) is presented in Section 6.1.4. There, the applicability of the tensor network renormalization group approach for classical systems to the current three-body repulsive model is assessed. In the following Section 6.1.2, the nature of the incompressible phases that appear in Figure 6.2, are discussed in detail and are characterized from in numerical analysis.

6.1.2. Incompressible Phases

The $n = 9/16$ VBS Phase: The first density plateau that is encountered upon filling the lattice has a density $n = 9/16$ and extends between $0 \leq \mu/W \leq 2$ in the classical limit ($t = 0$). It has an potential energy per lattice site (equal to the internal energy for $t = 0$) of $E_{pot}^{(9/16)} = -9/16\mu$, and corresponds to the closest packing of hardcore bosons on the honeycomb lattice without introducing any three-body repulsions. From geometrical considerations in the classical limit, this bosonic structure is obtained by covering the lattice with equilateral triangles with side length $4\sqrt{2}a$ (where a is the distance between two lattice sites), each covering 16 lattice sites. These triangles are filled by nine bosons in a staggered (checkerboard) arrangement in order to obtain the overall filling $9/16$. Neighboring triangles differ in the placement of the checkerboard pattern. This leads to domain walls along the edges of the triangles, where pairs of bosons reside. For $V = 0$, this does however not lead to a potential energy penalty. For an illustration of this structure, see the left panel of Figure 6.4. This structure allows for a denser packing of the particles (and thus a higher filling) than the overall checkerboard state of filling $n = 1/2$, without introducing any three-body energy terms. On every fourth hexagon (such as the hexagons indicated in the left panel of Figure 6.4), six triangles share a common corner. In the classical limit, the energy of the system remains unchanged, if two particles change their positions along such a hexagon by an angle of $2\pi/6$, as indicated in Figure 6.4. This local move results in a classical ground state degeneracy $W = 3^{N/32}$. Thus, the ground state entropy is extensive, and the entropy per site is $S/N = (\ln W)/N = \log(3)/32 \approx 0.034$ in the thermodynamic limit.

For finite values of t , the local moves allowed in the classical configurations lead to resonances on the hexagonal plaquettes, corresponding to second-order hopping processes of the bosons, effectively rotating a hexagon by an angle of $2\pi/3$, as illustrated in the right panel of Figure 6.4. The system is able this way to gain kinetic energy from these tunneling processes. Such resonances also provide the dominant quantum fluctuations on this density plateau, and stabilize a VBS phase with a superstructure of checkerboarded triangles, linked by the resonating hexagons. Through an order-by-disorder effect, the quantum dynamics thus selects the ground-state to be a coherent superposition of the local

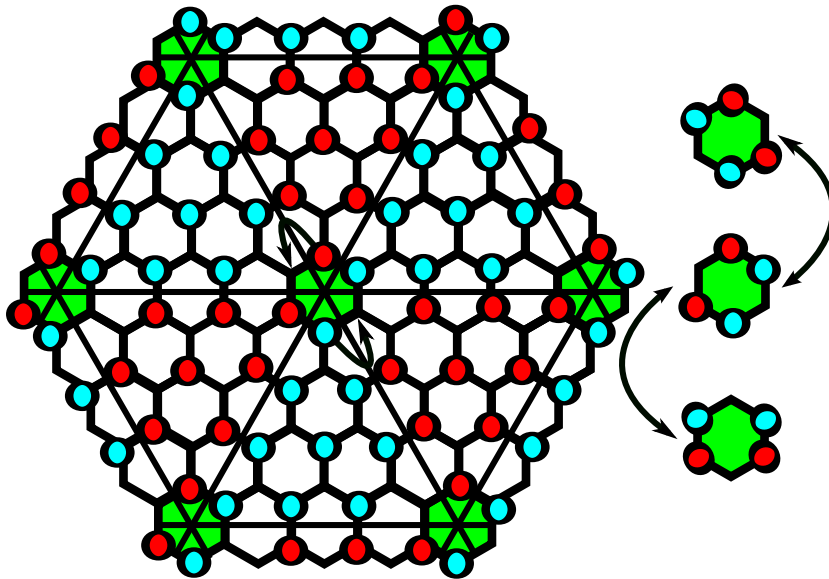


Figure 6.4.: Illustration of the classical configuration in the $n = 9/16$ plateau (left panel). The bosons are shown in two different colors, in order to underline the different checkerboard patterns within neighboring triangles. The green hexagons illustrate those plaquettes, where the bosons are allowed to change positions as illustrated in the right panel, without changing the potential energy. For finite hopping $t > 0$, this leads to resonances within these hexagonal plaquettes (right panel).

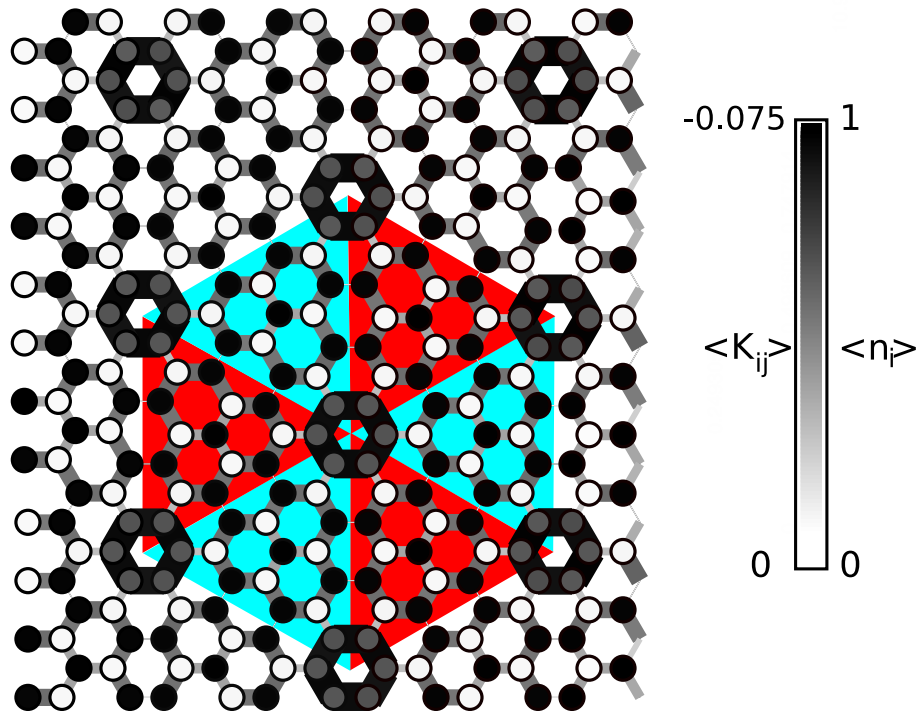


Figure 6.5.: QMC data of the local density $\langle n_i \rangle$ (shading) and the kinetic energy density along the nearest-neighbor bonds $\langle K_{ij} \rangle$ (line thickness and shading) for bosons on the honeycomb lattice in the $n = 9/16$ VBS phase at $V = 0$, $t/W = 0.2$, $\mu/W = 1$, and a system with $L = 12$ at $\beta = 20$. For clarity, the equilateral triangles, together forming the unit cell of the VBS superstructure, are indicated as well.

resonance states.

The peculiar features of the $9/16$ plateau phase can also be identified from QMC simulations. In Figure 6.5, the local density $\langle n_i \rangle$ is shown, along with the kinetic energy density per bond $\langle K_{ij} \rangle$, where $K_{ij} = b_i^\dagger b_j + b_j^\dagger b_i$ and sites i and j belong to a nearest neighbor bond on the honeycomb lattice, for a representative point within the $n = 9/16$ phase. The local density is found to be close to $\langle n_i \rangle = 1$ and 0 , thus exhibiting only few fluctuations, in a staggered (checkerboard) pattern within triangular structures. On the other hand, the density around a subset of the hexagons – those, where the triangular checkerboard patterns meet – is within an intermediate range, and it is along the bonds of these hexagons, where the kinetic energy is mainly located. Both observations indicate a residual density dynamics in this incompressible phase, located along these hexagons. The resonant nature of the corresponding hopping events

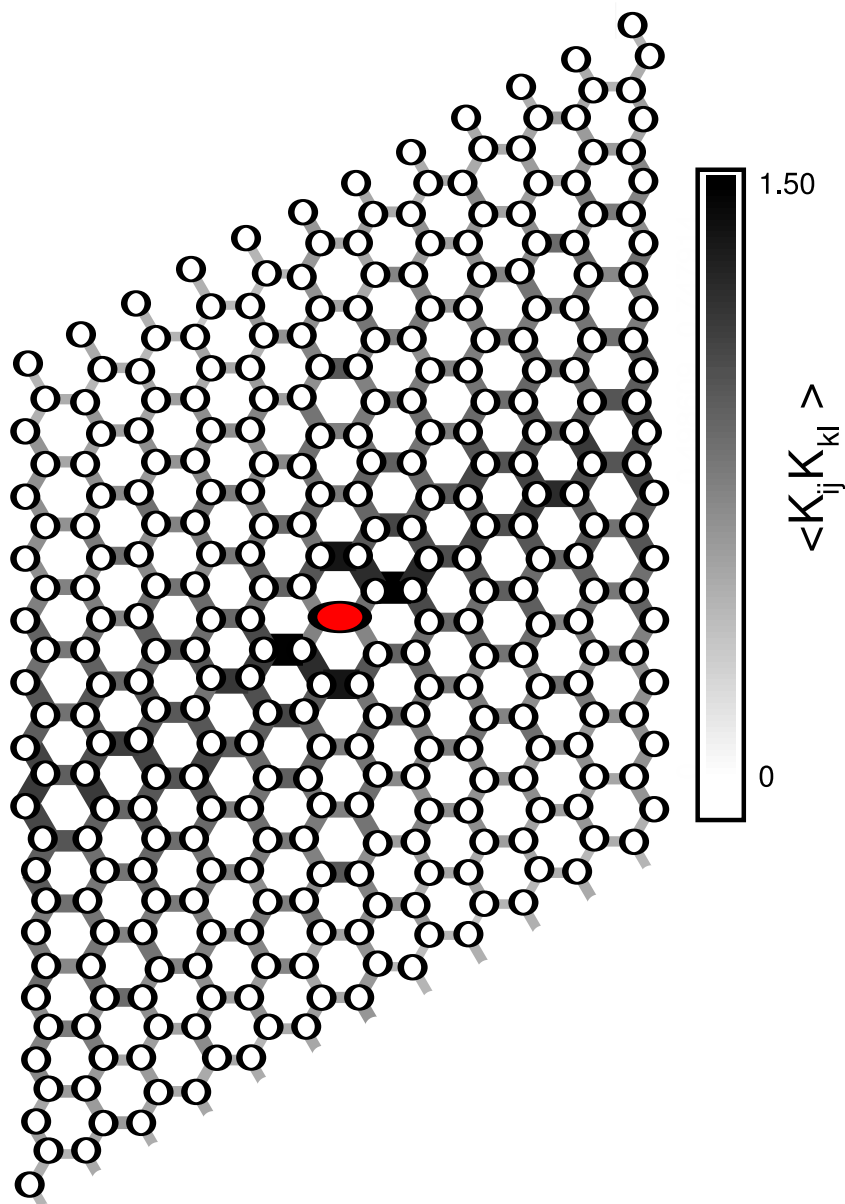


Figure 6.6.: QMC data for the bond-bond correlations in the kinetic energy $\langle K_{ij} K_{kl} \rangle$ along the nearest-neighbor bonds for bosons on the honeycomb lattice in the $n = 9/16$ VBS phase at $V = 0$, $t/W = 0.2$, $\mu/W = 1$, and a system with $L = 12$ at $\beta = 20$. The reference bond $\langle ij \rangle$ is indicated by the red ellipse.

6. Frustrating Three-body Interactions on the Honeycomb Lattice

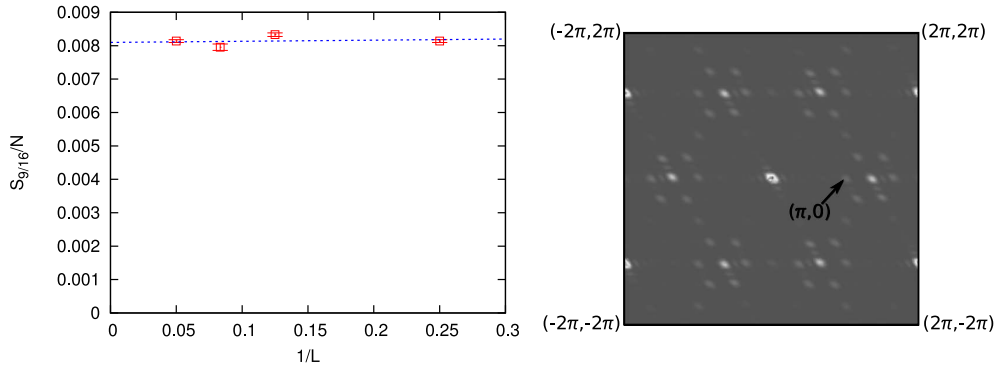


Figure 6.7.: Finite size scaling of the density structure factor $S_{9/16}$ for the $n = 9/16$ phase of hardcore bosons on the honeycomb lattice at $V = 0$, $t/W = 0.1$, and $\mu/W = 1$ (left panel). The right panel shows the positions of the peaks in the density structure factor in momentum space, with the peak at $\mathbf{q}_0 = (\pi, 0)$ indicated by the arrow.

is reflected in the bond-bond correlation function $\langle K_{ij}K_{kl} \rangle$, shown in Figure 6.6. One can identify the main contribution from the hexagonal resonances, which lead to the enhanced bond-bond correlation between the reference bond (marked by an ellipse) and the bonds atop and below the reference bond in Figure 6.6. Furthermore, correlations of the same strength are visible between the reference bond and its next-nearest neighbor bonds to the left and right. These result from residual quantum fluctuations that lead to the finite kinetic energy distribution inside the checkerboarded triangular structures in Figure 6.5. The hexagonal resonances evolve essentially independently of each other and no long ranged bond-bond correlations are observed.

The right panel of Figure 6.7 shows the density structure factor for the $9/16$ VBS structure, $S(\mathbf{q}) = 1/N \sum_{ij} n(\mathbf{x}_i)n(\mathbf{x}_j) e^{i\mathbf{q}(\mathbf{x}_i-\mathbf{x}_j)}$. Here, $n_a(\mathbf{x}_i)$ denotes the local density operator at position \mathbf{x}_i (note, that \mathbf{x}_i denotes the position of the lattice site i , and not the one of the unit cell, to which sites i belongs). A 6-fold structure is identified, with one of the equivalent peaks positioned at $\mathbf{q}_0 = (\pi, 0)$. This structure relates to the superstructure of equilateral triangles and thus provides a characteristic feature in the density distribution of this phase. The left panel of Figure 6.7 shows a finite size scaling analysis of QMC data for the structure factor $S_{9/16} = \langle S(\mathbf{q}_0) \rangle$ at this characteristic wavevector \mathbf{q}_0 for a system within the $9/16$ VBS phase. $S_{9/16}/L^2$ indeed extrapolates in the thermodynamic limit ($N \rightarrow \infty$) to a finite value, verifying the presence of long-range density

order in the bosonic structure of the 9/16 VBS phase.

The $n = 5/8$ VBS Phase: The next density plateau encountered upon further increasing the chemical potential appears between $2 < \mu/W \leq 5$ in the classical limit, and has a filling of $n = 5/8$. The classical potential energy equals $E_{pot}^{(5/8)} = -5/8\mu + W/8$ in this phase. As for the 9/16 plateau, one obtains a VBS structure in the quantum regime. However, its effective description is more involved.

In the classical limit, each valid configuration at this filling can be mapped to a lozenge tiling of the two-dimensional plane. Each lozenge is formed by eight lattice sites, and contains the boson pattern shown in Figure 6.8a, with a trimer-dimer pair such that one three-body vertex is introduced. A boson covering of filling $n = 5/8$ and energy $E_{pot}^{(5/8)}$ results whenever the full area of the lattice is covered with such lozenges. However, one has to introduce a parity constraint in mapping to the boson configuration: coloring the lozenges as shown in Figure 6.8a, only sides of the lozenges of equal color are allowed to touch, in order not to introduce additional three-body repulsions, which would lead to a higher potential energy. Furthermore, it is well known that each lozenge tiling of the plane is dual to a hardcore dimer covering of a honeycomb lattice [297]. This honeycomb lattice consists of hexagons that are a factor of two larger in linear extend than the hexagons of the underlying honeycomb lattice in the bosonic model. Different lozenge tilings along with the corresponding dimer coverings and the underlying boson patterns, are shown in Figure 6.8b and c. This mapping from bosonic configurations to dimer coverings allows to obtain the ground state entropy of the $n = 5/8$ phase in the classical limit from that of closed-packed hardcore dimer coverings on the honeycomb superlattice, which equals $S = 0.108$ [298] (the additional freedom of how the honeycomb superstructure is embedded onto the underlying lattice, and the two possible ways of coloring the lozenges lead to a further, non-extensive factor of 3×2 to the ground state degeneracy). Among the various lozenge tilings the dice lattice is found, shown in Figure 6.8b, which corresponds to a staggered dimer covering on the honeycomb superlattice. Other tilings contain a special group of three lozenges shown in Figure 6.8c. Rotating the bosons along the central hexagon in this structure, as shown in Figure 6.8c, leads to another allowed configuration, with the group

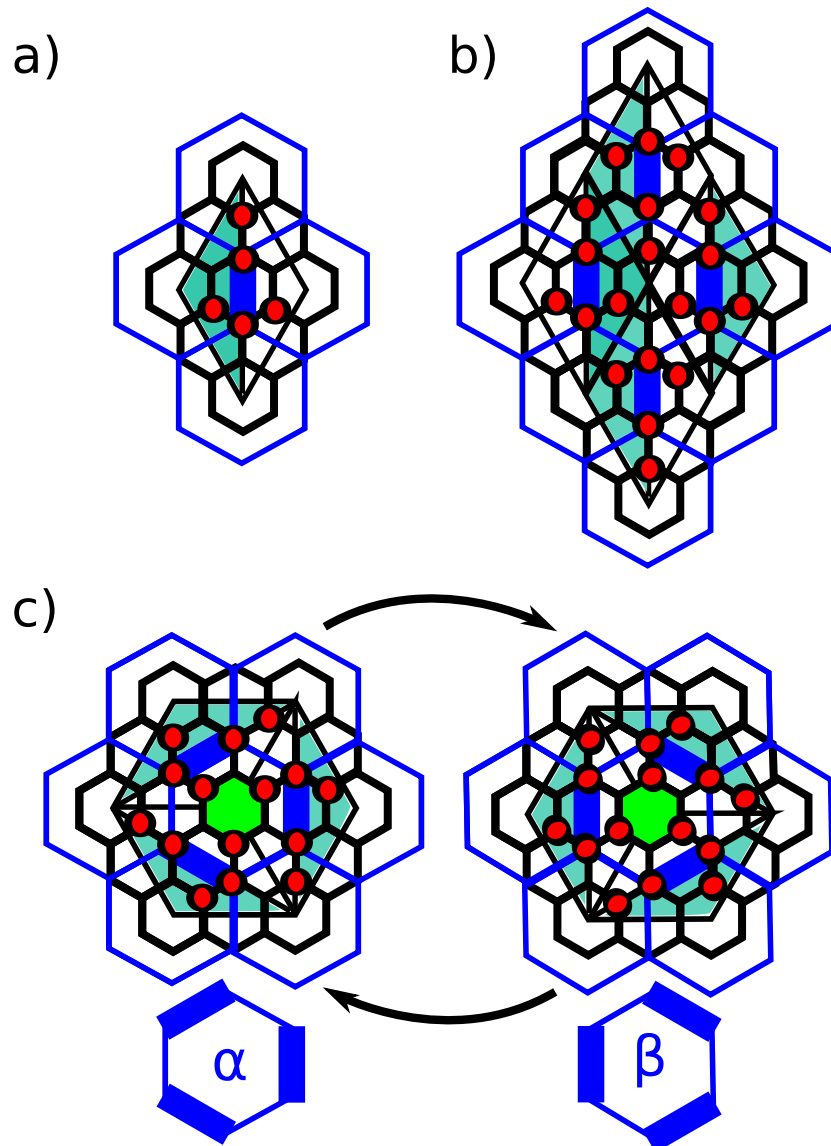


Figure 6.8.: Mapping between allowed boson configurations, lozenge tilings and dimer coverings of a honeycomb lattice: a) shows the colored lozenge with a trimer-dimer pair and part of the honeycomb superlattice. b) shows an example configuration, where the lozenges arrange to form a dice lattice. The corresponding dimer covering on the honeycomb superlattice is indicated as well as the position of the dimers (fat lines). c) shows two configurations that contain a group of three lozenges, where the rotation of the bosons within the central hexagon leads to a flip between the two shown configurations. The notation for the two corresponding states in the quantum dimer model is shown in the bottom row.

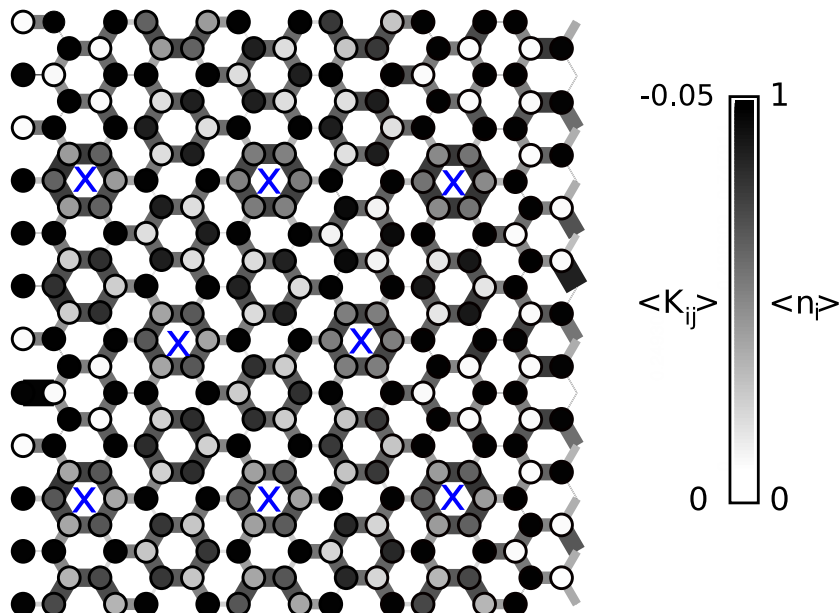


Figure 6.9.: QMC data of the local density $\langle n_i \rangle$ (shading) and the kinetic energy density along the nearest-neighbor bonds $\langle K_{ij} \rangle$ (line thickness and shading) for bosons on the honeycomb lattice in the $n = 5/8$ VBS phase at $V = 0$, $t/W = 0.2$, $\mu/W = 3$, and a system with $L = 12$ at $\beta = 20$. Crosses indicate the most dominant plaquette resonances in this configuration.

of the three lozenges being rotated. In the dimer covering, this leads to a flip of the dimer pattern around the hexagon, as also seen in Figure 6.8c.

Attention is now drawn to the full quantum model, i.e. to the regime $t > 0$. For finite t , a third-order boson hopping process corresponds to this local flip in the dimer configuration on the hexagonal plaquettes of the honeycomb superlattice, as illustrated in Figure 6.8c. Using degenerate perturbation theory in t , this local dimer-flip dynamics is described by a quantum dimer model with solely kinetic terms,

$$H^{\text{QDM}} \propto -t^3/W^2 \sum_p (|\alpha_p\rangle\langle\beta_p| + h.c.), \quad (6.3)$$

and favors the formation of plaquette resonances as shown in Figure 6.8c. Here, $|\alpha_p\rangle$ and $|\beta_p\rangle$ denote the two states on the hexagonal plaquette p on the superlattice in Figure 6.8c involved in the plaquette flip process. This quantum dimer model has been analyzed previously, and the ground state phase diagram was determined using Monte Carlo methods [298]. In particular, for finite values of

6. Frustrating Three-body Interactions on the Honeycomb Lattice

t , the system tries to maximize the number of plaquette resonances. This is possible, if the system forms a dense array of plaquette resonances, i.e. a VBS state formed by plaquette resonances [298]. From this result on the quantum dimer model on the honeycomb lattice [298], the ground state of the bosonic system at filling $n = 5/8$ is found to correspond to the plaquette VBS phase of the quantum dimer model with purely kinetic terms. This phase is characterized by resonances among hexagons, and is reflected in the QMC simulations: to exhibit this, the local density and the kinetic energy density on the nearest neighbor bonds for a representative point within the $n = 5/8$ phase is shown in Figure 6.9. The data is taken at $t/W = 0.2$, outside the asymptotic regime where the perturbative derivation of the effective quantum dimer model strictly holds. Nevertheless, one can identify in Figure 6.9 a pattern that shares the structure of the plaquette VBS phase of the quantum dimer model, as indicated by crosses on the most dominant hexagonal resonances.

The $n = 2/3$ VBS Phase: Further increasing the chemical potential, the classical model exhibits a first-order phase transition at $\mu/W = 5$ from the $n = 5/8$ phase to a $n = 3/4$ density plateau, with potential energy $E_{pot}^{(3/4)} = -3/4\mu + 3/4W$, which (as well as $E_{pot}^{(5/8)}$) equals $-3W$ at $\mu/W = 5$. This point in the phase diagram is highly degenerate; in particular, one finds among the degenerate ground states also states with a filling of $n = 2/3$ and a potential energy $E_{pot}^{(2/3)} = -2/3\mu + 1/3W$ (equal to $-3W$ at $\mu/W = 5$). One particular such state is shown in Figure 6.10. It consists of parallel strips of nearest neighbor boson pairs, separated by zig-zag chains of occupied sites. Other states of the same filling and energy can be obtained from this configuration upon allowing the bosons along the chains segments to move to a neighboring site. One such move is indicated in Figure 6.10. Such processes however are not independent of each other: For example, if the change indicated in Figure 6.10 was made, the two bosons located at the next-nearest neighbors along the chain of the originally occupied site are blocked to perform a similar move, since that would lead to additional three-body repulsion terms, and thus a higher potential energy. These changes in the configuration are thus blocking each other.

From the QMC simulation it is found, that an extended phase of filling $n = 2/3$

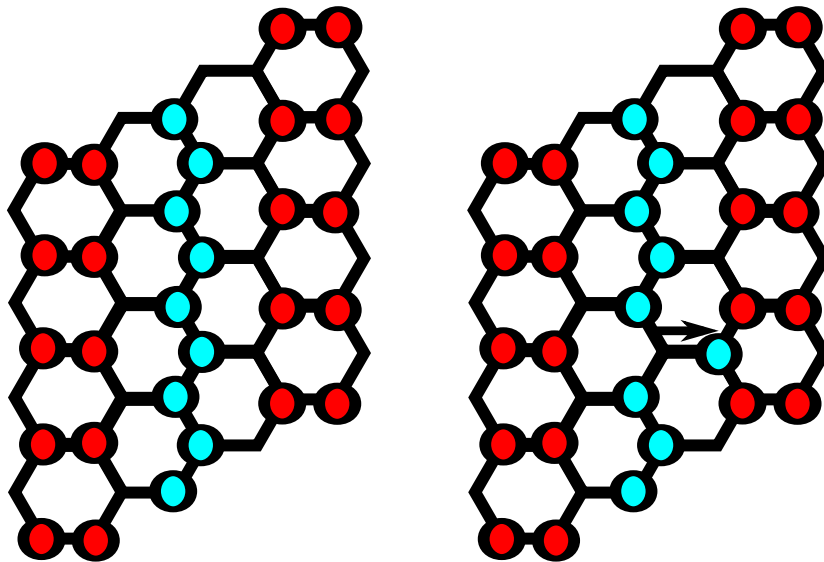


Figure 6.10.: A configurations of bosons on the honeycomb lattice at filling $n = 2/3$, with potential energy $E_{pot} = -3W$ (left panel). Also indicated is one of the processes that leads to further patterns of the same density and potential energy (right panel). In the quantum model, such moves lead to resonances in the emerging $n = 2/3$ phase.

gets selected via an order-by-disorder effect out of the degenerate ground state manifold in the classical limit at $\mu/W = 5$: a new plateau of filling $n = 2/3$ emerges in the quantum phase diagram of Figure 6.2. It vanishes in the classical limit, while upon increasing t , it extends well into the regime $\mu/W < 5$. In order to analyze the nature of this emerging phase, Figure 6.11 shows representative QMC data of the local density and kinetic energy density within the $n = 2/3$ phase. One identifies a rigid backbone of parallel strips of boson pairs, where the local density takes on values close to unity. Furthermore, between these strips one can find sites with a reduced local density, which are linked perpendicular to the stripes' direction by bonds with an enhanced kinetic energy density. Such behavior in both the density and the kinetic energy distribution is in accord with bond resonances, induced by the processes illustrated in Figure 6.10. The opening of the $n = 2/3$ plateau for finite t/W can thus be understood given the large local kinetic energy that the system gains, and which outweighs the penalty in potential energy. Since in the classical limit the kinetic energy contribution vanishes, the potential energy penalty leads to the disappearance of this phase. In Figure 6.12, the bond-bond correlations in the kinetic energy for the $n = 2/3$

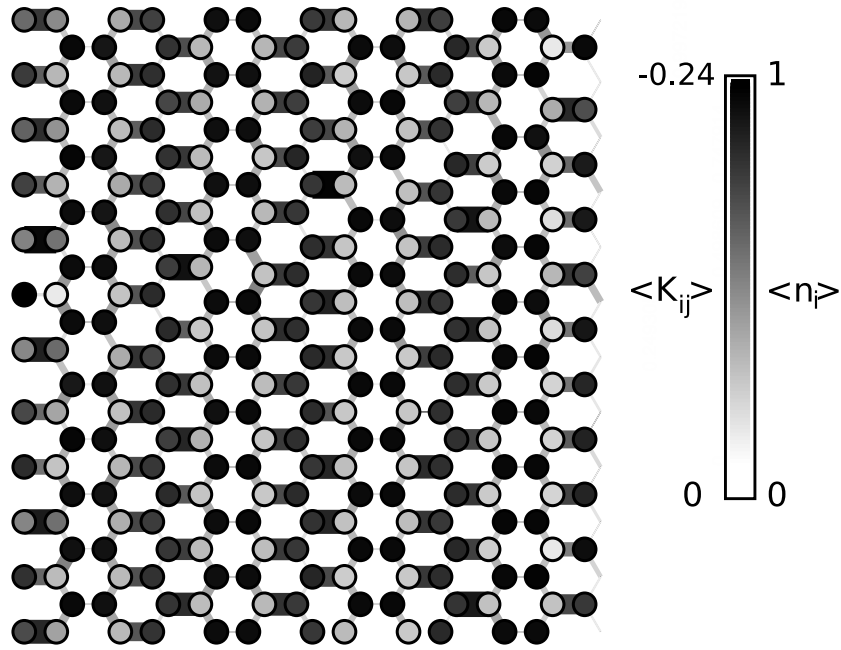


Figure 6.11.: QMC data of the local density $\langle n_i \rangle$ (shading) and the kinetic energy density along the nearest-neighbor bonds $\langle K_{ij} \rangle$ (line thickness and shading) for bosons on the honeycomb lattice in the $n = 2/3$ VBS phase at $V = 0$, $t/W = 0.3$, $\mu/W = 5$, and a system with $L = 12$ at $\beta = 20$.

phase are presented. While the correlations decay quickly in the direction parallel to the strips due to the previously mentioned blocking effect, they sustain over a rather wide range perpendicular to the stripe direction. This underlines the robustness of this emerging $n = 2/3$ phase in the quantum regime.

The $n = 3/4$ Solid Phase: Increasing the chemical potential beyond $\mu/W = 5$, the classical system enters a phase of filling $n = 3/4$, that concludes into the fully occupied state for $\mu/W > 9 + 3t/W$. A particular classical state of this filling and a potential energy of $E_{pot}^{(3/4)} = -3/4\mu + 3/4W$ consists of a regular superlattice of fully occupied hexagons shown in the left panel of Figure 6.13. Additional states of the same filling and potential energy can be constructed by applying *global* moves along parallel lines throughout the system, as shown in Figure 6.13. Such global moves shift all bosons on two parallel lines along one sublattice. The classical ground state entropy of this phase can be calculated by counting the number of states W obtained by such moves. As the number of lines to perform such moves is proportional to the linear system size L , the

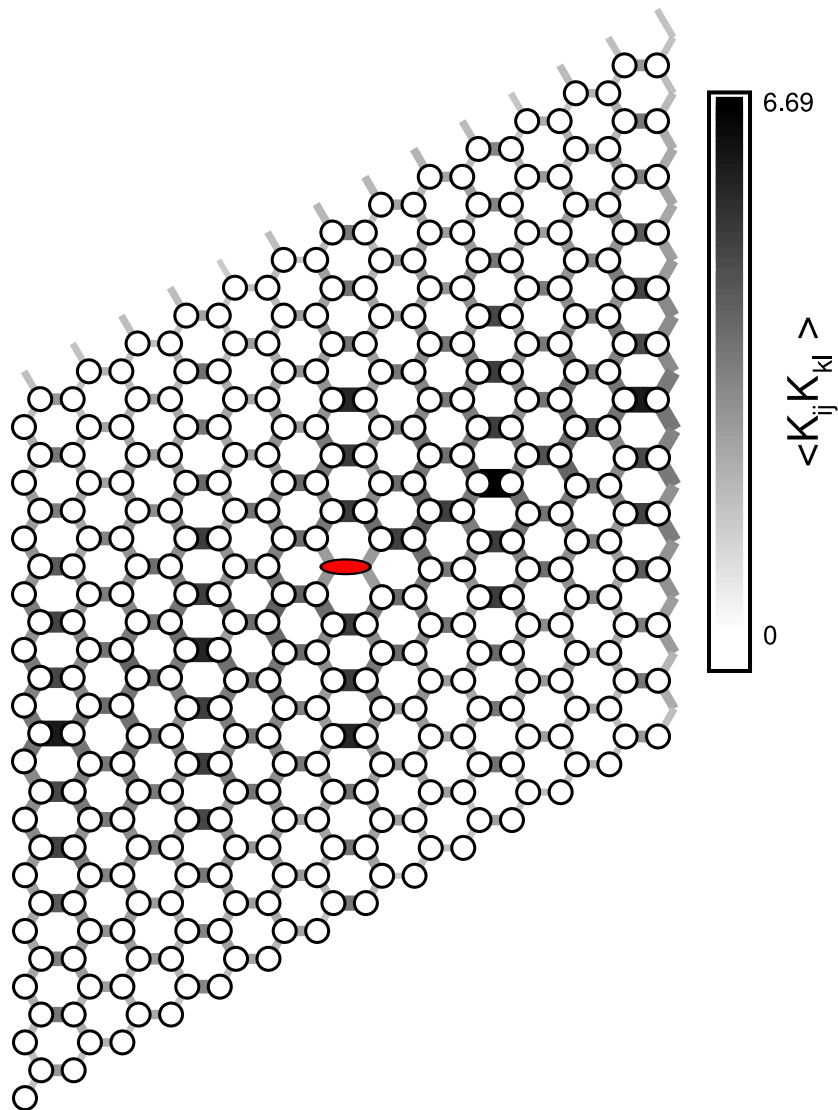


Figure 6.12.: QMC data for the bond-bond correlations in the kinetic energy $\langle K_{ij}K_{kl} \rangle$ along the nearest-neighbor bonds for bosons on the honeycomb lattice in the $n = 2/3$ VBS phase at $V = 0$, $t/W = 0.3$, $\mu/W = 5$, and a system with $L = 12$ at $\beta = 20$. The reference bond $\langle ij \rangle$ is indicated by the red ellipse.

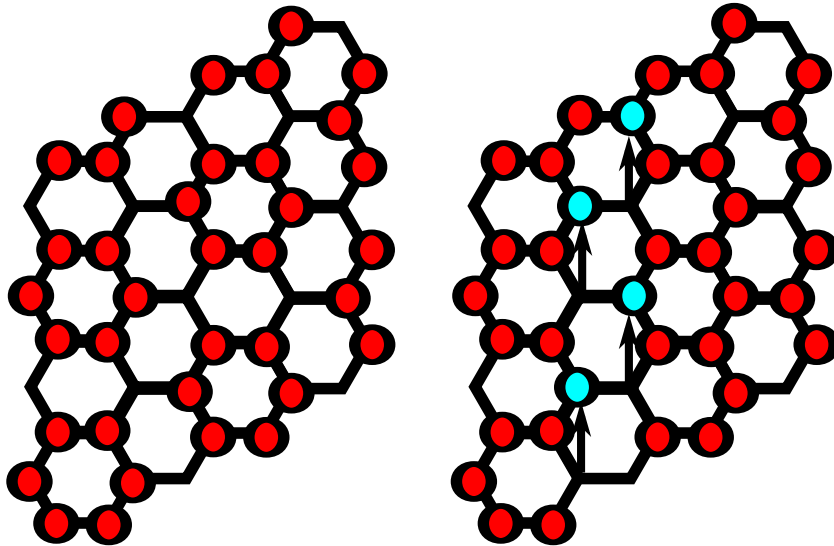


Figure 6.13.: Two classical configurations of filling $n = 3/4$. The state in the left panel consists of a regular superlattice of fully occupied hexagons. To obtain the state in the right panel, the particle colored blue have been shifted upwards (as indicated by arrows) with respect to their original positions in the left panel along two parallel lines.

entropy per sites $S = (\ln W)/(2L^2) \propto 1/L$ scales to zero in the thermodynamic limit.

Because these degenerate ground states are connected not by local moves, but by global displacements, this Boson arrangement will not show resonant structures for finite t . Due to the global nature of the moves that relate the various classical ground states, the QMC algorithm is expected to generate states that are members of this rigid manifold. Indeed, from the QMC simulations, the density patterns that show characteristics of the deformed superlattice of fully occupied hexagons shown in Figure 6.13 are obtained. A representative result from the QMC simulations is shown in Figure 6.14. The classical degeneracy thus appears not to be lifted in the quantum regime.

6.1.3. VBS-VBS Quantum Phase Transitions

After the discussion of the VBS phases appearing in the presence of three-body repulsions on the honeycomb lattice, attention is turned towards the quantum phase transitions between these incompressible phases. An exploration of the transition regions is challenging for the QMC algorithm, because neighboring

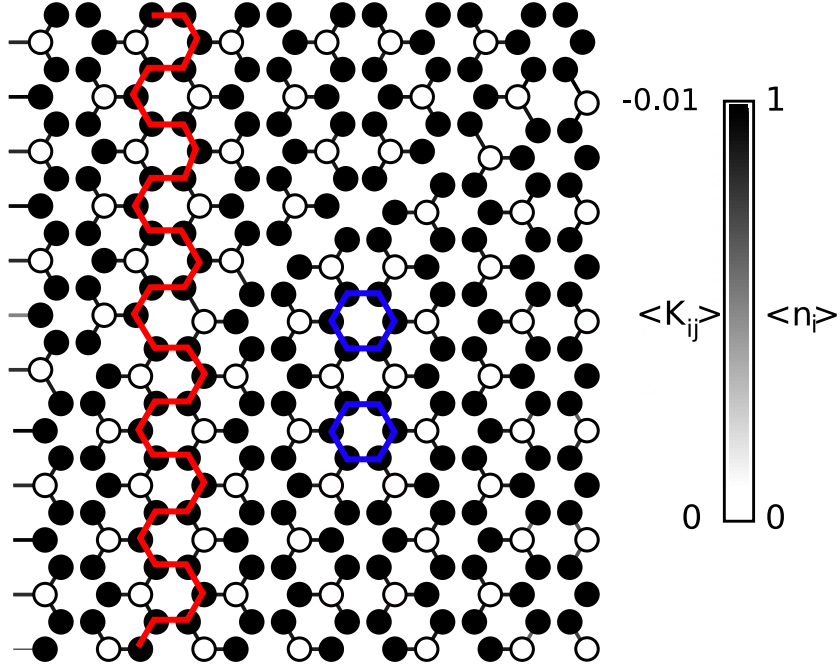


Figure 6.14.: QMC data of the local density $\langle n_i \rangle$ (shading) and the kinetic energy density along the nearest-neighbor bonds $\langle K_{ij} \rangle$ (line shading) for bosons on the honeycomb lattice in the $n = 3/4$ solid phase at $V = 0$, $t/W = 0.3$, $\mu/W = 5$, and a system with $L = 12$ at $\beta = 20$. Two of the fully occupied hexagons observed in this structure are highlighted as well as a chain-like structure like the one in Figure 6.13.

6. Frustrating Three-body Interactions on the Honeycomb Lattice

VBS states are rather close in energy, with competing potential and kinetic contributions of similar size. To illustrate this issue, consider a numerical example of the relevant energy scales. The potential energy difference between the two phases at $9/16$ and $5/8$ filling is $\Delta E_{\text{pot}} = -1/16\mu + 1/8W$, which equals $-0.0625W$ near $\mu/W = 3$. The kinetic energy difference between the two VBS phases for a given value of e.g. $t/W = 0.3$ is obtained from the QMC simulations as $\Delta E_{\text{kin}}(t/W = 0.3) \approx 0.025W$, and is thus of similar size. Competition between these two similar energy scales is found to lead to an extended transition region between the VBS phases, that gives rise to an apparent continuous increase in the density, as seen e.g. in the inset of Figure 6.2. It is checked explicitly that such behavior occurs also for temperatures as slow as $T/W = 0.05$ and $T/W = 0.01$, i.e. well below the above energy scales. Furthermore, strong algorithmic hysteresis effects appear upon varying the chemical potential at fixed t/W through the transition region within a single simulation. Figure 6.15 exemplifies this behavior: Starting within the $n = 5/8$ phase and decreasing μ , the density is stable until reaching $\mu/W \sim 2.1$, where it drops to $n = 9/16$ rapidly. Starting from the $n = 9/16$ phase and increasing μ , the filling of $n = 5/8$ is not established even well inside the $n = 9/16$ VBS region. This behavior exhibits a metastability of the $n = 9/16$ state; the algorithm cannot perform effectively the re-arrangements that are necessary in order to establish the structure of the $n = 5/8$ phase, starting from a configuration typical for the $n = 9/16$ phase.

Quantum parallel tempering in μ/W is employed in order to assess, if with the help of replica-exchanges between neighboring values of μ/W , the algorithm overcomes such metastabilities. Results of these calculations are shown in Figure 6.15 for systems of different sizes for $V = 0$ and $t/W = 0.3$. The obtained density n mimics the behavior of the hysteresis curve. In particular, the range of μ/W over which n increases coincides with the parameter range, where the upper hysteresis curve drops. In addition, the compressibility κ shows a peak within this region, that increases with system size. In the QMC simulations, the compressibility $\kappa = \partial n / \partial \mu = \beta(\langle n^2 \rangle - \langle n \rangle^2)$ is obtained in terms of the density fluctuations. The density curve flattens for the larger values of μ/W , and does not reach $5/8$ even at $\mu/W = 3$. On the other hand, n reaches the value $9/16$ for $\mu/W > 2$. Hence, the replicas are not able to establish the

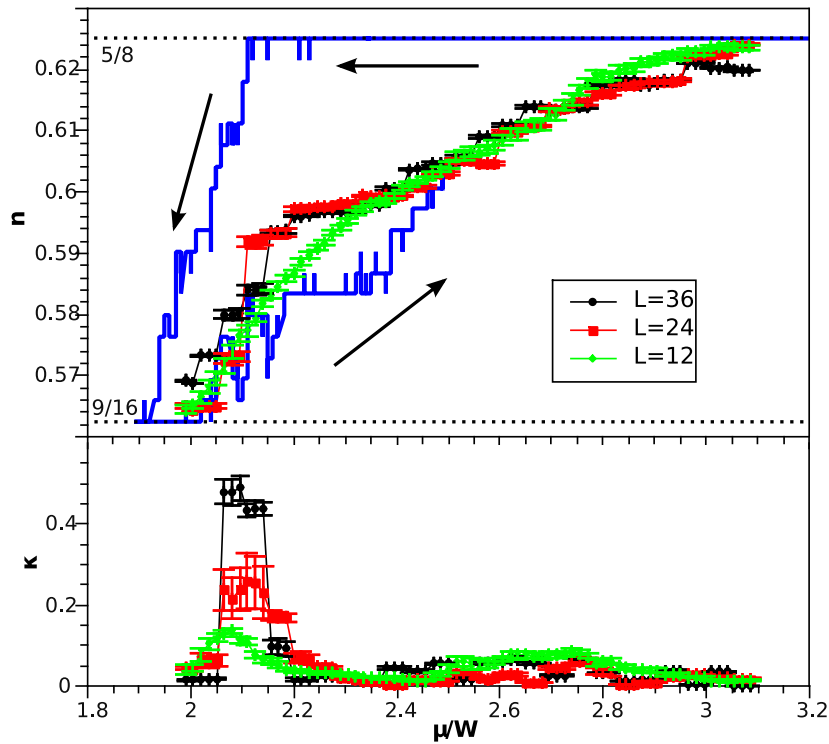


Figure 6.15.: Results of a hysteresis study between the $9/16$ and $5/8$ VBS phases (solid blue line) for a system size $L = 12$, and results from quantum parallel tempering simulations for systems of sizes $L = 12, 24$, and 36 . The upper panel shows the filling n , and the lower panel the compressibility κ obtained from the quantum parallel tempering calculations.

6. Frustrating Three-body Interactions on the Honeycomb Lattice

$n = 5/8$ VBS structure, even though they tunnel repeatedly throughout the extended parameter range. These observations are consistent with a first-order quantum phase transition between the neighboring VBS phases.

However, one might be concerned, that the numerical difficulties could hide an intermediate phase that separates the VBS phases. In one such scenario, an intermediate phase is not commensurate with the considered lattice sizes. When simulating lattices of varying sizes ($L=12, 24, 25, 36$), however, no structures are found to proliferate in the transition regime. Of course, one cannot exclude phases with very large unit cells from our finite size study. Another possibility would be a superfluid or even supersolid phase in the intermediate region, such as observed in a similar model on the square lattice [286]. However, this scenario can be ruled out a finite superfluid density in the transition region: Using quantum parallel tempering in t/W or driving a superfluid system (from large $t/W = 0.5$) towards the transition region at low t , resulted in ρ_s always becoming zero for values of $t/W \lesssim 0.35$. A third possibility for an intermediate phase would be a VBS "emulsion" i.e., a metastable phase mixture with domain walls separating $9/16$ and $5/8$ VBS-like domains. While it is observed that in the QMC simulations bosonic structures that show features of both the $9/16$ and the $5/8$ phase, which would be expected from such an VBS "emulsion" scenario, these structures are also consistent with a first-order transition, given the algorithmic metastability. Thus, a first-order VBS-VBS quantum phase transition is considered to be the most conservative scenario consistent with the QMC data and the apparent difficulty of the QMC algorithm in this parameter regime. Although the precise location of the quantum phase transition can not be determined, the peak position of the compressibility is a good estimate. This is reflected in the phase diagram in Figure 6.2: The points denote the region where the phase transition occurs according to our estimate. The uncertainty of the precise estimate of the transition is integrated in the phase diagram in Figure 6.2 by error bars indicating the smeared out transition region and not the statistical error. The above discussion applies likewise to the other inter-plateau transitions.

6.1.4. Classical Limit

Finite Cluster Studies: In order to analyze the ground state phase diagram of the present model, it is useful to consider also the classical limit $t = 0$ of the quantum Hamiltonian. In the particular case $V = 0$, the model reduces to the most simple classical model on the honeycomb lattice with extended three-body interactions. To the best of the authors knowledge, no previous numerical or even exact results on this statistical physics model have been obtained before. While one can construct states that appear in the classical limit from analyzing boson configurations from the QMC simulations, the implications for the classical limit are also accessed by independent methods. For this purpose, the classical model on a finite hexagonal cluster of linear system size $L = 4$ is solved exactly. Doing so, confirms the extends of the densities plateaus as described above, including the absence of a $n = 2/3$ plateau in the classical limit. However, this system size suffers from the particular problem, that among the various states of the $5/8$ plateau, only the bosonic state corresponding to the dice lattice lozenge tiling (c.f. Figure 6.8b) matches onto this finite cluster. While this particular tiling provides a valid boson covering in the classical limit, this restriction shadows the huge degeneracy of this phase. Namely, on the $L = 4$ cluster, no configuration can be realized, that contains the group of three lozenges shown in Figure 6.8c. In order to be commensurate with such coverings, the linear system size must be an integer multiple of 6. All other phases however are commensurate with this system size, and different boson patterns than those described above for up to 32 sites exactly can be excluded.

In order to check on larger clusters, whether the classical predictions for the bosonic structures are correct, classical Monte Carlo methods are applied. However, they suffer from dynamical freezing at the low temperatures required to explore the plateau structure. In that respect, the QMC simulations perform more efficient, and are thus used the QMC simulations in order to generate configurations of the classical model (this is possible within the SSE framework since on each propagation level one obtains a configuration of the classical model). While the sampling of the classical configurations does not resemble the correct statistical weight, one can nevertheless check if the various classical configuration obtained this way are consistent with our effective descriptions. In particular,

it is verified that each classical configuration of density $n = 5/8$ and potential energy $E_{pot} = E_{pot}^{(5/8)}$ indeed complies with the construction given in Section 6.1.2 in terms of lozenge tilings. No classical configuration with the right density and potential energy, that would violate this construction, is observed indicating that the understanding of the classical phases is in deed correct.

Tensor Network Renormalization Group: Recently, an interesting novel approach to study thermodynamic properties of classical statistical models has been proposed [217]. It is based on a tensor network representation of the partition function Z , and evaluates it directly in the thermodynamic limit using a real space renormalization procedure in the tensor network decomposition, as discussed in detail in Section 2.2.

Its applicability is demonstrated by recent works applying this approach to the Ising-model on the triangular [217, 219] and the Shastry-Sutherland lattice [220] encouraging the application to the honeycomb model with two- and three-body interactions considered in this chapter. In fact, in the original publication [217], the method was described explicitly for tensor network models on the honeycomb lattice. It is found, that one can indeed express the partition function of our model in terms of a tensor network. For this purpose, one specifies two cyclically symmetric tensors T_{ijk}^A and T_{ijk}^B , with indices i, j, k running from 1 up to a finite integer D , where each index corresponds to a degree of freedom $i = 1, \dots, D$ on the bonds of the honeycomb lattice. One verifies easily, that with the particular tensors, given in Table 6.1.4, Z indeed recovers the partition function of the classical particle model (cf. Equation (2.33)). Once a representation of the classical model in terms of a tensor network has been obtained, one can proceed to perform the renormalization procedure to this tensor network. Doing so, involves an approximation, since within each renormalization step the dimension of the renormalized tensor network is truncated to a fixed maximum dimension $D_{max} > D$. D_{max} is thus a regularization parameter of the algorithm. From the approximatively evaluated partition function, one obtains the free energy $f = -\frac{T}{N} \ln(Z)$ in the thermodynamic limit, from with the density n is calculated by taking numerical derivatives of f with respect to μ . Doing so for sufficiently low temperatures T , the low- T phase diagram is ob-

i	j	k	T_{ijk}^A	T_{ijk}^B
1	1	1	1	1
1	2	2	1	0
1	1	3	0	1
2	2	2	0	$\exp(\beta\mu)$
3	3	3	$\exp(\beta\mu)$	0
2	2	1	1	0
3	3	1	0	1
3	3	4	$\exp(-\beta(-\mu + V/2))$	0
2	2	4	0	$\exp(-\beta(-\mu + V/2))$
3	4	4	$\exp(-\beta(-\mu + V + W))$	0
4	4	2	0	$\exp(-\beta(-\mu + V + W))$
2	2	2	1	0
3	3	3	0	1
4	4	4	$\exp(-\beta(-\mu + 3/2V + 3W))$	$\exp(-\beta(-\mu + 3/2V + 3W))$

Table 6.1.: Non-zero tensor elements T_{ijk}^A for links i, j, k around a site of sublattice A , and T_{ijk}^B for links i, j, k around a site of sublattice B , respectively. All other finite tensor elements are obtained from the shown ones via cyclic permutation of the indices i, j, k .

tained from resolving the density plateau structure. For sufficiently large D_{max} , the numerical data eventually converges to the final result. Within the tensor network renormalization procedure, one performs a singular value decomposition of a $(D_{max})^2 \times (D_{max})^2$ matrix of contracted tensors, from which the renormalized tensors are constructed. After each step the tensors have to be normalized such that all tensor elements are smaller or equal to unity to avoid overflows. Since this procedure is iterated many times, one needs to implement all matrix computations using high-precision floating point arithmetics (e.g. the initial non-zero tensor elements differ in about 18 orders of magnitude from for $\mu/W = 2$ and $\beta = 20/W$ at $V = 0$). In Ref. [219], quadruple precision was found appropriate for an Ising model. Using a customized version of LAPACK [299] with 128 bit reals (floating point precision of about 10^{-34}), it is found that for the current model this precision was still not sufficient in the relevant part of the phase diagram. While the method performs for the case of purely two-body interactions (i.e. for $W = 0$), the tensor iteration procedure does not converge for $\beta \gtrsim W$, once W dominates and the chemical potential reaches beyond $\mu/W \approx 1$. (For

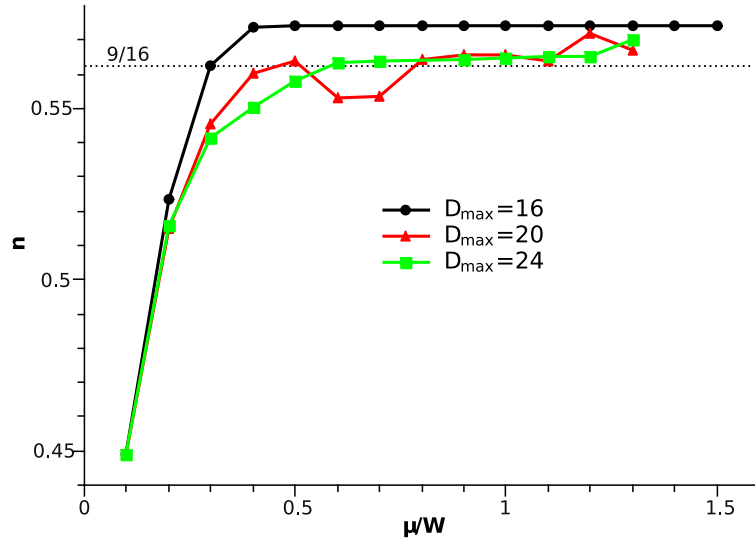


Figure 6.16.: Filling n in the classical limit at $V = 0$, as a function of μ/W obtained from the tensor network renormalization group approach at $\beta = 10$. The curves correspond to different values of D_{max} .

$\beta < W$, the method converged and the results could be verified by comparing to Monte Carlo simulations. However, for such high temperatures, the plateau structure is thermally smoothed out, thus providing no information about the ground state properties.) As an example, Figure 6.16 shows the density curves obtained at $\beta = 10$. In agreement with the previous analysis, the system enters a $n = 9/16$ plateau. However, it is not possible to explore the full phase diagram using this method. The failure of the tensor network renormalization group procedure is traced back to the fact, that the tensors for larger values of μ/W span many orders of magnitude due to the exponential dependence of the Boltzmann factor in the tensor elements. Thus a broad range of values is required in order to account for the physics of the model. However, due to the accumulation of round-off errors in the computation of the renormalized tensor network (which includes a large number of additions and multiplications), one loses the required precision in a numerical implementation of the algorithm after a small number of iteration steps. This problem appears to be a generic drawback of the tensor network renormalization group method, which one suffers from because of the broad range of magnitudes that our system implies in the tensor network representation. For a model with two-body interactions only (i.e. at $W = 0$), the range of values is significantly reduced, and in this case one could indeed recover

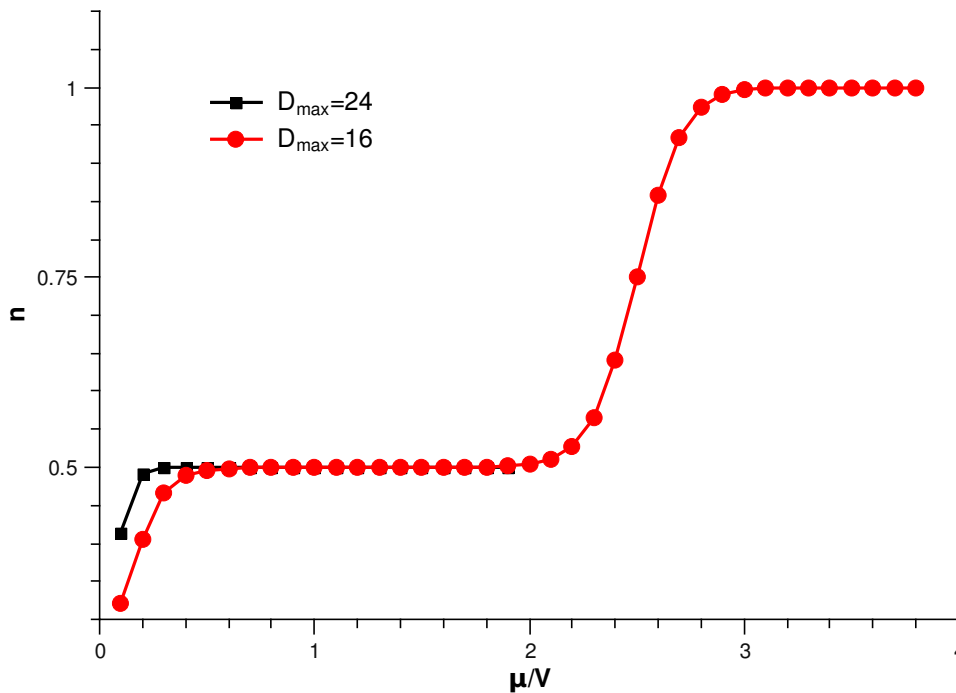


Figure 6.17.: Filling n in the classical limit ($t = 0$) at $W = 0$, as a function of μ/V obtained from the tensor network renormalization group approach at $\beta = 10$. The curves correspond to different values of D_{\max} .

the (well known) behavior of the model, which is equivalent to the ferromagnetic Ising model on the honeycomb lattice. As an example, see Fig. 6.17 showing the filling n as a function of μ/V at $W = 0$ and $\beta/W = 10$, with a pronounced plateau at $n = 1/2$ emerging.

6.2. Two-body Interactions

Thus far, the investigation focused on purely three-body repulsions, and the phases of the bosonic model in that parameter regime is explored. However, from the derivation of the extended Hubbard model for ultra-cold polar molecules in Ref. [142] it is clear, that two-body interactions will be at least of the same strength as the three-body terms². Hence, it is important to assess the influence of two-body terms on the physics of such models. Starting with the

²The claim in Ref. [286], that the interactions are solely of three-body type thus appears in contrast to the results in Ref. [142]

nearest-neighbor three-body term W , the next important interaction term to be considered is the nearest-neighbor two-body repulsion V .

The phase diagram for hardcore bosons with solely nearest-neighbor two-body interactions ($W = 0, V \neq 0$) features a half-filled checkerboard solid for small values of $t/V < 0.5$, surrounded by a superfluid phase, without any supersolid phases present in the quantum phase diagram [80]. In the current setup, the checkerboard solid is recovered at large values of V/W . An important question is, whether the other phases discussed in Section 6.1.2 are stable towards the relevant parameter regime $V \gtrsim W$, and if new phases appear from the competition between two- and three-body interactions.

6.2.1. Cascaded Transition

To make predictions about the impact of two-body interactions, consider the $n = 9/16$ phase in the classical limit. It consists of triangles with an edge length corresponding to the size of four hexagons (c.f. Figure 6.4). No three-body vertices are present in this state, but the structure has neighboring bosons along the edges of the triangles. For finite V , these boson pairs result in a potential energy penalty, which tends to destabilize the structure.

One possibility would be, that there is a direct transition from the $n = 9/16$ phase to the $1/2$ solid upon increasing V/W . However, one can construct intermediate states with densities $1/2 < n < 9/16$, that are energetically preferred for certain ranges of V/W . Such states can be obtained upon generalizing the classical $n = 9/16$ state, where checkerboarded (half-filled) triangles are separated by domain walls: size of these triangular domains is now considered to be variable to vary. Namely, considering honeycomb lattice and covering it with equilateral triangles of edge length x (in units of the size of one hexagon). Each triangle thus covers x^2 lattice sites (Figure 6.20 shows QMC data for the local density that corresponds to a configuration with $x = 12$). A staggered filling with bosons yields a lattice filling of $n_{\Delta}(x) = x(x + 1)/2 - 1$. The boson pairs along the boundaries of the triangles cost an energy of $P_{\Delta} = V(3x - 4)/2$, and the potential energy per lattice site reads

$$E_{\Delta}(x) = -\frac{\mu}{x^2}n_{\Delta}(x) + \frac{1}{x^2}P(x)_{\Delta}V. \quad (6.4)$$

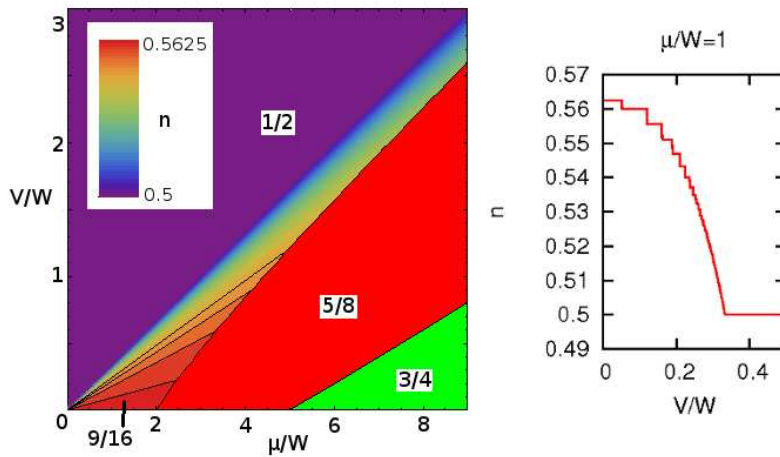


Figure 6.18.: Classical phase diagram for finite V and W in terms of μ/W and V/W (left panel). Colors indicate the filling of the corresponding phases. The $n = 5/8$ and $n = 3/4$ plateaus extend towards finite values of V/W . The color gradient denotes the filling in the cascade, varying from $9/16$ to $1/2$. The phase boundaries of the larger phases are marked by black lines. The right panel shows the filling n as a function of V/W in the classical limit at $\mu/W = 1$.

Minimizing the energy with respect to x gives $x = 4$ for $V = 0$ (the states at filling $9/16$) and $x \rightarrow \infty$ as $V/W \rightarrow \infty$ (convergence to the half-filled checkerboard state). The number of resonances in a system with N sites equals $N/(2x^2)$, resulting in a macroscopic ground state degeneracy of entropy $S/N = \ln(3)/(2x^2)$ for these solid phases.

In order to derive the ground-state phase diagram based on this construction, the energy is minimized for fixed μ/W and V/W as a function of x . For $\mu/W \geq 2$ other competing states are the $n = 5/8$ and for $\mu/W \geq 5$ the $n = 3/4$ phase. Thus, the energy is minimized among these various states in order to determine the phase boundaries. The phase diagram obtained this way is shown in the left panel of in Figure 6.18. In addition to the previously established phases, the system exhibits a cascade of new solid structures (with x running from 4 to infinity) that appear upon increasing the value of V/W . An example the filling as a function of V/W for a fixed value of $\mu/W = 1$ is shown in the right panel of Figure 6.18. Starting from the $n = 9/16$ plateau, a cascade of transitions eventually leads for $V/W > 0.35$ to the staggered plateau of filling $1/2$. This cascade of plateau phases forms an incomplete devil's staircase, induced by the

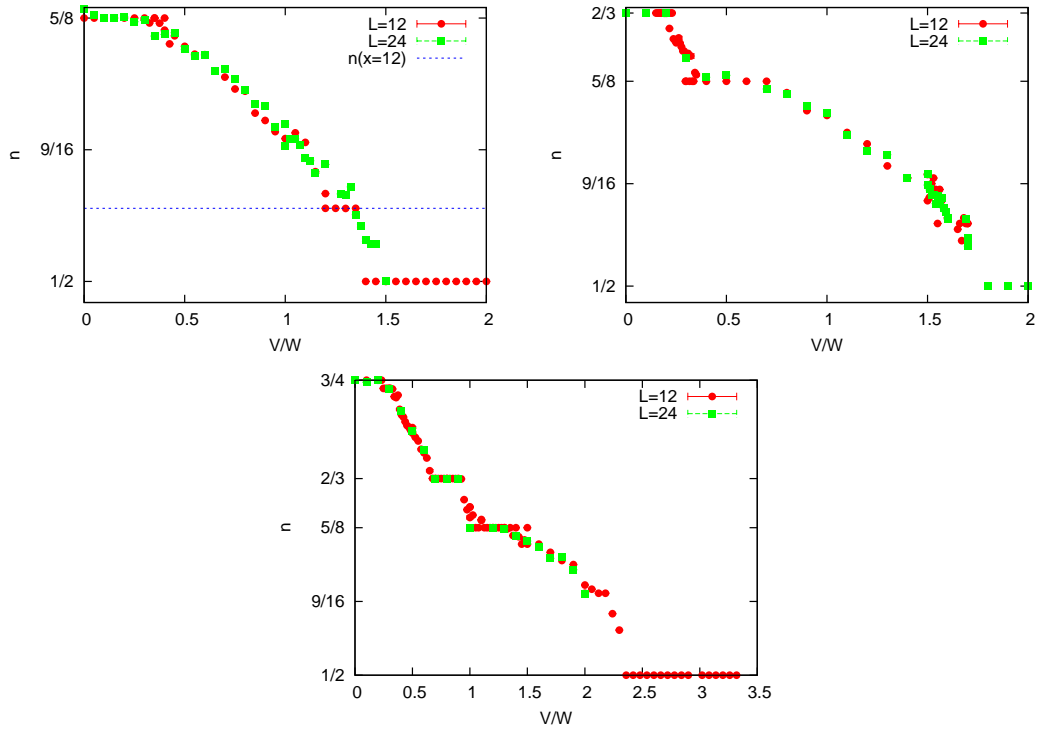


Figure 6.19.: QMC data of the filling n as a function of V/W for $t/W = 0.3$ and $\mu/W = 4, 5$ and 7 (from top to bottom) for $L = 12$ and 24 at $\beta = 20$. **Top:** For $V/W \approx 1.2$ a plateau at $n = 77/144$ (corresponding to $x = 12$) appears, with a direct transition to the half-filled solid at $V/W \approx 1.4$. **Middle:** The $2/3$ density plateau is stable towards finite V/W and decays into the $5/8$ plateau at $V/W \approx 0.3$. **Bottom:** For large enough μ/W one can also see the finite extend of the $3/4$ plateau.

competing nature of the three- and two-body repulsion terms.

6.2.2. Numerical Results

For finite $t > 0$, one expects deviations from the classical cascade structure, since the number of hexagonal resonances that appear for finite t decreases as $1/x^2$ with increasing x . The system could thus skip some of the higher- x plateaus because of the stabilization of the low- x phases by their larger kinetic energy. This can result in entering the staggered phase after only a finite number of intermediate plateaus. Besides, quantum fluctuations stabilize the $n = 2/3$ phase and one has to account for the relevance of this new phase on the overall phase diagram. However, it is difficult to resolve most of the new solid structures

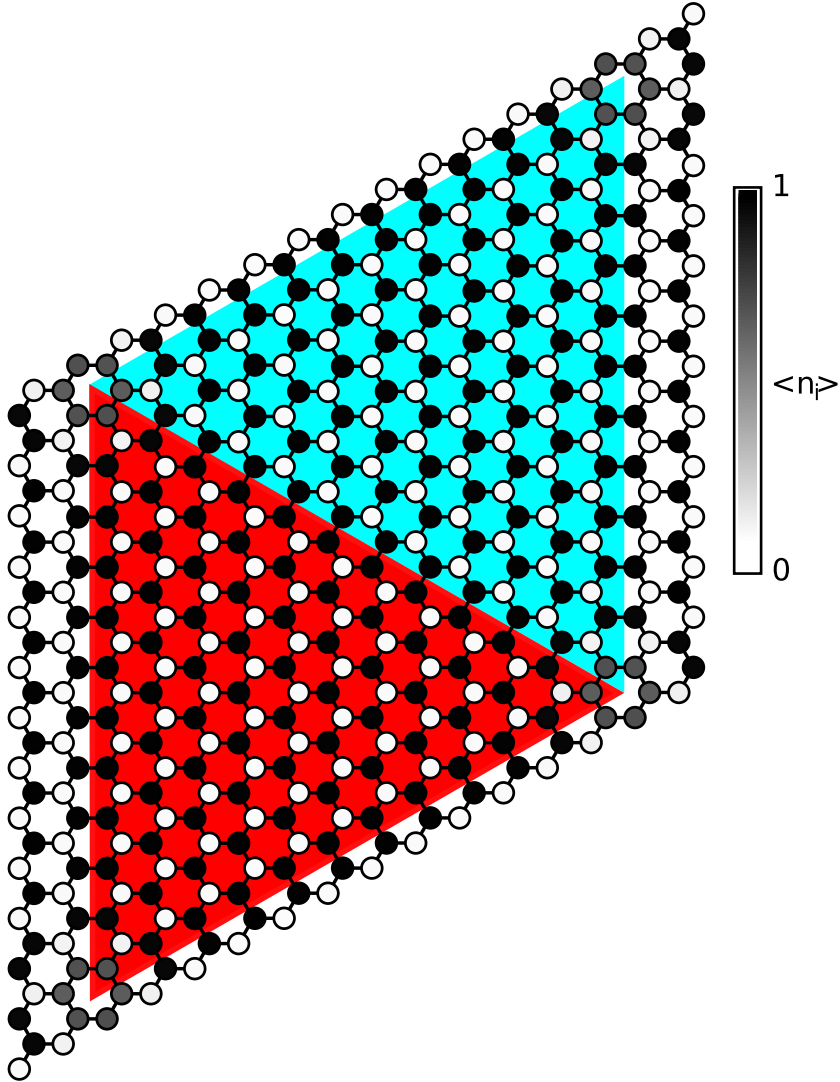


Figure 6.20.: QMC data for the local density $\langle n_i \rangle$ (shading) for $\mu/W = 4$, $t/W = 0.3$ and $V/W = 1.25$. The colored triangles highlight the unit cell of the superstructure with $x = 12$ found in the density plateau at filling $n = 77/144$.

6. Frustrating Three-body Interactions on the Honeycomb Lattice

numerically because they are not commensurate with our lattice sizes. Moreover, the differences in energy and filling for states of neighboring values of x are small, and the plateaus rather narrow already in the classical limit. Nevertheless evidence is obtained from the QMC simulations for (i) a non-direct transition to the staggered solid upon turning on a finite two-body repulsion V , and (ii) the stabilization of new VBS phases. For this purpose, Figure 6.19 shows QMC data for the V -dependence of the filling n for $\mu/W = 4, 5$ and 7 respectively, obtained at $t/W = 0.3$. There one clearly identifies a plateau corresponding to the $x = 12$ structure (of filling $n = 77/144$), commensurate with the lattice sizes of $L = 12$ and 24 . Figure 6.20 shows a representative boson covering obtained by QMC for $\mu/W = 4$ at $V/W = 1.25$, which is in perfect agreement with the $x = 12$ structure introduced above and the formation of hexagonal resonances as in the $n = 5/8$ phase. From Figure 6.19, it is found that the $n = 2/3$ phase is stable for small finite values of $V/W < 0.2$, before a transition takes place towards the $n = 5/8$ density plateau. Similarly, from Figure 6.19, it becomes evident that the $n = 3/4$ phase remains stable for small values of V . At larger values of V/W , one can clearly resolve the $n = 2/3$ and the $n = 5/8$ plateau. While evidence for a cascaded transition to the checkerboard solid is obtained, the employed simulations are not able to fully resolve this transitions within the finite size QMC simulations. Hence, no attempt was tried to comply a full phase diagram for finite V in the quantum case, but the above set of representative cuts through the parameter space are considered. In any case, however, the particular $n = 5/8$ VBS phase can be realized for such realistic values of the ratio between two- and three-body interactions.

7. Outlook and Conclusion

In the last chapter, attention is drawn to open question that arose in the previous chapters and an outlook to further projects, that are still in progress, will be given.

7.1. Open Questions

During the course of this thesis, some issues remain unresolved and give rise to further investigation.

Beginning with the triangular lattice supersolid, that has been discussed in Chapter 4 and 5, the question of the nature of the thermal nucleation at the particle-hole symmetric point seems, in light of the findings of the symmetry enhancement in the quantum transition, not fully understood. In particular, the influence of coupling of the superfluid and solid order parameter and the stability of possible intermediate phases (XY-solid or direct transition?) should be investigated further. In this context, the supersolid-superfluid transition of the bilayer antiferromagnet [76], that is reported to exhibit unexpected Ising critical behavior, and the soft-core supersolid on the square lattice [71], might be revisited with regard to the supersolid nucleation transition.

In Chapter 3, the $t - t'$ Bose-Hubbard model with explicit pair hopping was introduced. The unbinding of halfvortices in the PSF phase at $t' = 0$ gives rise to an enhancement of the critical helicity of factor 4. Looking at the BKT transition for finite t'/t , it is found that Υ_{crit} is not increased by a simple integer but the critical temperature occurs at intermediate values between 1 ($t'/t = 0$) and 4 ($t'/t = 0$). Detailed calculations are currently in progress.

The ansatz used in the quantum parallel tempering studies, for instance in Section 6.1.1, used a naive ansatz for the parameter set $\{\kappa_i\}$. It would appear

useful to check the performance of the optimized schemes discussed in Section 2.1.3 for the case of quantum phase transitions.

7.2. Disordered Supersolid: Towards a Glassy Solid

The properties of the triangular supersolid are discussed thoroughly in Chapter 4 and 5. Its two-component nature makes it an interesting candidate to study the effect of disorder. Previous works by Zhang *et al.* address the influence of static impurities in the triangular supersolid and revealed insight into the coupling of the solid and superfluid components [91]. The question raised here is the influence of random coupling constants. In particular, the chemical potential μ or the hopping amplitude t are distributed randomly, according to fixed probability distributions. The average is performed over a large number of independent disorder realizations, thus, the computational effort, in comparison with a pure system, is raised by a factor of hundred to thousand.

The influence of disorder on the Bose-Hubbard model leads to the appearance of a glassy phase [300] that is compressible, gapless and not superfluid although it has an infinite superfluid susceptibility [301–305]. The stability of the insulating and superfluid phases can be understood by energy arguments, as presented by Imry and Ma [306], and it turns out that a state with broken continuous symmetry is unstable against disorder of its conjugate field in $d \leq 4$ dimensions.

Thus, the supersolid is very sensitive towards a disordered chemical potential, where it seems that DLRO is destroyed instantaneously. In the case of random hopping, the situation is different. Choosing t from a bimodal distribution where t_1 is in the solid and t_2 in the supersolid phase, one can drive the system towards the phase transition with the parameter p denoting the fraction of bonds having $t = t_2$. In particular, the system is solid at $p = 0$ and supersolid at $p = 1$. Preliminary results indicate, that the system becomes compressible before a superfluid response arises. Thus, a peculiar phase is found that shows the characteristics of a glass but exhibits DLRO – this phase might be denoted a glassy solid.

7.3. The N -Flavor Hubbard Model with Alkali Earth Atoms

Recently, the realization of a $SU(N)$ Hubbard model with fermionic alkaline earth atoms has been proposed by Gorshkov *et al.* [307]. The large nuclear spin I can be used to realize $N = 2I + 1$ fermion flavors, where N can be as large as 10 [307, 308]. One remarkable opportunity is the possible realization of a chiral spin liquid, where parity and time reversal symmetry are spontaneously broken, in ladder or two dimensional systems [309, 310].

On the way to the realization of a one dimensional quantum degenerate $SU(N)$ Mott insulator, Hazzard *et al.* point out that the adiabatic ramping procedure from an initial non-interacting gas to the final lattice system gets more effective in terms of final temperatures for large N . The actual calculations involve a high temperature series expansion ($T/t \ll 1$) that is, admittedly, not valid in the Mott regime and the exact cooling effect has as yet not been addressed. The one-dimensional $SU(N)$ Hubbard model reads

$$H = \sum_{\alpha=1}^N \left[-t \sum_{\langle ij \rangle} \left(c_{i,\alpha}^\dagger c_{j,\alpha} + \text{h.c.} \right) + \frac{U}{N-1} \sum_{\beta \neq \alpha} \sum_i n_{i,\alpha} n_{i,\beta} - \mu \sum_i n_{i,\alpha} \right]. \quad (7.1)$$

Here $c_{i,\alpha}^\dagger$ ($c_{i,\alpha}$) creates (annihilates) a fermion of flavor α at site i and $n_{i,\alpha} = c_{i,\alpha}^\dagger c_{i,\alpha}$ counts the fermion occupation at site i . Let $n_\alpha = 1/L \sum_i n_{i,\alpha}$ be the flavor density and $n = 1/L \sum_\alpha \sum_i n_{i,\alpha}$ the total number of fermions. The $T = 0$ phase diagram has been accessed using DMRG [311]. At $n = 1$ ($n_\alpha = 1/N$), the metal-insulator transition is argued to be at $U/t = 0$ for all $N \geq 2$. This result, however, is highly debated, since the gap near the BKT transition closes exponentially and makes an accurate determination of the critical point challenging, on most likely the transition is shifted towards a finite value of U/t . For $n = N$ ($n_\alpha = 1$), however, a dimerized phase for $U/t > 0$ is found to persist.

Accessing the finite temperature physics for fermions is challenging even in one dimension. DMRG, and related finite temperature extensions [312] in particular, suffer from the large local Hilbert space for large values of N . However, the system can be accessed using the directed loop algorithm. The sign problem is

7. Outlook and Conclusion

circumvented in either of two ways. First, one can perform canonical simulations by projecting the measurements onto the subspace of right filling and adjust the boundary conditions (periodic or antiperiodic) accordingly. Second, one can employ open boundary conditions and perform grand-canonical simulations for the price of boundary effects.

The aim of this work is to access the finite temperature physics for large N . Supplementing the high-temperature series expansion [308], the entropy is calculated down to temperatures that are of the order of the superexchange, t^2/U . Within the local density approximation [313], the entropy distribution in the trap can be modeled and the cooling is inferred by the knowledge of the initial temperature and entropy. The goal is to provide an entropy look-up table where one can immediately check whether the spin superexchange regime is accessible for given initial set of parameters. In addition to that, the large- N cooling effect is to be verified.

The vertex decomposition of the Hamiltonian resembles a N -leg ladder of hardcore bosons. Each vertex only contains interactions of two species because the U -term in Equation (7.1) can eventually become very large and suppress off-diagonal events. In this way, simulations for temperature ranges down to $U/(8t^2)$ and $N = 10$ are feasible. Although the entropy can be accessed directly in the SSE framework using quantum Wang-Landau sampling [314], this work resorts to a direct (numerical) integration of $E(T)$ [315].

So far, full LDA calculations for $N = 2, 3$ and 5 have been performed and Figure 7.3 show the filling, energy and entropy for different values of μ/U for a representative parameter set at $N = 3$. In order to get reliable estimate for $S(T)$ at low temperatures, certain numerical difficulties in the numerical integration have to be overcome and extrapolation schemes are employed to improve the accuracy at low T .

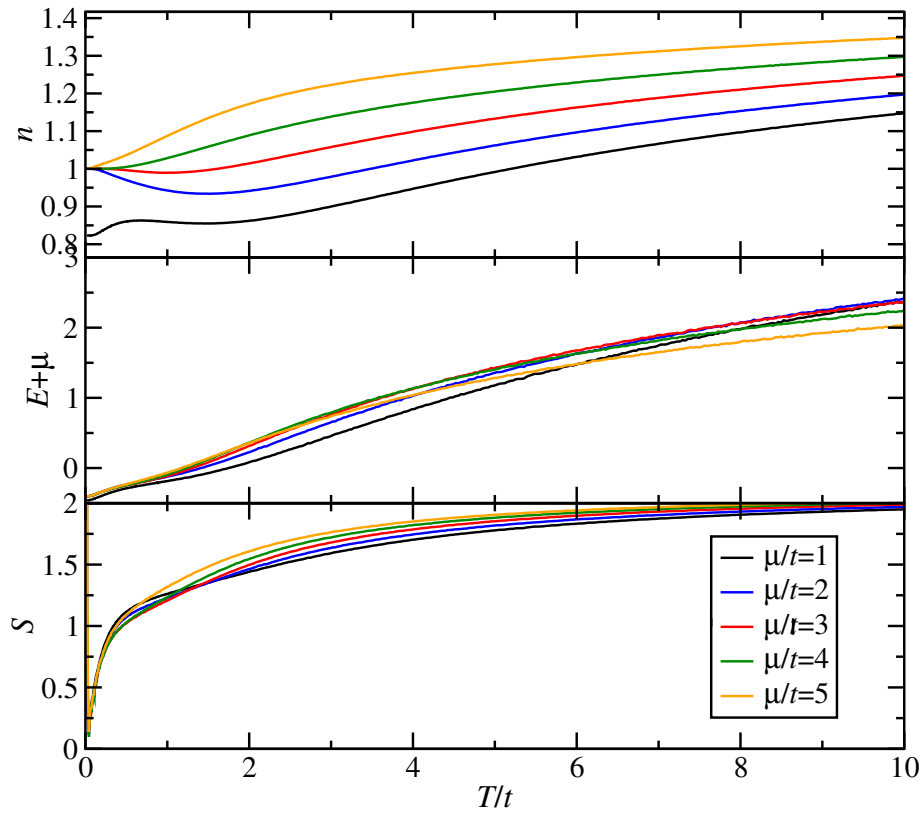


Figure 7.1.: Filling n , energy E and entropy $S = S(T) - S(0)$ for the $N = 3$ Hubbard model at $U/t = 8$ and $L = 42$.

A. Locally Optimal Scattering Probabilities

In this part, the locally optimal scattering probabilities are derived, following the publications by Pollet *et al.* [186, 187].

The transition matrix for Heat-bath updates is given by $P_{l_{\text{in}}, l_{\text{out}}}^{\text{HB}} = \pi_{l_{\text{out}}}$ with

$$\pi_{l_{\text{out}}} = \frac{W_v(l_{\text{in}}, l_{\text{out}})}{\sum_{x=1}^{N_{\text{legs}}} W_v(l_{\text{in}}, l_{\text{out}})}. \quad (\text{A.1})$$

The definition of $W_v(x, y)$ is given in Equation (2.13). Furthermore, let the Heat-Bath matrix elements be ordered such that $\pi_1 \leq \pi_2 \leq \pi_3 \dots$ by a relabeling of the vertex legs. Following the ‘‘Metropolizing’’ scheme from Pollet *et al.* [186, 187], the locally optimal scattering matrices are given as

$$P_{ij}^{\text{Opt}} = \begin{cases} 0 & i = j \text{ and } i \neq N_{\text{legs}} \\ 1 - \sum_{i=1}^{n_{\text{legs}}-1} y_i & i = j = N_{\text{legs}} \\ y_j & i < j \\ \frac{W_j}{W_i} y_i & i > j \end{cases} \quad (\text{A.2})$$

with

$$y_n = \begin{cases} \frac{\pi_1}{1-\pi_1} & n = 1 \\ (1 - \sum_{m=1}^{n-1} y_m) \frac{\pi_n}{1 - \sum_{m=1}^n \pi_m} & n \neq 1 \end{cases} \quad (\text{A.3})$$

Note that since $\sum_{i=1}^{n_{\text{legs}}} \pi_i = 1$, one can rewrite the denominator in the definitions of y_n : $1 - \sum_{m=1}^n \pi_m = \sum_{n+1}^{n_{\text{legs}}} \pi_m$.

B. Helicity Modulus for the Pairsuperfluid

Let Φ be the phase twist across the boundary in the x direction. The Hamiltonian for a twist in x -direction reads

$$H(\phi) = -t \sum_a \left[b_a^\dagger b_{a+\hat{x}} e^{i\phi} + b_{a+\hat{x}}^\dagger b_a e^{-i\phi} \right] - t' \sum_a \left[(b_a^\dagger)^2 (b_{a+\hat{x}})^2 e^{2i\phi} + (b_{a+\hat{x}}^\dagger)^2 (b_a)^2 e^{-2i\phi} \right] + H_y, \quad (\text{B.1})$$

where $\phi = \Phi/L$ is the local phase shift between two lattice sites. Diagonal terms involving only n_i are dropped since the phase shift has no effect. The helicity modulus can be calculated by considering the response of the system towards twisted boundary conditions [175],

$$\Upsilon = \frac{1}{L^2} \frac{\partial^2 F[\phi]}{\partial \phi^2}, \quad (\text{B.2})$$

where $F[\phi]$ is the free energy with respect to the twisted Hamiltonian. The atomic and dimer kinetic term are abbreviated as $H_{\text{kin}}^t = -t \sum_a \left[b_a^\dagger b_{a+\hat{x}} + b_{a+\hat{x}}^\dagger b_a \right]$ and $H_{\text{kin}}^{t'} = -t' \sum_a \left[(b_a^\dagger)^2 (b_{a+\hat{x}})^2 + (b_{a+\hat{x}}^\dagger)^2 (b_a)^2 \right]$. Expanding Equation (B.1) to second order in ϕ gives

$$H(\phi) = H(\phi = 0) - \phi J - \phi^2/2 (H_{\text{kin}}^t + 4H_{\text{kin}}^{t'}) \quad (\text{B.3})$$

where the total current is given as $J = J_1 + J_2$, $J_1 = -it \sum_a \left[b_a^\dagger b_{a+\hat{x}} - b_{a+\hat{x}}^\dagger b_a \right]$ and $J_2 = -2it' \sum_a \left[(b_a^\dagger)^2 (b_{a+\hat{x}})^2 - (b_{a+\hat{x}}^\dagger)^2 (b_a)^2 \right]$.

The derivative of the free energy gives the general Kubo formula [175, 316]

$$\Upsilon L^2 = -\langle H_{\text{kin}}^t + 4H_{\text{kin}}^{t'} \rangle - \int_0^\beta d\tau \langle J(0)J(\tau) \rangle. \quad (\text{B.4})$$

The first part is the expectation value of the kinetic energy and can be directly replaced by the SSE estimator $-1/\beta\langle N^t + 4N^{t'} \rangle$. The current-current correlator has three contributions reading

$$\begin{aligned} & \beta \int_0^\beta d\tau \langle J_1(0) J_1(\tau) \rangle \\ &= - \left(\sum_{ab} \langle [N_a^{t,+} - N_a^{t,-}] [N_b^{t,+} - N_b^{t,-}] \rangle - \delta_{ab} \langle N_a^{t,+} + N_a^{t,-} \rangle \right) \quad (\text{B.5}) \end{aligned}$$

$$\begin{aligned} & \beta \int_0^\beta d\tau \langle J_2(0) J_2(\tau) \rangle \\ &= -4 \left(\sum_{ab} \langle [N_a^{t',+} - N_a^{t',-}] [N_b^{t',+} - N_b^{t',-}] \rangle - \delta_{ab} \langle N_a^{t',+} + N_a^{t',-} \rangle \right) \quad (\text{B.6}) \end{aligned}$$

$$\beta \int_0^\beta d\tau \langle J_1(0) J_2(\tau) \rangle = -2 \left(\sum_{ab} \langle [N_a^{t',+} - N_a^{t',-}] [N_b^{t,+} - N_b^{t,-}] \rangle \right). \quad (\text{B.7})$$

Here $N_a^{t,+}$ counts the number of atomic hopping events on bond $a, a + \hat{x}$ in the positive x direction and $N_a^{t,-}$ in the negative direction. The Kronecker delta terms in Equation (B.5) and Equation (B.6) cancel the kinetic energy in Equation (B.4).

Defining the winding numbers W^t and $W^{t'}$ ($W^i = 1/L \sum_a \langle N_a^{i,+} - N_a^{i,-} \rangle$) for atoms and pairs and considering the response to a phase shift in y direction, one directly obtains the estimator for the helicity modulus

$$\Upsilon = \frac{T}{2} \langle (W^t + 2W^{t'})^2 \rangle. \quad (\text{B.8})$$

C. Implementation of LoadLeveller

The computational effort required in the projects of this theses greatly exceed the capabilities of recent desktop computers that already feature four or more computer cores. High-performance supercomputers are required to fit the needs of extensive numerical studies and the actual computations are performed in a multitude of different system environments such as Beowulf clusters which basically are small computer clusters composed out of “off the box“ PC components, to massively parallel supercomputers like the BlueGene/P. Hence, portability of the program code is important. The generic structure of the execution of a Monte Carlo program, that can be decided in a few generic steps, is predestined for a generic implementation. During the time of this theses, a small, portable and flexible load balancing class was implemented in C++ that meets the needs of every-day work (Quantum) Monte Carlo. It provides a framework for the actual implementation of a specific algorithm where the load balancing on the computer cluster, checkpointing and restarting and data collection and analysis (Bootstrapping, Jackknifing) is performed by the `loadleveller` that provides a simple interface the Monte Carlo class has to provide. This piece of software is by no means designed as a competitor of the ALPS project [317] which provides a toolbox for the simulation of strongly correlated systems including a multitude of algorithms like quantum Monte Carlo, DMRG or TEBD. The project was rather started by the wish to have a minimalistic and transparent framework and is in some parts based on the program code developed during the diploma theses of the author.

Since the parallelization of the Monte Carlo procedure in terms for farming is trivial, as detailed also in Section 3.5, it consists of a number of `tasks` the simulation has to perform. This can be different kind of simulation parameters or system realizations. An example of a `taskfile` looks like

C. Implementation of LoadLeveller

```
walltime = 27000
checkpointtime = 7200
statusfile = status.file
@taskfiles
CFG/L10__t0.045_t20_U-1_mu-0.5__T0.001__N2.config
CFG/L10__t0.05_t20_U-1_mu-0.5__T0.001__N2.config
CFG/L10__t0.055_t20_U-1_mu-0.5__T0.001__N2.config
CFG/L10__t0.06_t20_U-1_mu-0.5__T0.001__N2.config
@taskfiles
```

and the files `CFG/L10__t*_t20_U-1_mu-0.5__T0.001__N2.config` are configuration files including all simulation parameters. All `tasks` will be distributed to the available resources by a `master` that communicates the actual `task` for each node via MPI [318]. After `checkpointtime` seconds all computing nodes report their status to the `master` and checkpointing and, if necessary, redistribution of jobs, is performed. Checkpointing is particularly important since the wallclock times, usually about eight to 24 hours, is smaller than the computation time needed. The implementation of observables is performed via the `measurement` class. The `loadleveller` class accesses the public instance of the `measurement` class provided by the Monte Carlo class. The interface is quite simple; the following example creates a measurement class, adds a scalar and vector observable, adds measurements, makes an error analysis and then saves all measurements.

```
measurements measure;
// add observables
measure.add_observable("energy", bin_size);
measure.add_vectorobservable("G1_x",L,bin_size);

double E;
vector<double> greensfct(L);

... measurement loop
    measure.add("energy", E);
    measure.add("G1_x",greensfct[0]);
...
// get mean of E and error of G1_x
```

```
int mean=measure.mean("E");
valarray errorVector=measure.error("G1_x");

// write to files
measure.write("/somedir/for/measurement")
```

Portability of the code is ensured by minimizing the use of external libraries. The `loadleveller` environment itself, including the checkpointing and effective random number generator based on a Mersenne Twister but also providing wrappers to ACML¹, SPRNG² and BOOST³, only utilizes the C++ standard library and an implementation of MPI, such as LAM MPI⁴, MPICH⁵ or openMPI⁶.

¹AMD Core Math Library, <http://developer.amd.com/libraries/acml/pages/default.aspx>

²The Scalable Parallel Random Number Generators Library <http://sprng.cs.fsu.edu/>

³<http://www.boost.org/>

⁴<http://www.lam-mpi.org/>

⁵<http://www.mcs.anl.gov/research/projects/mpich2/>

⁶<http://www.open-mpi.org/>

Bibliography

- [1] D. J. Wineland, R. E. Drullinger, and F. L. Walls. Radiation-Pressure Cooling of Bound Resonant Absorbers. *Phys. Rev. Lett.*, 40:1639, 1978.
- [2] M. H. Anderson, J. R. Ensher, M. R. Matthews, C. E. Wieman, and E. A. Cornell. Observation of Bose-Einstein Condensation in a Dilute Atomic Vapor. *Science*, 269:198, 1995.
- [3] C. C. Bradley, C. A. Sackett, J. J. Tollett, and R. G. Hulet. Evidence of Bose-Einstein Condensation in an Atomic Gas with Attractive Interactions. *Phys. Rev. Lett.*, 75:1687, 1995.
- [4] K. B. Davis, M.-O. Mewes, M. R. Andrews, N. J. van Druten, D. S. Durfee, D. M. Kurn, and W. Ketterle. Bose-Einstein Condensation in a Gas of Sodium Atoms. *Phys. Rev. Lett.*, 75:3969, 1995.
- [5] http://nobelprize.org/nobel_prizes/physics/laureates/2001/.
- [6] M. R. Andrews, C. G. Townsend, H.-J. Miesner, D. S. Durfee, D. M. Kurn, and W. Ketterle. Observation of Interference Between Two Bose Condensates. *Science*, 275:637, 1997.
- [7] M. Greiner, O. Mandel, T. Esslinger, T.W. Hänsch, and I. Bloch. Quantum phase transition from a superfluid to a Mott insulator in a gas of ultracold atoms. *Nature*, 415:39, 2002.
- [8] T. Udem, R. Holzwarth, and T. W. Hänsch. Optical frequency metrology. *Nature*, 416:233, 2002.
- [9] S. Chu. Cold atoms and quantum control. *Nature*, 416:206, 2002.

- [10] W. Ertmer, E. Rasel, C. Salomon, S. Schiller, G. M. Tino, and L. Cacciapuoti. Cold atoms and precision sensors in space. *Europhysics News*, 39:33, 2008.
- [11] N. Poli, F.-Y. Wang, M. G. Tarallo, A. Alberti, M. Prevedelli, and G. M. Tino. Precision Measurement of Gravity with Cold Atoms in an Optical Lattice and Comparison with a Classical Gravimeter. *Phys. Rev. Lett.*, 106:038501, 2011.
- [12] Y.-W. Lee and M.-F. Yang. Superfluid-Insulator Transitions in Attractive Bose-Hubbard Model with Three-Body Constraint. *Phys. Rev. A*, 81:061604, 2010.
- [13] N. P. Armitage, P. Fournier, and R. L. Greene. Progress and perspectives on electron-doped cuprates. *Rev. Mod. Phys.*, 82:2421, 2010.
- [14] L. Balents. Spin liquids in frustrated magnets. *Nature*, 464:199, 2010.
- [15] M. Lewenstein, A. Sanpera, V. Ahufinger, B. Damski, A. Sende, and U. Senchal. Ultracold atomic gases in optical lattices: mimicking condensed matter physics and beyond. *Adv. Phys.*, 56:243, 2007.
- [16] I. Bloch, J. Dalibard, and W. Zwerger. Many-body physics with ultracold gases. *Rev. Mod. Phys.*, 80:885, 2008.
- [17] Q. Zhou and T.-L. Hochbruck. Signature of Quantum Criticality in the density profiles of cold atom systems. *Phys. Rev. Lett.*, 105:245702, 2010.
- [18] L. Pollet, J. D Picon, H. P. Büchler, and M. Troyer. Criticality in trapped atomic systems. *Phys. Rev. Lett.*, 104:125302, 2010.
- [19] Z.-F. Zhang, R. Dillenschneider, Y. Yu, and S. Eggert. Supersolid phase transitions for hardcore bosons on a triangular lattice. *arXiv:1106.0006*, 2011.
- [20] J. B. Kogut. An introduction to lattice gauge theory and spin systems. *Rev. Mod. Phys.*, 51:659, 1979.

- [21] H. P. Büchler, M. Hermele, S. D. Huber, M. P. A. Fisher, and P. Zoller. Atomic Quantum Simulator for Lattice Gauge Theories and Ring Exchange Models. *Phys. Rev. Lett.*, 95:040402, 2005.
- [22] D. Deutsch. Quantum Theory, the Church-Turing Principle and the Universal Quantum Computer. *Proc. R. Soc. Lond. A* 8, 400:97, 1985.
- [23] C. Nayak, S. H. Simon, A. Stern, M. Freedman, and S. Das Sarma. Non-Abelian anyons and topological quantum computation. *Rev. Mod. Phys.*, 80:1083, 2008.
- [24] M. Saffmann, T. G. Walker, and K. Mølmer. Quantum information with Rydberg atoms. *Rev. Mod. Phys.*, 82:2313, 2010.
- [25] R. Gerritsma, G. Kirchmair, F. Zähringer, E. Solano, R. Blatt, and C. F. Roos. Quantum simulation of the Dirac equation. *Nature*, 463:68, 2010.
- [26] G. J. Bednorz and K. A. Müller. Possible highT_c superconductivity in the BaLaCuO system. *Z. Phys. B*, 64:188, 1986.
- [27] C. J. Foot. *Atomic Physics*. Oxford Univ. Press, 2004.
- [28] R. Grimm, M. Weidemüller, and Y. B. Ovchinnikov. Optical dipole traps for neutral atoms. *Adv. At., Mol., Opt. Phys.*, 42:95, 2000.
- [29] N. Masahura, J. M. Doyle, J. C. Sandberg, D. Kleppner, T. J. Greytak, H. F. Hess, and G. P. Kochanski. Evaporative Cooling of Spin-Polarized Atomic Hydrogen. *Phys. Rev. Lett.*, 61:935, 1988.
- [30] K. B. Davis, M.-O. Mewes, M. A. Joffe, M. R. Andrews, and W. Ketterle. Evaporative Cooling of Sodium Atoms. *Phys. Rev. Lett.*, 74:5202, 1995.
- [31] T. Lahaye, C. Menotti, L. Santos, M. Lewenstein, and T. Pfau. The physics of dipolar bosonic quantum gases. *Rep. Prog. Phys.*, 72:126401, 2009.
- [32] C. Becker, P. Soltan-Panahi, J. Kronjäger, S. Dörscher, K. Bongs, and K. Sengstock. Ultracold quantum gases in triangular optical lattices. *New J. of Phys.*, 12:065025, 2010.

- [33] W. S. Bakr, J.I. Gillen, A. Peng, S. Fölling, and M. Greiner. A quantum gas microscope for detecting single atoms in a Hubbard-regime optical lattice. *Nature*, 462:74, 2009.
- [34] D. Jaksch, C. Bruder, J.I. Cirac, C.W. Gardiner, and P. Zoller. Cold Bosonic Atoms in Optical Lattices. *Phys. Rev. Lett.*, 81:3108, 1998.
- [35] W. Kohn. Analytic Properties of Bloch Waves and Wannier Functions. *Phys. Rev.*, 115:809, 1959.
- [36] H. Feshbach. Unified theory of nuclear reactions. *Ann. Phys.*, 5:357, 1958.
- [37] N. Syassen, D.M. Bauer, M. Lettner, T. Volz, D. Dietze, J.J. Garcia-Ripoll, J. I. Cirac, G. Rempe, and S. Dürr. Strong Dissipation Inhibits Losses and Induces Correlations in Molecular Gases. *Science*, 320:1329, 2008.
- [38] J. J. García-Ripoll, S. Dürr, N. Syassen, D. M. Bauer, M. Lettner, G. Rempe, and J. I. Cirac. Dissipation-induced hard-core boson gas in an optical lattice. *New J. of Phys.*, 11:013053, 2009.
- [39] B. Misra and E. C. G. Sudarshan. The Zeno's Paradox in quantum theory. *J. Math. Phys.*, 18:756, 1977.
- [40] D. Guiulini, E. Joos, C. Kiefer, J. Kupsch, I.-O. Stamatescu, and H. D. Zeh. *Decoherence and the Appearance of a Classical World in Quantum Theory*. Springer, 1996.
- [41] L. Tonks. The Complete Equation of State of One, Two and Three-Dimensional Gases of Hard Elastic Spheres. *Phys. Rev.*, 50:955, 1936.
- [42] M. Girardeau. Relationship between Systems of Impenetrable Bosons and Fermions in One Dimension. *J. Math. Phys.*, 1:516, 1960.
- [43] T. Giamarchi. *Quantum Physics in One Dimension*. Clarendon Press, Oxford, 2004.
- [44] B. Paredes, A. Widera, V. Murg, O. Mandel, S. Fölling, I. Cirac, G. V. Shlyapnikov, T. W. Hänsch, and I. Bloch. Tonks-Girardeau gas of ultracold atoms in an optical lattice. *Nature*, 429:277–281, 2004.

- [45] A. J. Daley, J.M. Taylor, S. Diehl, M. Baranov, and P. Zoller. Atomic Three-Body Loss as a Dynamical Three-Body Interaction. *Phys. Rev. Lett.*, 102:040402, 2009.
- [46] B. Paredes, T. Keilmann, and J. I. Cirac. Pfaffian-like ground state for three-body hard-core bosons in one-dimensional lattices. *Phys. Rev. A*, 75:053611, 2007.
- [47] G. Moore and N. Read. Nonabelions in the fractional quantum hall effect. *Nucl. Phys. B*, 360:362, 1991.
- [48] N. R. Cooper. Exact Ground States of Rotating Bose Gases Close to a Feshbach Resonance. *Phys. Rev. Lett.*, 92:220405, 2004.
- [49] T. Kraemer, M. Mark, P. Waldburger, J. G. Danzl, C. Chin and B. Engeser, A. D. Lange, K. Pilch, A. Jaakkola, H.-C. Nägerl, and R. Grimm. Evidence for Efimov quantum states in an ultracold gas of caesium atoms. *Nature*, 440:315, 2006.
- [50] S. R. White. Density matrix formulation for quantum renormalization groups. *Phys. Rev. Lett.*, 69:2863, 1992.
- [51] I. Peschel, X. Wang, M. Kaulke, and K. Hallberg, editors. *Density Matrix Renormalization - A New Numerical Method in Physics*, Berlin, 1999. Springer Verlag.
- [52] H. Carmichael. *An Open System Approach to Quantum Optics*. Springer-Verlag, 1993.
- [53] M. W. J. Romans, R. A. Duine, S. Sachdev, and H. T. C. Stoof. Quantum Phase Transition in an Atomic Bose Gas with a Feshbach Resonance. *Phys. Rev. Lett.*, 93:020405, 2004.
- [54] L. Radzihovsky, P. B. Weichmann, and J. I. Park. Superfluidity and phase transitions in a resonant Bose gas. *Ann. Phys.*, 323:2376, 2008.
- [55] L. Bonnes and S. Wessel. Pair Superfluidity of Three-Body Constrained Bosons in Two Dimensions. *Phys. Rev. Lett.*, 106:185302, 2011.

- [56] P. Embrechts, C. Klüppelberg, and T. Mikosch. *Modelling Extremal Events*. Springer, 1991.
- [57] S. Sachdev. *Quantum Phase Transitions*. Cambridge University Press, Cambridge, 1999.
- [58] S. Mukerjee, C. Xu, and J. E. Moore. Topological Defects and the Superfluid Transition of the $s=1$ Spinor Condensate in Two Dimensions. *Phys. Rev. Lett.*, 97:120406, 2006.
- [59] N. D. Mermin and H. Wagner. Absence of Ferromagnetism or Antiferromagnetism in One- or Two-Dimensional Isotropic Heisenberg Models. *Phys. Rev. Lett.*, 17:1133, 1966.
- [60] K.-K. Ng and M.-F. Yang. Thermal phase transitions in the attractive extended Bose-Hubbard model with three-body constraint. *Phys. Rev. B*, 83:100511(R), 2011.
- [61] A. J. Leggett. Can a Solid Be "Superfluid"? *Phys. Rev. Lett.*, 25:1543, 1970.
- [62] O. Penrose and L. Onsager. Bose-Einstein Condensation and Liquid Helium. *Phys. Rev.*, 104:576, 1956.
- [63] A. F. Andreev and I. M. Lifshitz. Quantum theory of defects in crystals. *Sov. Phys. JETP*, 29:1107, 1969.
- [64] G. V. Chester. Speculations on Bose-Einstein Condensation and Quantum Crystals. *Phys. Rev. A*, 2:256, 1970.
- [65] E. Kim and M. H. W. Chan. Probable observation of a supersolid helium phase. *Nature*, 427:225, 2004.
- [66] E. Kim and M. H. W. Chan. Observation of Superflow in Solid Helium. *Science*, 305:1941, 2004.
- [67] P. Phillips and V. Balatsky. Cracking the Supersolid. *Science*, 316:5830, 2007.

- [68] M. Boninsegni, N. Prokof'ev, and B. Svistunov. Superglass Phase of ^4He . *Phys. Rev. Lett.*, 96:105301, 2006.
- [69] L. Pollet, M. Boninsegni, A. Kuklov, N. Prokof'ev, B. V. Svistunov, and M. Troyer. The role of defects in Supersolid Helium-4. *Physics Procedia*, 7:80, 2010.
- [70] G. Murthy, D. Arovas, and A. Auerbach. Superfluids and supersolids on frustrated two-dimensional lattices. *Phys. Rev. B*, 55:3104, 1997.
- [71] P. Sengupta, L. P. Pryadko, F. Alet, M. Troyer, and G. Schmid. Supersolids versus Phase Separation in Two-Dimensional Lattice Bosons. *Phys. Rev. Lett.*, 94:207202, 2005.
- [72] S. Wessel and M. Troyer. Supersolid Hard-Core Bosons on the Triangular Lattice. *Phys. Rev. Lett.*, 95:127205, 2005.
- [73] D. Heidarian and K. Damle. Persistent Supersolid Phase of Hard-Core Bosons on the Triangular Lattice. *Phys. Rev. Lett.*, 95:127206, 2005.
- [74] R. G. Melko, A. Paramekanti, A. A. Burkov, A. Vishwanath, D. N. Sheng, and L. Balents. Supersolid Order from Disorder: Hard-Core Bosons on the Triangular Lattice. *Phys. Rev. Lett.*, 95:127207, 2005.
- [75] M. Boninsegni and N. Prokof'ev. Supersolid Phase of Hard-Core Bosons on a Triangular Lattice. *Phys. Rev. Lett.*, 95:237204, 2005.
- [76] N. Laflorencie and F. Mila. Quantum and Thermal Transitions Out of the Supersolid Phase of a 2D Quantum Antiferromagnet. *Phys. Rev. Lett.*, 99:027202, 2007.
- [77] B. Capogrosso-Sansone, S. Wessel, H. P. Büchler, P. Zoller, and G. Pupillo. Phase diagram of one-dimensional hard-core bosons with three-body interactions. *Phys. Rev. B*, 79:020503, 2009.
- [78] L. Bonnes and S. Wessel. Supersolid polar molecules beyond pairwise interactions. *Phys. Rev. B*, 83:134511, 2011.

- [79] D. Jaksch. Solid-state physics: Supersolid simulations. *Nature*, 442:147, 2006.
- [80] S. Wessel. Phase diagram of interacting bosons on the honeycomb lattice. *Phys. Rev. B*, 75:174301, 2007.
- [81] V. W. Scarola and S. Das Sarma. Quantum Phases of the Extended Bose-Hubbard Hamiltonian: Possibility of a Supersolid State of Cold Atoms in Optical Lattices. *Phys. Rev. Lett.*, 95:033003, 2005.
- [82] F. Hébert, G. G. Bartouni, R. T. Scalettar, G. Schmid, M. Troyer, and A. Dorneich. Quantum phase transitions in the two-dimensional hardcore boson model. *Phys. Rev. B*, 65:014513, 2001.
- [83] L. Pollet, J. D. Picon, H. P. Büchler, and M. Troyer. Supersolid phase with cold polar molecules on a triangular lattice. *Phys. Rev. Lett.*, 104:125302, 2010.
- [84] T. Ohgoe and N. Kawashima. Quantum Monte Carlo method for pairing phenomena: Supercounterfluid of two-species Bose gases in optical lattices. *Phys. Rev. A*, 83:023622, 2011.
- [85] K. Baumann, C. Guerlin, F. Brennecke, and T. Esslinger. Dicke quantum phase transition with a superfluid gas in an optical cavity. *Nature*, 464:1301, 2010.
- [86] S. Gopalakrishnan, B. L. Lev, and P. M. Goldbart. Emergent crystallinity and frustration with Bose-Einstein condensates in multimode cavities. *Nature Physics*, 5:845, 2009.
- [87] A. Eckhardt, P. Hauke, P. Soltan-Panahi, C. Becker, K. Sengstock, and M. Lewenstein. Frustrated quantum antiferromagnetism with ultracold bosons in a triangular lattice. *Europhys. Lett.*, 89:10010, 2010.
- [88] A. A. Burkov and L. Balents. Superfluid-insulator transitions on the triangular lattice. *Phys. Rev. B*, 72:134502, 2005.

- [89] S. R. Hassan, L. de Medici, and A.-M. S. Tremblay. Supersolidity, entropy, and frustration: t - t' - V model of hard-core bosons on the triangular lattice. *Phys. Rev. B*, 76:144420, 2007.
- [90] H. C. Jiang, M. Q. Weng, Z. Y. Weng, D. N. Sheng, and L. Balents. Supersolid order of frustrated hard-core bosons in a triangular lattice system. *Phys. Rev. B*, 79:020409(R), 2009.
- [91] X.-F. Zhang, Y. C. Wen, and S. Eggert. Static impurities in a supersolid of interacting hard-core bosons on a triangular lattice. *Phys. Rev. B*, 82:220501(R), 2010.
- [92] L. Bonnes and S. Wessel. Generic First-Order vs. Continuous Quantum Nucleation of Supersolidity. *arXiv:1105.1682*, 2011.
- [93] X. Zhang, C.-L. Hung, S.-K. Tung, N. Gemelke, and C. Chin. Exploring quantum criticality based on ultracold atoms in optical lattices. *New J. of Phys.*, 13:045011, 2011.
- [94] R. Moessner and A. P. Ramirez. Geometrical frustration. *Physics Today*, 59:2426, 2006.
- [95] M. Schick, J. S. Walker, and M. Wortis. Phase diagram of the triangular Ising model: Renormalization-group calculation with application to adsorbed monolayers. *Phys. Rev. B*, 16:2205, 1977.
- [96] K. Wada, T. Tsukada, and T. Ishikawa. Monte Carlo Simulation of a Triangular Ising Lattice. *JPSJ*, 51:1331, 1982.
- [97] K. Wada, H. Takayama, and T. Ishikawa. Monte Carlo simulation of a triangular Ising lattice. *J. Magn. & Magn. Mater.*, 31-34:1043, 1983.
- [98] K. Wada and T. Ishikawa. Monte Carlo Study of a Triangular Ising Lattice. I. *JPSJ*, 52:1774, 1983.
- [99] H. Takayama, K. Matsumoto, H. Kawahara, and K. Wada. Monte Carlo Study of a Triangular Ising Lattice. II. Occurrence of the Kosterlitz-Thouless-Like Phase Transition. *JPSJ*, 52:1983, 1983.

- [100] S. Fujiki, K. Shutoh, Y. Abe, and S. Katsura. Monte Carlo Simulation of the Antiferromagnetic Ising Model on the Triangular Lattice with the First and Second Neighbour Interactions. *JPSJ*, 52:1531, 1983.
- [101] H. A. Kramers and G. H. Wannier. Statistics of the Two-Dimensional Ferromagnet. Part I. *Phys. Rev.*, 60:252, 1941.
- [102] H. A. Kramers and G. H. Wannier. Statistics of the Two-Dimensional Ferromagnet. Part II. *Phys. Rev.*, 60:263, 1941.
- [103] G. H. Wannier. Antiferromagnetism. The Triangular Ising Net. *Phys. Rev.*, 79:357, 1950.
- [104] R. M. F. Houtappel. Order-disorder in hexagonal lattices. *Physica*, 16:425, 1950.
- [105] R. B. Potts. Some generalized order-disorder transformations. *Math. Proc. Camb. Phil. Soc.*, 48:106, 1952.
- [106] G. H. Wannier. Antiferromagnetism. The Triangular Ising Net. *Phys. Rev. B*, 7:5017, 1973.
- [107] Y. Saito and K. Igeta. Antiferromagnetic Ising Model on a Triangular Lattice. *J. Phys. Soc. Jpn.*, 53:3060, 1984.
- [108] S. Alexander and P. Pincus. Phase transitions of some fully frustrated models. *J. Phys. A*, 13:263, 1980.
- [109] E. Domany, M. Schick, J. S. Walker, and R. B. Griffiths. Classification of continuous order-disorder transitions in adsorbed monolayers. *Phys. Rev. B*, 18:2209, 1978.
- [110] S. Elizur, R. B. Pearson, and J. Shigemitsu. Phase structure of discrete Abelian spin and gauge systems. *Phys. Rev. D*, 19:3698, 1979.
- [111] C. J. Hamer and J. B. Kogut. Weak-coupling series and the critical indices of Z_p spin systems in two dimensions. *Phys. Rev. B*, 22:3378, 1980.
- [112] F. Y. Wu. The Potts model. *Rev. Mod. Phys.*, 54:235, 1982.

- [113] B. Nienhuis. Critical Behavior of Two-Dimensional Spin Models and Charge Asymmetry in the Coulomb Gas. *J. Statist. Phys.*, 34:731, 1984.
- [114] D. Blankschtein, M. Ma, A. N. Berker, G. S. Grest, and C. M. Soukoulis. Orderings of a stacked frustrated triangular system in three dimensions. *Phys. Rev. B*, 29:5250, 84.
- [115] S. Miyashita. Nature of the Ordered Phase and the Critical Properties of the Three Dimensional Six-State Clock Model. *JPSJ*, 66:3411, 1997.
- [116] M. Oshikawa. Ordered phase and scaling in Z_n models and the three-state antiferromagnetic Potts model in three dimensions. *Phys. Rev. B*, 61:3430, 2000.
- [117] J. Hove and A. Sudbø. Criticality versus q in the $(2+1)$ -dimensional Z_q clock model. *Phys. Rev. E*, 68:046107, 2003.
- [118] O. Borinsenko, G. Cortese, R. Fiore, M. Gravina, and A. Papa. Critical properties of the two-dimensional $Z(5)$ vector model. *Proceedings of Science (Lattice 2010)*, page 274, 2010.
- [119] W. Stephan and B. W. Southern. Monte Carlo Study of the anisotropic Heisenberg antiferromagnet on the triangular lattice. *Phys. Rev. B*, 61:11514, 2000.
- [120] L. D. Carr, D. DeMille, R. V. Krems, and J. Ye. Cold and ultracold molecules: science, technology and applications. *New J. of Phys.*, 11:1367, 2009.
- [121] G. E. Astrakharchik and Y. E. Lozovik. Super-Tonks-Girardeau regime in trapped one-dimensional dipolar gases. *Phys. Rev. A*, 77:13404, 2008.
- [122] A. Griesmaier, J. Werner, S. Hensler, J. Stuhler, and T. Pfau. Bose-Einstein Condensation of Chromium. *Phys. Rev. Lett.*, 94:160401, 2005.
- [123] S. Müller, J. Metz, T. Koch, B. Fröhlich, A. Griesmaier, and T. Pfau. A purely dipolar quantum gas. *arXiv:0808.3876*, 2008.

- [124] *Pushing the Frontiers of Atomic Physics, Proceedings of the XXI International Conference on Atomic Physics*. World Scientific, 2009.
- [125] P. Köberle and G. Wunner. Phonon instability and self-organized structures in multilayer stacks of confined dipolar Bose-Einstein condensates in optical lattices. *Phys. Rev. Lett.*, 80:063601, 2009.
- [126] P. L. Gould. Cold Molecules Beat the Shakes. *Science*, 322:20, 2008.
- [127] S. Kotochigova, P. S. Julienne, and E. Tiesigna. Ab initio calculation of the KRb dipole moments. *Phys. Rev. A*, 68:022501, 2003.
- [128] J. M. Sage, S. Sainis, T. Bergeman, and D. DeMille. Optical Production of Ultracold Polar Molecules. *Phys. Rev. Lett.*, 94:203001, 2005.
- [129] M. Viteau, A. Chotia, M. Allegrini, N. Bouloufa, O. Dulieu, D. Comparat, and P. Pillet. Optical Pumping and Vibrational Cooling of Molecules. *Science*, 321:232, 2008.
- [130] J. Deiglmayr, A. Grochola, M. Repp, K. Mortlbauer, C. Gluck, J. Lange, O. Dulieu, R. Wester, and M. Weidemüller. Formation of Ultracold Polar Molecules in the Rovibrational Ground State. *Phys. Rev. Lett.*, 101:13304, 2008.
- [131] F. Lang, K. Winkler, C. Strauss, R. Grimm, and J. HeckerDenschlag. Ultracold Triplet Molecules in the Rovibrational Ground State. *Phys. Rev. Lett.*, 101:133005, 2008.
- [132] J. G. Danzl, E. Haller, M. Gustavsson, M. J. Mark, R. Hart, N. Bouloufa, O. Dulieu, H. Ritsch, and H.-C. Nägerl. Quantum Gas of Deeply Bound Ground State Molecules. *Science*, 321:5892, 2008.
- [133] K.-K. Ni, S. Ospelkaus, M. H. G. de Miranda, A. Pe'er, B. Neyenhuis, J. J. Zirbel, S. Kotochigova, P. S. Julienne, D. S. Jin, and J. Ye. A High Phase-Space-Density Gas of Polar Molecules. *Science*, 322:231, 2008.
- [134] K.-K. Ni, S. Ospelkaus, D. Wang, G. Quéméner, B. Neyenhuis, M. H. G. de Miranda, J. L. Bohn, J. Ye, and D. S. Jin. Dipolar collisions of polar molecules in the quantum regime. *Nature*, 464:1324, 2010.

- [135] S. Ospelkaus, K.-K. Ni, G. Quéméner, B. Neyenhuis, D. Wang, M. H. G. de Miranda, J. L. Bohn, J. Ye, and D. S. Jin. Controlling the Hyperfine State of Rovibronic Ground-State Polar Molecules. *Phys. Rev. Lett.*, 104:030402, 2010.
- [136] S. D. Kraft, P. Staantum, J. Lange, L. Vogel, R. Wester, and M. Weidemüller. Formation of ultracold LiCs molecules. *J. Phys. B*, 39:993, 2006.
- [137] J. Deiglmayr, M. Repp, A. Grochola, K. Mörtlbauer, C. Glück, O. Dulieu, J. Lange, R. Wester, and M. Weidemüller. Formation of ultracold dipolar molecules in the lowest vibrational levels by photoassociation. *Faraday Discussions*, 142:335, 2009.
- [138] A. H. Castro Neto, F. Guinea, N. M. R. Peres, K. S. Novoselov, and A. K. Geim. The electronic properties of graphene. *Rev. Mod. Phys.*, 81:109, 2009.
- [139] L. Balents, M. P. A. Fisher, and S. M. Girvin. Fractionalization in an easy-axis Kagome antiferromagnet. *Phys. Rev. B*, 65:224412, 2002.
- [140] M. A. Levin and X.-G. Weng. String-net condensation: A physical mechanism for topological phases. *Phys. Rev. B*, 71:045110, 2005.
- [141] A. Micheli, G. K. Brennen, and P. Zoller. A toolbox for lattice-spin models with polar molecules. *Nature Physics*, 2:341, 2006.
- [142] H. P. Büchler, A. Micheli, and P. Zoller. Three-body interactions with cold polar molecules. *Nature Physics*, 3:726, 2007.
- [143] J. Villain, R. Bidaux, J.-P. Cartin, and R. Conte. Order as an effect of disorder. *J. Phys. France*, 41:1263, 1980.
- [144] L. Bonnes, H. P. Büchler, and S. Wessel. Polar molecules with three-body interactions on the honeycomb lattice. *New J. of Phys.*, 12:053027, 2010.
- [145] A. Altland and B. Simons. *Condensed Matter Field Theory*. Cambridge University Press, 2006.

- [146] E. Altman, E. Demler, and M. D. Lukin. Probing many-body states of ultracold atoms via noise correlations. *Phys. Rev. A*, 70:013603, 2004.
- [147] F. Gerbier, S. Trotzky, S. Fölling, U. Schnorrberger, J. D. Thompson, A. Widera, I. Bloch, L. Pollet, M. Troyer, B. Capogrosso-Sansone, N. V. Prokof'ev, and B. V. Svistunov. Expansion of a quantum gas released from an optical lattice. *Phys. Rev. Lett.*, 101:155303, 2008.
- [148] S. Fölling, F. Gerbier, A. Widera, O. Mandel, T. Gericke, and I. Bloch. Spatial quantum noise interferometry in expanding ultracold atom clouds. *Nature*, 434:481, 2005.
- [149] R. Hanbury Brown and R. Q. Twiss. A Test of a New Type of Stellar Interferometer on Sirius. *Nature*, 178:1046, 1956.
- [150] R. Hanbury Brown and R. Q. Twiss. Interferometry of the Intensity Fluctuations in Light. I. Basic Theory: The Correlation between Photons in Coherent Beams of Radiation. *Proc. R. Soc. Lond. A*, 242:300, 1957.
- [151] R. Hanbury Brown and R. Q. Twiss. Interferometry of the Intensity Fluctuations in Light II. An Experimental Test of the Theory for Partially Coherent Light. *Proc. R. Soc. Lond. A*, 243:291, 1958.
- [152] V. W. Scarola, E. Demler, and S. Das Sarma. Searching for a supersolid in cold-atom optical lattices. *Phys. Rev. A*, 73:051601(R), 2006.
- [153] T. Gericke, P. Würtz, D. Reitz, T. Langen, and H. Ott. High-resolution scanning electron microscopy of an ultracold quantum gas. *Nature Physics*, 4:949, 2008.
- [154] W. S. Bakr, A. Peng, M. E. Tai, R. Ma, J. Simon, J. I. Gillen, S. Fölling, L. Pollet, and M. Greiner. Probing the Superfluid – to – Mott Insulator Transition at the Single-Atom Level. *Science*, 329:547, 2010.
- [155] P. Würtz, T. Langen, T. Gericke, A. Koglbauer, and H. Ott. Experimental Demonstration of Single-Site Addressability in a Two-Dimensional Optical Lattice. *Phys. Rev. Lett.*, 103:080404, 2009.

- [156] T. Stöferle, H. Moritz, C. Schori, M. Köhl, and T. Esslinger. Transition from a Strongly Interacting 1D Superfluid to a Mott Insulator. *Phys. Rev. Lett.*, 92:130403, 2004.
- [157] S. Trotzky, P. Cheinet, S. Fölling, M. Feld, U. Schnorrberger, A. M. Rey, A. Polkovnikov, E. A. Demler, M. D. Lukin, and I. Bloch. Time-Resolved Observation and Control of Superexchange Interactions with Ultracold Atoms in Optical Lattices . *Science*, 319:295, 2008.
- [158] S. Trotzky, Y.-A. Chen, U. Schnorrberger, P. Cheinet, and I. Bloch. Controlling and Detecting Spin Correlations of Ultracold Atoms in Optical Lattices. *Phys. Rev. Lett.*, 105:265303, 2010.
- [159] B. Paredes and I. Bloch. Minimum instances of topological matter in an optical plaquette. *Phys. Rev. A*, 77:023603, 2008.
- [160] Z. Hadzibabic, P. Krüger, M. Cheneau, B. Battelier, and J. Dalibard. Berezinskii-Kosterlitz-Thouless crossover in a trapped atomic gas. *Nature*, 441:1118, 2006.
- [161] D. Hellweg, L. Cacciapuoti, M. Kottke, T. Schulte, K. Sengstock, W. Ertmer, and J. J. Arlt. Measurement of the Spatial Correlation Function of Phase Fluctuating Bose-Einstein Condensates. *Phys. Rev. Lett.*, 91:010406, 2003.
- [162] T. P. Simula and P. B. Blaike. Thermal Activation of Vortex-Antivortex Pairs in Quasi-Two-Dimensional Bose-Einstein Condensates. *Phys. Rev. Lett.*, 96:020404, 2006.
- [163] L. E. Sadler, J. M. Higbie, S. R. Leslie, M. Vengalattore, and S. M. Stamper-Kurn. Spontaneous symmetry breaking in a quenched ferromagnetic spinor Bose-Einstein condensate. *Nature*, 443:312, 2006.
- [164] N. Metropolis, A. Rosenbluth, M. Rosenbluth, A. Teller, and E. Teller. Equation of State Calculations by Fast Computing Machines. *J. Chem. Phys.*, 21:1087, 1953.
- [165] G. Bhanot. The Metropolis algorithm. *Rep. Prog. Phys.*, 51:429, 1988.

- [166] A.M. Johansen. Markov Chain Monte Carlo. *International Encyclopedia of Education*, 3:245, 2010.
- [167] U. H. E. Hansmann and Y. Okamoto. New Monte Carlo algorithms for protein folding. *Current Opinion in Structural Biology*, 9:177, 1999.
- [168] A. K. Hartmann and H. Reiger. *Optimization Algorithms in Physics*. Wiley-Vch, 2002.
- [169] A. Shapiro. Monte Carlo Sampling Methods. *Handbooks in Operations Research and Management Science*, 10:353, 2003.
- [170] K. Binder and D. W. Heermann. *Monte Carlo Simulations in Statistical Physics*. Springer-Verlag, 1988.
- [171] M. Troyer and U.-J. Wiese. Computational Complexity and Fundamental Limitations to Fermionic Quantum Monte Carlo Simulations. *Phys. Rev. Lett.*, 94:170201, 2005.
- [172] A. W. Sandvik and J. Kurkijärvi. Quantum Monte Carlo simulation method for spin systems. *Phys. Rev. B*, 43:5950, 1991.
- [173] A. W. Sandvik. Stochastic series expansion method with operator-loop update. *Phys. Rev. B*, 59:R14157, 1999.
- [174] A. W. Sandvik. Stochastic series expansion for quantum Ising models with arbitrary interactions. *Phys. Rev. E*, 68:056701, 2003.
- [175] A. Cuccoli, T. Roscilde, V. Tognetti, R. Vaia, and P. Verrucchi. Quantum Monte Carlo study of $S=1/2$ weakly anisotropic antiferromagnets on the square lattice. *Phys. Rev. B*, 67:104414, 2003.
- [176] F. Alet, S. Wessel, and M. Troyer. Generalized directed loop method for quantum Monte Carlo simulations. *Phys. Rev. E*, 71:036706, 2005.
- [177] D. C. Handscomb. The Monte Carlo method in quantum statistical mechanics. *Proc. Cambridge Philos. Soc.*, 58:594, 1962.
- [178] J. A. Hertz. Quantum Critical Phenomena. *Phys. Rev. B*, 14:1165, 1975.

- [179] M. Suzuki. Relationship between d-Dimensional Quantal Spin Systems and (d+1)-Dimensional Ising Systems. *Prog. Theor. Phys.*, 56:1454, 1976.
- [180] N. V. Prokof'ev, B. V. Svistunov, and I. S. Tupitsyn. Worm algorithm in quantum Monte Carlo simulations. *Physics Letters A*, 238:253, 1997.
- [181] M. Boninsegni, N. V. Prokof'ev, and B. V. Svistunov. Worm Algorithm for Continuous-Space Path Integral Monte Carlo Simulations. *Phys. Rev. Lett.*, 96:070601, 2006.
- [182] S. M. A. Rombouts, K. Van Houcke, and L. Pollet. Loop Updates for Quantum Monte Carlo Simulations in the Canonical Ensemble. *Phys. Rev. Lett.*, 96:180603, 2006.
- [183] K. Van Houcke, S. M. A. Rombouts, and L. Pollet. Quantum Monte Carlo simulation in the canonical ensemble at finite temperature. *Phys. Rev. E*, 73:056703, 2006.
- [184] A. W. Sandvik. Computational Studies of Quantum Spin Systems. *AIP Conf. Proc.*, 1297:135, 2010.
- [185] <http://lpsolve.sourceforge.net/>.
- [186] L. Pollet, S. M. A. Rombouts, K. Van Houcke, and K. Heyde. Optimal Monte Carlo updating. *Phys. Rev. E*, 70:056705, 2004.
- [187] L. Pollet, K. Van Houcke, and S. M. A. Rombouts. Engineering local optimality in quantum Monte Carlo algorithms. *J. Comp. Phys.*, 225:2249, 2007.
- [188] A. Dorneich and M. Troyer. Accessing the dynamics of large many-particle systems using Stochastic Series Expansion. *Phys. Rev. E*, 64:066701, 2001.
- [189] N. V. Prokof'ev and B. V. Boninsegni. Two definitions of superfluid density. *Phys. Rev. B*, 61:11282, 2000.
- [190] E. L. Pollock and D. M. Ceperley. Path-integral computation of superfluid densities. *Phys. Rev. B.*, 36(16):8343–8352, 1987.

- [191] W. H. Press, S. A. Teukolsky, W. T. Vetterling, and B. P. Flannery. *Numerical Recipes in C*. Cambridge University Press, Cambridge, 1992.
- [192] J. Shao and D. Tu. *The jackknife and bootstrap*. Springer, 1995.
- [193] T. Bataille, N. Mahé, E. Le Fur, and J.-Y. Pivan and D. Louër. Using the parallel tempering algorithm to overcome complex problems in structure determination of inorganic materials with laboratory X-rays. *Z. Kristallogr. Suppl.*, 23:9, 2006.
- [194] S. Trebst, M. Troyer, and U. H. E. Hansmann. Optimized parallel tempering simulations of proteins. *J. Chem. Phys.*, 124:174903, 2006.
- [195] K. Hukushima and K. Nemoto. Exchange Monte Carlo method and application to spin glass simulations. *J. Phys. Soc. Jpn.*, 65:1604, 1995.
- [196] F. Wang and D. P. Landau. Efficient, Multiple-Range Random Walk Algorithm to Calculate the Density of States. *Phys. Rev. Lett.*, 86:2050, 2001.
- [197] F. Wang and D. P. Landau. Determining the density of states for classical statistical models: A random walk algorithm to produce a flat histogram. *Phys. Rev. E*, 64:056101, 2001.
- [198] M. Troyer, F. Alet, and S. Wessel. Flat Histogram Methods for Quantum Systems: Algorithms to Overcome Tunneling Problems and Calculate the Free Energy. *Phys. Rev. Lett.*, 90:120201, 2003.
- [199] R. H. Swendsen and J.-S. Wang. Replica Monte Carlo Simulation of Spin-Glasses. *Phys. Rev. Lett.*, 57:2607, 1986.
- [200] C. E. Fiore and M. G. E. Luz. Comparing parallel- and simulated-tempering-enhanced sampling algorithms at phase-transition regimes. *Phys. Rev. E*, 82:031104, 2010.
- [201] E. Marinari and G. Parisi. Simulated tempering: a new Monte Carlo scheme. *Europhys. Lett.*, 19:451, 1992.

- [202] A. P. Lyubartsev, A. A. Martsinovski, S. V. Shevkunov, and P. N. Vorotsov-Velyaminov. New approach to Monte Carlo calculation of the free energy: Method of expanded ensembles. *J. Chem. Phys.*, 96:1776, 1992.
- [203] P. Sengupta, A.W. Sandvik, D.K. Campbell. Bond-order-wave phase and quantum phase transitions in the one-dimensional extended Hubbard model. *Phys. Rev. B*, 65:155113, 2002.
- [204] D. J. Earl and M. W. Deem. Parallel tempering: Theory, applications, and new perspectives. *Phys. Chem. Chem. Phys.*, 7:3910, 2005.
- [205] J. Machta. Strengths and weaknesses of parallel tempering. *Phys. Rev. E*, 80:056706, 2009.
- [206] C. Predescu, M. Predescu, and C.V. Ciobanu. The incomplete beta function law for parallel tempering sampling of classical canonical systems. *J. Chem. Phys.*, 120:4119, 2004.
- [207] H. G. Katzgraber, S. Trebst, D. A. Huse, and M. Troyer. Feedback-optimized parallel tempering Monte Carlo. *J. Stat. Mech.*, 2006:03018, 2006.
- [208] E. Bittner, A. Nussbaumer, and W. Janke. Make Life Simple: Unleash the Full Power of the Parallel Tempering Algorithm. *Phys. Rev. Lett.*, 101:130603, 2008.
- [209] M. Hasenbusch and S. Schaefer. Speeding up parallel tempering simulations. *Phys. Rev. E*, 82:046707, 2010.
- [210] F. Verstraete and J. I. Cirac. Renormalization algorithms for Quantum-Many Body Systems in two and higher dimensions. *cond-mat/0407066*, 2004.
- [211] F. Verstraete, M. M. Wolf, D. Perez-Garcia, and J. I. Cirac. Criticality, the Area Law, and the Computational Power of Projected Entangled Pair States. *Phys. Rev. Lett.*, 96:220601, 2006.

- [212] G. Vidal. Entanglement Renormalization. *Phys. Rev. Lett.*, 99:220405, 2007.
- [213] Z.-C. Gu, M. Levin, and X.-G. Wen. Tensor-entanglement renormalization group approach to 2D quantum systems. *Phys. Rev. B*, 78:205116, 2008.
- [214] S. Yan, D. A. Huse, and S. R. White. Ground State of the $S = 1/2$ Kagome Heisenberg Antiferromagnet. *Science*, 28:1126, 2011.
- [215] S. R. White and R. M. Noack. Real-space quantum renormalization groups. *Phys. Rev. Lett.*, 68(24):3487, 1992.
- [216] E. M. Stoudenmire and S. R. White. Studying Two Dimensional Systems With the Density Matrix Renormalization Group. *arXiv:1105.1374*, 2011.
- [217] M. Levin and C. P. Nave. Tensor Renormalization Group Approach to Two-Dimensional Classical Lattice Models. *Phys. Rev. Lett.*, 99:120601, 2007.
- [218] L. P. Kanadoff. Scaling laws for Ising models near T_c . *Physics*, 2:263, 1966.
- [219] M. Hinczewski and A. N. Berker. High-precision thermodynamic and critical properties from tensor renormalization group flows. *Phys. Rev. E*, 77:011104, 2008.
- [220] M.-C. Chang and M.-F. Yang. Magnetization Plateau of Classical Ising Model on Shastry-Sutherland Lattice. *Phys. Rev. B*, 79:104411, 2009.
- [221] H. C. Jiang, Z. Y. Weng, and T. Xiang. Accurate Determination of Tensor Network State of Quantum Lattice Models in Two Dimensions. *Phys. Rev. Lett.*, 101:090603, 2008.
- [222] H.-H. Zhao, Z. Y. Xie, Q. N. Chen, Z. C. Wei, J. W. Cai, and T. Xiang. Renormalization of tensor-network states. *Phys. Rev. B*, 81:174411, 2010.
- [223] W. Li, S.-S. Gong, Y. Zhao, and G. Subir. Quantum phase transition, $O(3)$ universality class, and phase diagram of the spin-1/2 Heisenberg antiferromagnet on a distorted honeycomb lattice: A tensor renormalization-group study. *Phys. Rev. B*, 81:184427, 2010.

- [224] Z. Y. Xie, H. C. Jiang, Q. N. Chen, Z. Y. Weng, and T. Xiang. Second Renormalization of Tensor-Network States. *Phys. Rev. Lett.*, 103:160601, 2009.
- [225] K. Okunishi, Y. Hieida, and Y. Akutsu. Universal asymptotic eigenvalue distribution of density matrices and corner transfer matrices in the thermodynamic limit. *Phys. Rev. E*, 59:R6227, 1999.
- [226] W. Lenz. *Physik. Z.*, 21:613, 1920.
- [227] E. Ising. Beitrag zur Theorie des Ferromagnetismus. *Z. Physik*, 31:253, 1925.
- [228] L. Onsager. Crystal Statistics. I. A Two-Dimensional Model with an Order-Disorder Transition. *Phys. Rev.*, 65:117, 1944.
- [229] S. G. Brush. History of the Lenz-Ising Model. *Rev. Mod. Phys.*, 39:883, 1967.
- [230] D. J. Thouless, M. Kohmoto, M. P. Nightingale, and M. den Nijs. Quantized Hall Conductance in a Two-Dimensional Periodic Potential. *Phys. Rev. Lett.*, 49:405, 1982.
- [231] X.-L. Qi, Y.-S. Wu, and S.-C. Zhang. Topological quantization of the spin hall effect in two-dimensional paramagnetic semiconductors. *Phys. Rev. B*, 74:085308, 2006.
- [232] X.-L. Qi, T. L. Hughes, and S.-C. Zhang. Topological Field Theory of time-reversal invariant insulators. *Phys. Rev. B*, 78:195424, 2006.
- [233] J. E. Moore. The birth of topological insulators. *Nature*, 464:194, 2010.
- [234] T. Senthil, A. Vishwanath, L. Balents, S. Sachdev, and M. P. A. Fisher. Deconfined Quantum Critical Points. *Science*, 303:1490, 2004.
- [235] T. Senthil, L. Balents, S. Sachdev, A. Vishwanath, and M. P. A. Fisher. Quantum criticality beyond the Landau-Ginzburg-Wilson paradigm. *Phys. Rev. B*, 70:144407, 2004.

- [236] J. Cardy. *Scaling and Renormalization in Statistical Physics*. Cambridge University Press, 1996.
- [237] F. Schwabl. *Statistische Mechanik*, volume 3. Springer, 2006.
- [238] P. Ginsparg. *Champs, Cordes et Phénomènes Critiques / Fields, Strings and Critical Phenomena: Applied Conformal Field Theory*. Elsevier, 1989.
- [239] P. Di Francesco, P. Mathieu, and D. Sénéchal. *Conformal Field Theory*. Springer, 1997.
- [240] K. G. Wilson. The renormalization group: Critical phenomena and the Kondo problem. *Rev. Mod. Phys.*, 47(4):773, 1975.
- [241] K. S. D. Beach, L. Wang, and A. W. Sandvik. Data collapse in the critical region using finite-size scaling with subleading corrections. *cond-mat:0505194*, 2005.
- [242] V. L. Berezinskii. Destruction of Long-range Order in One-dimensional and Two-dimensional Systems having a Continuous Symmetry Group I. Classical Systems. *Sov. Phys. JETP*, 32:493, 1971.
- [243] J. M. Kosterlitz and D. J. Thouless. Ordering, metastability and phase transitions in two-dimensional systems. *J. Phys. C*, 6:1181, 1973.
- [244] X.-G. Wen. *Quantum Field Theory of Many-body Systems*. Oxford Univ. Press, 2004.
- [245] H. Weber and P. Minnhagen. Monte Carlo determination of the critical temperature for the two-dimensional XY model. *Phys. Rev. B*, 37:5986, 1988.
- [246] K. Harada and N. Kawashima. Universal jump in the helicity modulus of the two-dimensional quantum XY model. *Phys. Rev. B*, 55:R11949, 1997.
- [247] S. E. Korshunov. Phase transitions in the antiferromagnetic XY model with a kagome lattice. *Phys. Rev. B*, 65:054416, 2002.

- [248] D. H. Lee and G. Grinstein. String in Two-Dimensional Classical XY Models. *Phys. Rev. Lett.*, 55:541, 1985.
- [249] D. B. Carpenter and J. T. Chalker. The phase diagram of a generalised XY model. *J. Phys.: Condens. Matter*, 1:4907, 1989.
- [250] S. Diehl, M. Baranov, A. J. Daley, and P. Zoller. Quantum Field Theory for the Three-Body Constrained Lattice Bose Gas – Part I: Formal Developments. *Phys. Rev. B*, 82:064509, December 2009.
- [251] S. Diehl, M. Baranov, A. J. Daley, and P. Zoller. Observability of Quantum Criticality and a Continuous Supersolid in Atomic Gases. *Phys. Rev. Lett.*, 104:165301, 2010.
- [252] J. G. Valatin and D. Butler. On the collective properties of a boson system. *Nuovo Cimento*, 10:37, 1958.
- [253] K. P. Schmidt, J. Dorier, A. Läuchli, and F. Mila. Single-particle versus pair condensation of hard-core bosons with correlated hopping. *Phys. Rev. B*, 74:174508, 2006.
- [254] X.-F. Zhou, Y. S. Zhang, and G.-C. Guo. Pair tunneling of bosonic atoms in an optical lattice. *Phys. Rev. B*, 80:013605, 2009.
- [255] L. Mazza, M. Rizzi, M. Lewenstein, and J. I. Cirac. Emerging Bosons with Three-Body Interactions from Spin-1 Atoms in Optical Lattices. *Phys. Rev. A*, 82:043629, 2010.
- [256] A. F. Andreev and I. A. Grishchuk. Spin nematics. *Sov. Phys. JETP*, 60:267, 1984.
- [257] L. Radzihovsky, J. I. Park, and P. B. Weichmann. Superfluid transitions in bosonic atom-molecule mixtures near Feshbach resonance. *Phys. Rev. Lett.*, 92:160402, 2004.
- [258] S. Coleman and E. Weinberg. Radiative Corrections as the Origin of Spontaneous Symmetry Breaking. *Phys. Rev. D*, 7:1888, 1973.

- [259] S. Diehl, M. Baranov, A. J. Daley, and P. Zoller. Quantum Field Theory for the Three-Body Constrained Lattice Bose Gas – Part II: Application to the Many-Body Problem. *Phys. Rev. B*, 82:064510, December 2009.
- [260] L. Balents and D. R. Nelson. Quantum smectic and supersolid order in helium films and vortex arrays. *Phys. Rev. B*, 52:12951, 1995.
- [261] E. Frey and L. Balents. Critical behavior of the supersolid transition in Bose-Hubbard models. *Phys. Rev. B*, 55:1050–1067, 1997.
- [262] A. Kuklov, N. Prokof'ev, and B. Svistunov. Commensurate Two-Component Bosons in an Optical Lattice: Ground State Phase Diagram. *Phys. Rev. Lett.*, 92:050402, 2004.
- [263] M. J. Bhaseen, A. O. Silver, M. Hohenadler, and B. D. Simons. Feshbach Resonance in Optical Lattices and the Quantum Ising Model. *Phys. Rev. Lett.*, 103:265302, 2009.
- [264] S. Ejima, M. J. Bhaseen, M. Hohenadler, F. H. L. Essler, H. Fehske, and B. D. Simons. Ising Deconfinement Transition between Feshbach-Resonant Superfluids. *Phys. Rev. Lett.*, 106:015303, 2011.
- [265] H. J. Schulz. Phase diagrams and correlation exponents for quantum spin chains of arbitrary spin quantum number. *Phys. Rev. B*, 34:6372, 1986.
- [266] W. Chen, K. Hida, and B. C. Sanctuary. Ground-state phase diagram of $S=1$ XXZ chains with uniaxial single-ion-type anisotropy. *Phys. Rev. B*, 67:104401, 2003.
- [267] S. R. Manmana, A. M. Läuchli, F. H. L. Essler, and F. Mila. Phase diagram and continuous pair-unbinding transition of the bilinear-biquadratic $S=1$ Heisenberg chain in a magnetic field. *arXiv:1012.4518*, 2010.
- [268] H. H. Zhao, Q. N. Chen, Z. C. Wei, M. P. Qin, G. M. Zhang, and T. Xiang. Quantum spin liquid phase in the spin-1 bilinear-biquadratic Heisenberg model on a honeycomb lattice. *arXiv:1105.2716*, 2011.

- [269] M. E. Zhitomirsky and T. Nikuni. Magnetization curve of a square-lattice Heisenberg antiferromagnet. *Phys. Rev. B*, 57:5013, 1998.
- [270] K. Bernardet, G. G. Bartouni, J.L. Meunier, G. Schmid, M. Troyer, and A. Dorneich. Analytical and numerical study of hardcore bosons in two dimensions. *Phys. Rev. B*, 65:104519, 2002.
- [271] M. Hasenbusch, K. Pinn, and S. Vinti. Critical exponents of the three-dimensional Ising universality class from finite-size scaling with standard and improved actions. *Phys. Rev. B*, 59:11471, 1999.
- [272] M. Eckholt and T. Roscilde. Comment on "Feshbach-Einstein Condensates" by V. G. Rousseau and P. J. H. Denteneer. *Phys. Rev. Lett.*, 105:199603, 2010.
- [273] V. G. Rousseau and P. J. H. Denteneer. Feshbach-Einstein Condensates. *Phys. Rev. Lett.*, 102:015301, 2009.
- [274] L. Pollet, M. Troyer, K. Van Houcke, and S. M. A. Rombouts. Phase Diagram of Bose-Fermi Mixtures in One-Dimensional Optical Lattices. *Phys. Rev. Lett.*, 96:190402, 2006.
- [275] T. Roscilde and J. I. Cirac. Quantum Emulsion: A Glassy Phase of Bosonic Mixtures in Optical Lattices. *Phys. Rev. Lett.*, 98:190402, 2007.
- [276] S. Guertler, M. Troyer, and F.-C. Zhang. Quantum Monte Carlo study of a two-species bosonic Hubbard model. *Phys. Rev. B*, 77:184505, 2008.
- [277] S. G. Söyler, B. Capogrosso-Sansone, N. V. Prokof'ev, and B. V. Svistunov. Sign-alternating interaction mediated by strongly correlated lattice bosons. *New J. of Phys.*, 11:073036, 2009.
- [278] P. Chen and M.-F. Yang. Quantum phase transitions in a two-species hardcore boson Hubbard model in two dimensions. *Phys. Rev. B*, 82:180510(R), 2010.
- [279] Y.-C. Chen, K.-K. Ng, and M.-F. Yang. Quantum phase transitions in attractive extended Bose-Hubbard Model with three-body constraint. *arXiv:1103.3350*, 2011.

- [280] D. Yamamoto, I. Danshita, and C. A. R. Sa de Melo. Dipolar Bosons in Triangular Optical Lattices: Quantum Phase Transitions and Anomalous Hysteresis. *arXiv:1102.1317*, 2011.
- [281] X.-F. Zhang, Y.-C. Wen, and Y. Yu. Three-body interactions on a triangular lattice. *Phys. Rev. B*, 83:184513, 2011.
- [282] E. Jones, T. Oliphant, P. Peterson, et al. SciPy: Open source scientific tools for Python, 2001.
- [283] <http://www.netlib.org/minpack/>.
- [284] M. Campostrini, M. Hasenbusch, A. Pelissetto, and E. Vicari. Theoretical estimates of the critical exponents of the superfluid transition in ^4He by lattice methods. *Phys. Rev. B*, 74:144506, 2006.
- [285] J. Zinn-Justin. *Quantum Field Theory and Critical Phenomena, 3rd Edition*. Oxford University Press, Great Clarendon Street, Oxford, UK, 1997.
- [286] K. P. Schmidt, J. Dorier, A. M. Läuchli, and F. Mila. Supersolid Phase Induced by Correlated Hopping in Spin-1/2 Frustrated Quantum Magnets. *Phys. Rev. Lett.*, 100:090401, 2008.
- [287] R. J. Baxter and F. Y. Wu. Exact Solution of an Ising Model with Three-Spin Interactions on a Triangular Lattice. *Phys. Rev. Lett.*, 31:1294, 1973.
- [288] L. L. Liu and H. E. Stanley. Exact solution in an external magnetic field of Ising models with three-spin interactions. *Phys. Rev. B*, 10:2958, 1974.
- [289] F. Y. Wu and H. E. Stanley. Universality of Potts models with two- and three-site interactions. *Phys. Rev. B*, 26:6326, 1982.
- [290] K. K. Chin and D. P. Landau. Monte Carlo study of a triangular Ising lattice-gas model with two-body and three-body interactions. *Phys. Rev. B*, 36:275, 1987.
- [291] C. Menotti, C. Trefzger, and M. Lewenstein. Metastable States of a Gas of Dipolar Bosons in a 2D Optical Lattice. *Phys. Rev. Lett.*, 98:235301, 2007.

- [292] B. Spivak and S. A. Kivelson. Phases intermediate between a two-dimensional electron liquid and Wigner crystal. *Phys. Rev. B*, 70:155114, 2004.
- [293] L. Pollet, M. Boninsegni, A. B. Kuklov, N. V. Prokof'ev, B. V. Svistunov, and M. Troyer. Superfluidity of Grain Boundaries in Solid ^4He . *Phys. Rev. Lett.*, 98:135301, 2007.
- [294] U. Schollwöck, J. Richter, D. J. J. Farnell, R. F. Bishop, and Eds. *Quantum Magnetism, Lecture Notes in Physics 645*. Springer-Verlag, Berlin, 2004.
- [295] S. Wessel, N. Stoop, E. Gull, S. Trebst, and M. Troyer. Optimized broad-histogram ensembles for the simulation of quantum systems. *J. Stat. Mech.*, page 12005, 2007.
- [296] D. E. Knuth. *The Art of Computer Programming*, volume 2. Addison-Wesley Publishing Company, 1998.
- [297] R. Kenyon. *Directions in Mathematical Quasicrystals: The Planar Dimer Model with Boundary*. American Mathematical Society, 2000.
- [298] R. Moessner, S.L. Sondhi and P. Chandra. Phase diagram of the hexagonal lattice quantum dimer model. *Phys. Rev. B*, 64:144416, 2001.
- [299] E. Anderson, Z. Bai, C. Bischof, S. Blackford, J. Demmeland J. Dongarra, J. Du Croz, A. Greenbaum, S. Hammarlingand A. McKenney, and D. Sorensen. *LAPACK Users' Guide*. Society for Industrial and Applied Mathematics, third edition, 1999.
- [300] M. P. A. Fisher, P. B. Weichman, G. Grinstein, and D. S. Fisher. Boson localization and the superfluid-insulator transition. *Phys. Rev. B*, 40:546, 1989.
- [301] K. Bernardet, G. G. Bartouni, and M. Troyer. Destruction of diagonal and off-diagonal long-range order by disorder in two-dimensional hard-core boson systems. *Phys. Rev. B*, 66:054520, 2002.

- [302] N. V. Prokof'ev and B. V. Svistunov. Superfluid-Insulator Transition in Commensurate Disordered Bosonic Systems: Large-Scale Worm Algorithm Simulations. *Phys. Rev. Lett.*, 92:015703, 2004.
- [303] S. Pilati, S. Giorgini, and N. Prokof'ev. Superfluid Transition in a Bose Gas with Correlated Disorder. *Phys. Rev. Lett.*, 102:150402, 2009.
- [304] L. Pollet, N. V. Prokof'ev, B. V. Svistunov, and M. Troyer. Absence of a direct superfluid to mott insulator transition in disordered bose systems. *Phys. Rev. Lett.*, 103:140402, 2009.
- [305] V. Gurarie, L. Pollet, N. V. Prokof'ev, B. V. Svistunov, and M. Troyer. Phase diagram of the disordered Bose-Hubbard model. *Phys. Rev. B*, 80:214519, 2009.
- [306] Y. Imry and S.-K. Ma. Random-field instability of the ordered state of continuous symmetry. *Phys. Rev. Lett.*, 35:1399, 1975.
- [307] A. V. Gorshkov, M. Hermele, V. Gurarie, C. Xu, P. S. Julienne, J. Ye, P. Zoller, E. Demler, M. D. Lukin, and A. M. Rey. Two-orbital $SU(N)$ magnetism with ultracold alkaline-earth atoms. *Nature Physics*, 6:289, 2010.
- [308] K. R. A. Hazzard, V. Gurarie, M. Hermele, and A. M. Rey. High temperature thermodynamics of fermionic alkaline earth atoms in optical lattices. *arXiv:1011.0032*, 2010.
- [309] M. Hermele, V. Gurarie, and A. M. Rey. Mott Insulators of Ultracold Fermionic Alkaline Earth Atoms: Underconstrained Magnetism and Chiral Spin Liquid. *Phys. Rev. Lett.*, 103:135301, 2009.
- [310] C. Wulf. Exotic many-body physics with large-spin Fermi gases. *Physics*, 3:92, 2010.
- [311] K. Buchta, Ö. Legeza, E. Szirmai, and J. Sólyom. Mott transition and dimerization in the one-dimensional $SU(n)$ Hubbard model. *Phys. Rev. B*, 75:155108, 2007.

- [312] G. Verstraete, J. J. Garcia-Ripoll, and J. I. Cirac. Matrix Product Density Operators: Simulation of Finite-Temperature and Dissipative Systems. *Phys. Rev. Lett.*, 93:207204, 2004.
- [313] D. A. Butts and D. S. Rokhsar. Trapped Fermi gases. *Phys. Rev. A*, 55:4346, 1997.
- [314] M. Troyer, F. Alet, and S. Wessel. Histogram Methods for Quantum Systems: From Reweighting to Wang-Landau Sampling. *Braz. J. of Physics*, 34:377, 2004.
- [315] B. Capogrosso-Sansone, Ş. G. Söyler, N. V. Prokof'ev, and B. V. Svistunov. Critical entropies for magnetic ordering in bosonic mixtures on a lattice. *Phys. Rev. A*, 81:053622, 2010.
- [316] T. Roscilde. Phase Transitions and Crossovers in Two-Dimensional Anisotropic Quantum Antiferromagnets. *Doctoral Thesis*, 2002.
- [317] Algorithms and Libraries for Physics Simulations. <http://alps.comp-phys.org/>.
- [318] Message Passing Interface. <http://www.mpi-forum.org/>.

Danksagung

Ich danke der Studienstiftung des Deutschen Volkes, die mich während meines Studium an der ETH Zürich sowie in Doktorarbeit großzügig gefördert hat.

Ein großer Dank gebührt meinem Lehrer Stefan Wessel, der mich durch meine Promotion geführt hat und von dem ich nicht nur fachlich, sondern auch menschlich profitiert habe.

Zudem danke ich Prof. Pfau and Prof. Wunner, die sich bereit erklärt haben, den Vorsitz in meiner Doktorprüfung zu übernehmen bzw. als Zweitberichter meine Arbeit zu bewerten.

Meine Mitstreiter am Insitut für Theoretische Physik III der Universität Stuttgart seien hier noch erwähnt. Insbesondere Adam, Alexander, Jürgen, Steffen, Thorsten und Zi Yang, mit denen ich so manche Tasse Kaffee getrunken und über Gott und die Welt gesprochen habe.

In meiner Zeit als Doktorand hatte ich die Möglichkeit mit zwei Gruppen zu kooperieren. Ich danke Stephan Haas und der Gruppe an der USC, Los Angeles, für ihre Gastfreundschaft und die interessante Zeit, die ich dort verbringen durfte. Auch erwähnen möchte ich Salvatore Manmana, der sich bei meinem Besuch in Boulder viel Zeit für mich genommen hat, und Kaden Hazzard sowie die Theoriegruppe von Ana Maria Rey am JILA.

Abschließend muß ich noch Svenja erwähnen, ohne die mein Leben nicht mal halb so schön wäre und die auch in nicht so einfachen Zeiten fest an meiner Seite stand.